Copper Oxide Single-nanowire-based Devices and Applications

A

Thesis submitted

for the award of the degree of

DOCTOR OF PHILOSOPHY

By

S. Raveesh

DEPARTMENT OF ELECTRONICS AND ELECTRICAL ENGINEERING

INDIAN INSTITUTE OF TECHNOLOGY GUWAHATI

GUWAHATI - 781 039, ASSAM, INDIA

June 2022

TH-2675_186102019

TH-2675_186102019

DECLARATION

This is to certify that the thesis entitled "**Copper Oxide Single-nanowire-based Devices and Applications**", submitted by me to the *Department of Electronics and Electrical Engineering, Indian Institute of Technology Guwahati* for the award of the degree of **Doctor of Philosophy**. This is an original research work carried out by me under the supervision of **Prof. Roy P. Paily**. The contents of this thesis, in full or in parts, have not been submitted to any other Institute or University for the award of any degree or diploma.

Signed: 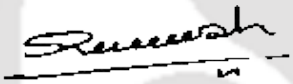

S. Raveesh
Department of Electronics & Electrical Engineering,
Indian Institute of Technology Guwahati,
Guwahati-781039, Assam, India.

Date: 08/06/2022

TH-2675_186102019

TH-2675_186102019

CERTIFICATE

This is to certify that the thesis entitled "**Copper Oxide Single-nanowire-based Devices and Applications**", submitted by **S. Raveesh** (186102019), a research scholar in the *Department of Electronics and Electrical Engineering, Indian Institute of Technology Guwahati*, for the award of the degree of **Doctor of Philosophy**, is a record of an original research work carried out by him under my supervision and guidance. The thesis has fulfilled all requirements as per the regulations of the institute, and in my opinion has reached the standard needed for submission. The results embodied in this thesis have not been submitted to any other University or Institute for the award of any degree or diploma.

Signed:

Prof. Roy P. Paily
Department of Electronics & Electrical Engineering,
Indian Institute of Technology Guwahati,
Guwahati-781039, Assam, India.

Date:

TH-2675_186102019

TH-2675_186102019

Dedicated to

Parents and In-laws

TH-2675_186102019

TH-2675_186102019

Acknowledgements

Every research requires an amicable atmosphere in personalities and places, with the focused efforts. In this regard, for the successful completion of my thesis, I would like to thank the following persons, Centers, and Institutes. First and foremost, I am extremely privileged to take this opportunity to express my sincere and honest gratitude to my thesis supervisor, Prof. Roy Paily Palathinkal, for the motivation, guidance, and support in the entire course of my research work.

I am very thankful to my doctoral committee members Dr. Harshal B. Nemade (Chairman), Dr. Arun Tej Mallajosyula, and Dr. D. Pamu, for sparing their valuable time to assess the progress of my research work and provide constructive suggestions to improve my work. I would also like to thank the Head of the Electronics and Electrical Engineering Department and the other faculty members for their kind help in carrying out research work. I am also grateful to the technical staff of the department. My special thanks to Mrs. S. Josephine, Technical Officer, for helping me to utilize the lab resources and purchase of consumables for the experiments.

I am grateful to the Head of Centre for Nanotechnology (CNT) and Centre For Excellence in Nanoelectronics and Theranostic Devices (CENTD), IIT Guwahati, and faculty members associated with the centre for providing me the opportunity to utilize the high-end instruments for fabrication and characterization of the devices. I would like to acknowledge the technical and supporting staff members of Centre of Nanotechnology for their help in conducting the experiments. I extend my sincere thanks to Mrs. Emlin E. Abraham and Reena Dey from CNT, who helped me to purchase chemicals, gases, and glassware for the experiments; also, fruitful technical discussions in using the cutting edge instruments. Special thanks to Mr. Manjay for helping in replacing various gas cylinders for our gas sensing experiments, fixing the pumps, and installing the sensing chamber. My honest thanks to Central Instruments Facility (CIF), IIT Guwahati, for permitting me to carry out material characterization. I extend my warmest thanks to the technical staff and all the operators of the instruments in CNT, CIF, and other departments used in my research work.

I wish to convey my heartiest gratitude to Prof. P. K. Iyer, Department of Chemistry, IITG, for providing access to the muffle furnace for the thermal oxidation and Prof. P. K. Giri, Department of Physics, IITG, to access Xenon lamp with a monochromator, to record the spectral response of the fabricated devices.

TH-2675_186102019

I am very grateful to Siddaganga Institute of Technology (SIT), Tumakuru, Karnataka, India, for deputing me to study at Indian Institute of Technology Guwahati, Assam, with financial assistance. My valuable thanks to Dr. M. N. Channabasappa, Director, SIT, for his motivation to complete the research work. I sincerely thank Dr. Shivakumariah, Chief Executive Officer, and Dr. S V Dinesh, Principal, SIT, Tumakuru, for the help and support. I am thankful to Dr. K. C. Narasimhamurthy, Head, Electronics and Telecommunication Engineering, for encouraging me to pursue my research in microelectronics.

My warm thanks to all my fellow research scholars and friends for their cooperation. At IITG, I have several friends who helped me morally and in the technical discussions. I would like to say a big thanks to Dr. Vimal Kumar Singh Yadav and Mr. Thomas T. Daniel, without whose help I could not have completed my research experiments.

I would like to express my thanks to my labmates Mr. Pralay, Mr. Rajan, Mr. Siddhanta, Ms. Monica, Mr. Satyajit, Mr. Birjit, Mr. Rahul, Mr. Mridul, Mr. Hari, for the lively atmosphere in the lab. I would wish to thank Dr. Ayan pal, Mr. Arin Bhakat, Md. Tarik Hossain, and Mr. Ramesh Babu Y. Mr. Tamal Pal, for the discussions and suggestions. I am thankful to Mr. Karan Kumar, Mr. Rohit, Mr. Sunil, Mr. Debanjan Roy Chowdhury, Mr. Brij Nandan Tripathi for their moral support. I owe my sincere thanks to the Government of India for providing the opportunity and financial support to carry out this research work. I also extend my thanks to the people of India, who have helped my efforts indirectly in many ways.

Acknowledgement section is half-done if I miss my parents, in-laws, and elders of family for their continuous support and love during my studies; the unlimited sacrifices are the prime reasons for my accomplishments. I offer my heartfelt gratitude to my parents Sri. Siddaramaiah and Smt. Girija; in-laws Sri. Ramakrishnappa and Smt. Chayadevi. I also thank my brother family, Sri. and Smt. Kiran, for the support.

Finally, my heart deepest thanks to my better half, Smt. Shwetha Kiran R., patient enough for years to complete my research work; also proof-reading the manuscripts and supporting me in all possible ways and loving thanks to my son Chi. Shaurya.

S. Raveesh

TH-2675_186102019

Abstract

Transition-metal-oxide semiconductors, including composites in nano-form, are explored widely for photodetectors and volatile organic compound (VOC) sensors in two-terminal and field-effect-transistor (FET) configurations. Photodetectors are generally used in optical detectors, communication, and thermal imaging systems. On the other hand, VOC biosensors have facilitated the early detection, diagnosis, and treatment of diseases and disorders in recent days. Moreover, VOC sensors are also used in indoor real-time monitoring of hazardous VOC concentration in offices, research labs, industries, and commercial buildings which are crucial for human safety.

The prime focus of the thesis is to fabricate the copper oxide (CuO) single nanowire (SNW) two-terminal and FET devices using silver nanoparticles (AgNP) microcantilever contact printed (μCCP) electrode for the photodetection and VOCs detection. Also, the design and development of control environment chambers (CECs) to measure sensor response for gases (hydrogen, carbon dioxide, carbon monoxide, sulfur dioxide, hydrogen sulfide, and nitric oxide) and VOCs (ethanol, acetone, 2-propanol, methanol, ammonia, toluene, chlorobenzene, p-Xylene, and cyclohexane). The first contribution includes the fabrication of CuO SNW photodetector fabricated using spot overwrite and drag printing techniques. The photodetector exhibits exceptional performance and reliability. Also, experimental analysis of the irregular response of CuO SNW printed devices under various operating conditions at lower bias voltage is analyzed.

The second contribution includes the design of two controlled environment chamber (CEC) systems. The first one, i.e., CEC 2.0 system, is proposed and developed to overcome the shortcomings of existing in-house developed CEC 1.0 for sensing the gases and VOCs that use carrier and analyte in compressed gas cylinders. The second one is designed exclusively to sense the VOCs in atmospheric air by a static liquid gas distribution method, which is more straightforward, portable, and employed where the gas flow regulation doesn't require mass flow controllers (MFCs).

TH-2675_186102019

The third contribution is the fabrication of two and three-terminal CuO SNW devices to sense VOCs such as ethanol, acetone, and 2-propanol, etc., at room temperature, 150 °C, and under white light for the concentrations ranging from 25-100 ppm. Devices exhibits a maximum response of 1.1% and 4.86% under various operating conditions with a limit of detection (LOD) of 15.4 ppm. The device has limited performance, but is stable for four months. The sensor has a limited response, and its reasons are analyzed.

The fourth contribution of the thesis includes the fabrication of CuO SNW FETs with the bottom gate, coplanar gate, and top gate architectures using μCCP technique.The fabricated FETs exhibit p-type conduction with hole mobility 0.14 – 0.36 $cm^{-2}V^{-1}$ s^{-1} with I_{on}/I_{off} of 5.5 and the hole concentration in dark and photo-excitation found to be in the range of 10^{16}–10^{17} cm^{-3} and 10^{17}–10^{19} cm^{-3}, respectively. The fifth contribution includes the fabrication of fully solution-processed planar capacitors and FET. Aluminum nitrate nonahydrate, sodium molybdate dihydrate, and AgNP inks are used to print gate oxide, channel, and electrodes, respectively. The printed FET has I_{on}/I_{off} of 10^3 with gate leakage of 10^{-8} A.

TH-2675_186102019

Contents

TH-2675_186102019

TH-2675_186102019

TH-2675_186102019

TH-2675_186102019

List of Figures

TH-2675_186102019

TH-2675_186102019

TH-2675_186102019

TH-2675_186102019

List of Tables

TH-2675_186102019

TH-2675_186102019

List of Acronyms

AgNP	Silver nanoparticles
Al	Aluminium
AuNP	Gold nanoparticles
CAD	Computer aided design
CEC	Control environment chamber
CF	Conflat
Cu	Copper
CuO	Copper oxide
DC	Direct current
DI	Deionized
DEP	Dielectrophoresis
EBL	Electron-beam lithography
EDS	Energy-dispersive X-ray spectroscopy
EQE	External quantum efficiency
FESEM	Field emission scanning electron microscopy
FET	Field effect transistor
FIB	Focussed ion beam
Ga–In	Gallium–indium
GCMS	Gas chromatography–mass spectroscopy
HPLC	High-performance liquid chromatography
IC	Integrated Circuit
IoT	Internet of Things
IR	Infrared
ITO	Indium tin oxide

TH-2675_186102019

JCPDS	Joint committee on powder diffraction standards
KF	Klein flansche
kHz	Kilohetrz
LED	Light-emitting diode
LOD	Limit of detection
LPM	liters per minute
MIM	Metal-insulator-metal
MSM	Metal-semiconductor-metal
MFC	Mass flow controller
NW	Nanowire
NWFET	Nanowire field effect transistor
OD	Outer diameter
OSHA	Occupational safety and health administration
PEL	Permissible exposure limit
PET	Polyethylene terephthalate
PID	Proportional-integral-derivative
PVDF–TrFE	Polyvinylidene fluoride–trifluorethylene
RH	Relative humidity
SAED	Selected area electron-diffraction
SBFET	Schottky barrier field-effect transistor
SMAT	Surface mechanical attrition treatment
SNW	Single nanowire
SPT	Surface patterning tool
SAW	Surface acoustic wave
TMO	Transition-metal-oxide
UV	Ultraviolet
VOCs	Volatile organic compounds
XRD	X-ray diffraction
1D	One-dimensional
μCCP	Microcantilever contact print

TH-2675_186102019

1

Introduction

भारतीय प्रौद्योगिकी संस्थान गुवाहाटी • Indian Institute of Technology Guwahati •

Contents

TH-2675_186102019

1.1 Introduction

Photodetectors are sensors that convert light into an electric signal; widely used in fiber optic systems, sensing, environment monitoring, and security-related applications. The chemical sensor detects the analytes (i.e., gas molecules, volatile organic compounds (VOCs), heavy metal ions, etc.). Volatile organic compounds are organic chemicals with a high vapor pressure at room temperature. In general, VOCs are gases emitted into the air from chemicals, products, and processes. The volatility of a VOC correlates with high vapor pressure, which is coupled with a low boiling point, a measure of the number of gas molecules in the surrounding air. The gas/VOCs sensor response is generally directly proportional to analyte concentration with the saturation levels. Gas sensors are specifically useful for both indoor and outdoor air monitoring of toxic/hazardous gases or VOCs for human health, well-being, and safety.

The presence of VOCs above the permissible exposure limit (PEL) cause severe diseases, and in some cases, may even lead to explosion [1–3]. However, on the other hand, VOC sensors may also be employed in healthcare for the non-invasive diagnosis of several diseases [4–6]. The developed gas sensor is usually tested with static and dynamic gas sensing measurement systems to validate the performance in the initial stages [7–10].

On the other hand, internet of hings (IoT) enabled devices and systems are in great demand in day-to-day life. IoT platform interfaces with the real world through sensors and actuators; IoT connected with numerous sensors for collecting data; which is further used for analytics. As IoT grows, the demand for sensors to measure the various physical quantities in the real world also grows [11–13], which leads to new directions in the development of sensors, detectors, and actuators. To develop the transducers researchers explore materials, device architecture, and systems to meet the requirement. A Kumar *et al.* demonstrated the ultra-high response deep-ultraviolet (UV) photodetector using Ga–In bimetallic oxide nanowires [14]. C Zhou *et al.* proposed self-driven WSe_2 photodetectors enabled with asymmetrical van der Waals contact interfaces [15]. TL Shen *et al.* showed the high-performance self-powered flexible photodetector driven from photogate, piezo-phototronic, and ferroelectric effects using PVDF-TrFE polymer and metal oxide nanoparticles [16]. J Ahn *et al.* developed a low-cost IoT sensing platform for VOCs classification using fluorometric sensors [17]. Y Gao *et al.* presented a review article on organic/inorganic hybrid sensors, which covers the fabrication of sensors in several configurations such as intercalating type, core-shell type, coating type, and mixed type [18].

TH-2675_186102019

Various organic and inorganic materials are explored as sensing materials to develop the sensors. Among them, metal oxide nanostructures are of vast research interest due to their distinctive fundamental properties compared to bulk. Despite various forms of nanostructures, one-dimensional (1D) is remarkable because of the charge carrier confinement within small dimension, large surface-to-volume ratio, and crystallinity. Nanostructures such as wires, fibers, rods, and belts are broadly used in photodetectors [19–24]; in VOCs and gas sensing using two terminal and field effect transistor (FET) architectures [25–27].

A wide range of metal oxides such as ZnO, SnO_2, WO_3, TiO_2 etc. has been used for photodetectors and sensing [21, 28–31]; similarly, copper oxide (CuO) is also one such p-type metal oxide that exists in two forms; copper (II) oxide and copper (I) oxide [32]. P-type oxide semiconductors such as NiO and CuO have been widely used as suitable catalysts to enable selective oxidation of various VOCs. Also, the p-n junction by oxide semiconductor materials can alter the gas-sensing characteristics by varying the charge transport near heterointerfaces [26,33–37]. Further, CuO possesses excellent photoresponse properties [38–41]. CuO exhibits direct bandgap of 2-4.15 eV and an indirect bandgap of 1-1.4 eV [21, 39, 40]; which helps to tune the conductivity of the device. The aforementioned bandgap engineering with CuO allows detection of UV, white light, and near-infrared [38–42].

This chapter is organized as follows. Section 1.2 deals with the brief overview of CuO nanostructure synthesis. Section 1.3 has a review of device fabrication and section 1.4 includes motivation and problem definition for various topics investigated in the thesis.

1.2 CuO Nanostructure Synthesis

CuO nanostructures synthesis broadly has two divisions: (i) physical and (ii) chemical synthesis routes. W Wang *et al.* synthesized the CuO nanorods using a simple wet-chemical route; CuO nanorods have dimension of 5 –15 nm diameter and lengths of up to 400 nm [43]. M Cao *et al.* demonstrated the CuO nanowires (NWs) and nanorods synthesized via controllable solution-phase hydrothermal method using a nonionic surfactant polyethylene glycol (PEG) as the template [44]. C Yang *et al.* synthesized CuO nanorods with width 15–20 nm and the length of 60–80 nm using the microwave-assisted hydrothermal method for sensing the ethanol at temperature 210 °C [45]. CuO nanofibers which are prepared by electrospinning, have diameter of ≈60 nm, length over 100 μm, and demonstrated a p-type FET [46].

TH-2675_186102019

Table 1.1: Table comparing advantages and disadvantages of different synthesis procedures for CuO NWs

Synthesis procedure	**Advantages**	**Disadvantages**
PVD	– Temperature requirement – Specialized precursors are not required – Availability of materials – Reproducibility	– Line-of-sight coating process – Widely used in thin films and 2D structures – Complex instrumentation
CVD	– Conformal deposition – Good control over stoichiometry – Morphology and roughness – Reproducibility	– High purity precursors – Widely used in thin films and 2D structures – Temperature requirement – Complex instrumentation – Difficult to mask surface
Sol-gel\ Hydrothermal	– Relatively mild operating temperatures – Simple instrumentation – Growth of 1D and 2D structures – Low cost and high yield	– Long processing time – High purity precursors – Morphology control is moderate – Less aspect ratio
Thermal oxidation	– **Simple instrumentation** – **Growth of 1D and 2D structures** – **Low cost and high yield** – **High crystalline and aspect ratio** – **Negligible impurities**	– **Temperature requirement** – **Long processing time**

CuO NW arrays are prepared by directly annealing the sputter-deposited copper nitride (Cu_3N) film at 300 °C for 90 min in the atmosphere [47]. CuO nanorod arrays are prepared on copper substrates by liquid-solid reactions. The morphology and composition of the structure are studied by varying the temperature, time, solvents, and pH value [48]. L Yuan *et al.* synthesis the CuO NWs by thermal oxidation of copper substrate [49]; also proposed a kinetic model based on the stress-driven grain-boundary diffusion for CuO nanowire growth. Anodic alumina template-based free-standing CuO nanorod arrays are formed by oxidation and are highly sensitive for the 808 nm IR laser light [38]. Surface mechanical attrition treatment (SMAT)-assisted CuO NWs are synthesized using oxidation, and photodetectors are fabricated on the flexible PET substrate. Moreover, FET is fabricated with back gate configuration on Si/SiO_2 substrate [50]. However, CuO NWs by thermal oxidation are highly crystalline with high aspect ratio and possess negligible impurities. Table 1.1 lists the advantages and disadvantages of different synthesis procedures for CuO NWs.

1.3 Device Fabrication

The device high performance and fabrication complexity go hand-in-hand. Electrode fabrication to NW plays a vital role in developing a device, and the process remains a challenge. Various methods, such as contact printing and sacrificial layers, employ bundled and interconnected NWs; post-processing

TH-2675_186102019

Table 1.2: Table comparing advantages and disadvantages of electrode deposition procedures for the fabrication of SNW devices

Electrode deposition procedure	**Advantages**	**Disadvantages**
Lift-up technique	– Simple instrumentation – Good for connecting multiple NWs – Low cost	– Metal - NW has a minimal interface – SNW device fabrication is difficult – Difficult to reproduce the identical structure
Dielectrophoresis	– Simple instrumentation – NWs are less affected during the process – Moderate operating cost	– Small gap limits voltage between electrodes – Multiple NWs may connect on electrodes – Metal - NW has a minimal interface
Ebeam lithography and FIB deposition	– Precise control over the process – Resolution up to few nm – Robust and reproducible – Good for SNW devices	– Complex instrumentation – High cost – Time-consuming – Metal - NW interface may be disturbed
Bridging	– On-chip process – Moderate operating cost – Good for connecting the multiple NWs	– NW-NW interface is minimal – Temperature requirement – Long processing time
Contact printing	– Simple instrumentation – Good for connecting the multiple NWs – Low-cost process – Roll-to-roll printing is possible	– SNW connection is difficult – Resolution up to tens of μm – Initial set-up time is high
μCCP	– **Simple instrumentation** – **Best feature-to-particle size ratio** – **Low viscosity inks (10-18 cP)** – **Wider print range** – **Suitable for rapid prototyping** – **Resolution up to 1 μm**	– **Initial set-up time is high** – **Rigorous cleaning of SPTs** – **Possibility of spillover of ink**

may also deteriorate device performance [51,52]. Further, bridging technology is utilized to interconnect the trench by nanowires [53]. A simple lift-up technique is used to connect the multiple CuO NWs on the electrode. Initially, thermally grown CuO NWs transferred to 1-butanol via sonication, and then transferred to a water-filled beaker. Later, a pre-patterned electrode is immersed and then pulled up to transfer CuO NWs between the electrodes [54].

To integrate a single nanowire (SNW) in a device, electron beam lithography and focused ion beam induced deposition process is used, this may disturb the NW surface and junctions [55]. The dielectrophoresis (DEP) technique is also used to fabricate NW devices; their small gap limits the highest voltage applied over the electrodes, which reduces the DEP force region; also, the contact area between electrode and NW is very narrow [41, 56]. In this context, microcantilever contact print (μCCP) is simple and less explored [57, 58]. The process is additive and requires low viscosity inks (10-18 cP) that offer the best feature-to-particle size ratio with a fine resolution of below sub-5 μm. The μCCP is highly suitable for rapid prototyping and can print a wider range. Table 1.2 lists the advantages and disadvantages of electrode deposition procedures for the fabrication of SNW devices.

TH-2675_186102019

1.4 Motivation and Problem Definition

Metal oxide devices exhibit outstanding performance, which can be used in various applications such as photodetectors and sensor applications. But most of the material synthesis and electrode fabrication includes sophisticated instruments. Preferably, low-cost synthesis and device integration are need of the hour for rapid design and development of devices to deploy in various applications. With this context, we have selected thermal oxidation to synthesize CuO NWs and microcantilever contact print to fabricate the electrodes.

Fig. 1.1 (a) shows the schematic of loading of the AgNP ink to the surface pattern tool (SPT) reservoir via micropipette to carry out the μCCP and (b) shows the printing of single CuO NW on the substrate. Fig. 1.2 shows the schematic of two terminal and three terminal CuO SNW devices fabricated using μCCP

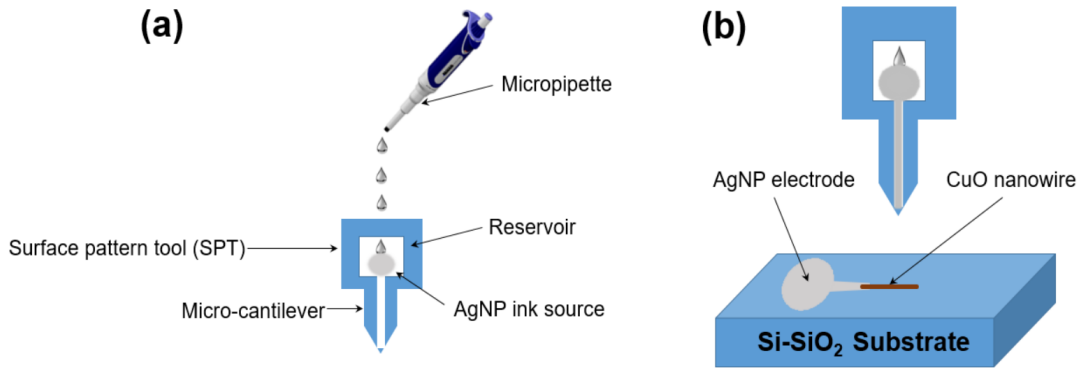

Fig. 1.1: (a) Schematic showing the loading of the AgNP ink to the surface pattern tool (SPT) reservoir via micropipette for μCCP (b) Printing of single CuO NW on the substrate

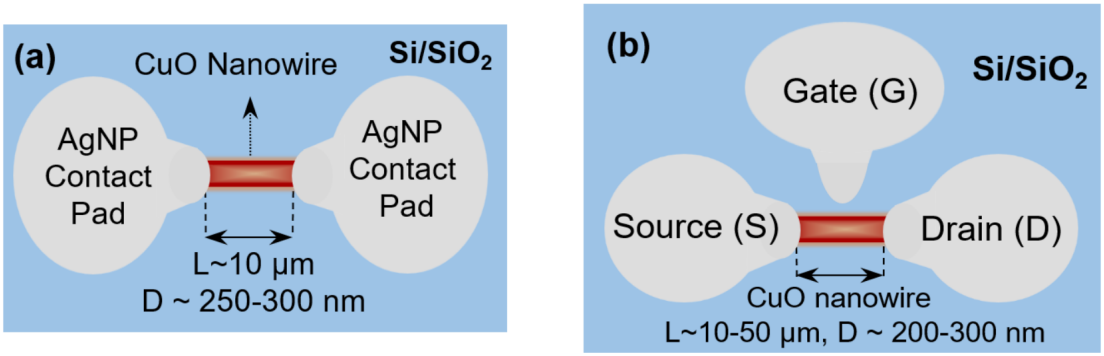

Fig. 1.2: Schematic of (a) Two terminal CuO SNW device (b) Three terminal CuO SNW device

TH-2675_186102019

The main objectives of the thesis can be listed as follows:

- Fabrication of CuO SNW device as a white light photodetector using μCCP.
- CuO SNW devices study at lower bias voltages for the anomalous response.
- Design and development of controlled environment chambers (CECs) for sensing gases and VOCs.
- Fabrication of CuO SNW back-to-back Schottky diodes of diffrent channel lengths and FETs for the detection of VOCs.
- Fabrication of CuO SNW FETs with back, coplanar, and top gate configuration.
- Solution-processed planar printed capacitors and FETs.

1.5 Thesis Outline

The thesis has been organized into six chapters. The contents of each chapter can be briefly outlined as follows.

Chapter 1 is a general introduction detailing the importance of metal oxide one-dimensional nanostructures in photodetectors, VOCs and gas sensing. Also, CuO nanostructure synthesis methods and device fabrication techniques are reviewed, along with the motivation, problem definition and organization of the thesis work.

Chapter 2 includes two parts; the first part covers the fabrication of CuO SNW back-to-back Schottky diode for white light detection. The device fabrication includes the synthesis of nanowires by thermal oxidation of copper, followed by μCCP of silver nanoparticles (AgNP) electrodes. The AgNP/CuO SNW/AgNP device reveals a sharp rise and recovery for continuous operation under the bias stress. Further, the fabricated device exhibits a remarkable white light photodetection. The second part covers the experimental investigation of irregularities in the device response at lower bias voltages.

Chapter 3 includes two in-house designs and also the development of sensing measurement systems. The first controlled environment chamber (CEC 2.0) is developed to update the existing sensing setup (CEC 1.0), which is of dynamic measurement type; uses mass flow controllers (MFCs) to regulate the

TH-2675_186102019

gas flow. The second VOC sensing system consists of an airtight borosilicate glass chamber; the desired concentration of the VOC in the chamber is achieved by the static liquid gas distribution method.

Chapter 4 includes a CuO SNW based metal-semiconductor-metal (MSM) structure for the detection of VOCs. Devices with channel lengths 10, 20, and 30 μm are employed to detect VOCs such as ethanol, acetone, and 2-propanol, etc., with concentrations ranging from 25-100 ppm. In the initial stage, sensing is carried out at room temperature. The device exhibits a poor response; later sensing is carried out at 150 °C, and in white light (1 mWcm^{-2}). The device has limited performance under these conditions and shows stable performance for four months.

Chapter 5 includes two parts; the first part covers CuO SNW FET with back gate, coplanar, and top gate configuration. The back gate and coplanar gate uses SiO_2 as gate oxide. The top gate configuration uses a solution of 0.3 M concentration of aluminum nitrate nonahydrate printed using μCCP as gate oxide. The challenges associated with CuO SNW FET realization are analyzed. The second part covers a fully printed metal-insulator-metal(MIM) capacitor and adjacent gate FET. For oxide and channel printing, aluminum nitrate nonahydrate and sodium molybdate dihydrate inks are respectively used; AgNP is used for the electrodes.

Chapter 6 presents conclusive remarks for this work and a brief discussion on future scope of this work.

TH-2675_186102019

2

Fabrication of CuO Single-Nanowire Based White-Light Photodetector

Contents

TH-2675_186102019

2.1 Introduction

Transition-metal-oxide (TMO) nanostructures exhibit novel perspectives in chemical, mechanical, and optoelectrical properties associated with a size and dimension, targeting various potential applications. The material synthesis and integration to develop devices for photodetectors, optical switches, and solar cells based on nanostructures with various geometries such as flowers, cubes, rods, wires, boats, fibers, etc., have a great research interest in recent years [19–21, 40]. The photodetector devices can be fabricated with two terminal or FET configurations. Along with the device configurations, contact to the material could be engineered either by Schottky or ohmic using different metals as electrodes. However, one-dimensional (1D) nanostructures have been a prime focus for nano-devices due to its unique physical and optoelectrical properties. SN Das *et al.* fabricated a ZnO single NW-based device using e-beam lithography with ohmic and Schottky interface for the low-power UV detection [59]. Ga–In bimetallic NWs have been synthesized using the electrospinning method and fabricated a photodetector to detect deep-UV with very high responsivity [14]. LB Luo *et al.* fabricated CuO SNW photodetectors on the flexible PET substrate [50]. A García Marí *et al.* synthesized CuO NWs by direct oxidation of copper, then CuO NWs deposited on n-type ZnO:Al electrodes by dielectrophoresis. The heterostructure light sensors detect white light and exhibit fast response [41].

Several synthesis methods are reported to achieve the CuO 1D nanostructures, such as wet chemical methods, sputtering, template-assisted synthesis, thermal oxidation, electrospinning [43, 44, 46–49, 60]. CuO 1D nano-device fabrication involves high purity material synthesis followed by effective metal contact to exploit the optoelectronic properties.

This chapter covers the fabrication of CuO single-nanowire (SNW) back-to-back Schottky diode for white light detection. The device fabrication includes the synthesis of nanowires by thermal oxidation of copper, followed by microcantilever contact print (μCCP) of silver nanoparticles (AgNP) electrode. The metal-semiconductor-metal (MSM) structure exhibits a dark current of 1.40 nA and photocurrent of 2.55 μA for $\pm$6 V bias. The AgNP/CuO SNW/AgNP device reveals a sharp rise and recovery for continuous operation under the bias stress. Further, the fabricated device exhibits a remarkable photodetection with the highest photosensitivity, responsivity, detectivity, and external quantum efficiency (EQE). The printed devices have an irregular response in the lower bias voltage in dark and white light conditions. A wide range of material and device characterization is performed to understand the CuO SNW material, interface, and electrical properties.

TH-2675_186102019

2.2 Materials and Methods

CuO NWs are grown using high-purity copper (Cu) wires (99.99%) of 0.5 mm diameter using thermal oxidation [60]. AgNP ink (Product Id: 736481) is procured from Merck, India, and used as received from the supplier. The Nano eNabler system and its surface patterning tools (SPTs) are used to fabricate the devices. Si-substrate with 300 nm SiO_2 oxide layers is used as a substrate.

2.2.1 Synthesis of CuO NWs

Cu wires are cleaned with acetone by ultrasonication for 5 min to clean grease, followed by cleaning with deionized (DI) water. Then, Cu wires are ultrasonicated in 0.5 M hydrochloric acid for 90 s to remove the oxide of the surface, followed by rinsing with DI water and dried with N_2. After the thorough clean, thermal oxidation of Cu wires is carried out at temperature 640 °C for 12 h in open atmosphere using a muffle furnace; further Cu wires are cooled down to room temperature naturally. Fig. 2.1 shows the schematic of CuO NWs synthesis. When copper is heated in the atmospheric air, the primary product is Cu_2O, and CuO will form slowly via the oxidation of Cu_2O; hence Cu_2O serves as a precursor to form CuO and its NWs.

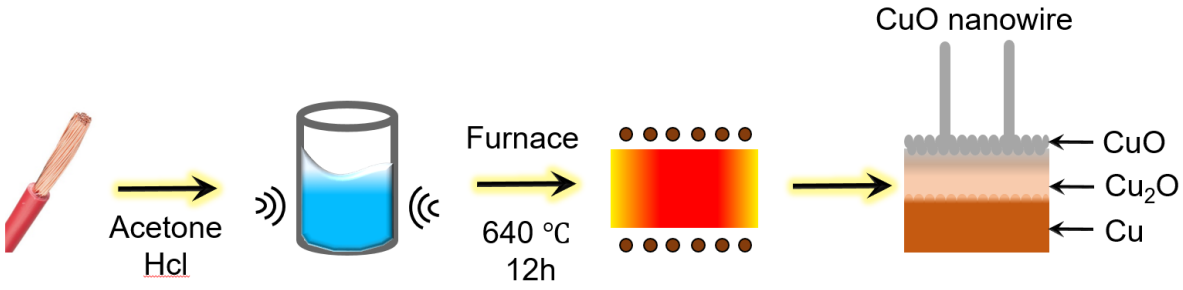

Fig. 2.1: Schematic of the CuO NWs synthesis.

2.2.2 Fabrication of CuO SNW Device

Thermal oxidation of Cu wires yields CuO NWs on the Cu substrate. The NWs are then transferred to a clean Si/SiO_2-substrate by gentle mechanical scrape, which results in the distribution of CuO NWs over the substrate. Fig. 2.2 shows the schematic representation of the mechanical scrape; (a) shows the oxidized copper wire along with NWs on the surface before the scrape, and (b) shows the NWs distribution on the substrate when the tweezer travels along the scraping path. The electrodes are then printed over a well-separated NW on the Si/SiO_2-substrate. AgNP ink is used to print the contact

TH-2675_186102019

pads (electrodes) in a sequence. μCCP is carried out using surface patterning tools by employing spot overwrite and drag printing techniques [61]. The first contact pad to the NW is annealed at 60 °C to dry the ink to avoid further spread in the subsequent printing process. After the second contact pad printing, the Si/SiO_2-substrate is annealed from 60 °C to 200 °C with a rate of 2 °Cmin^{-1} and then gradually cooled down to the room temperature.

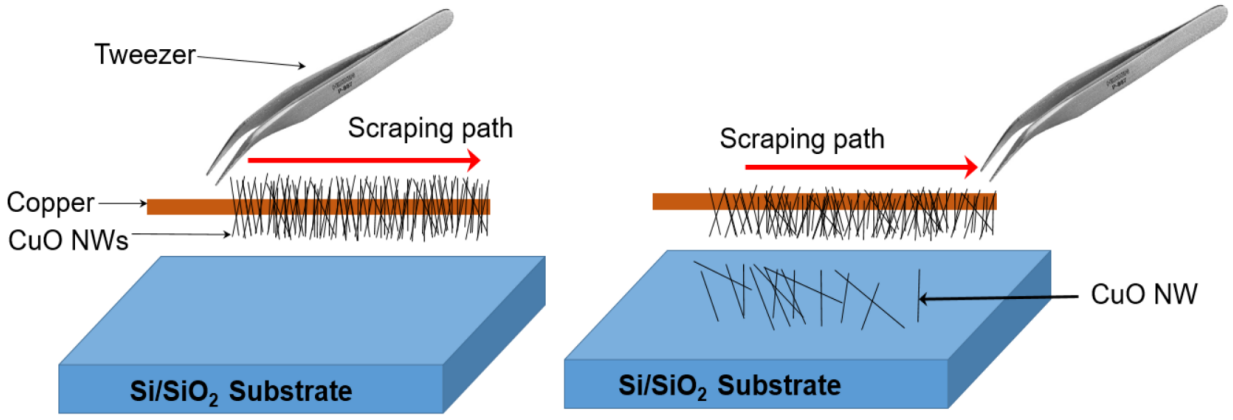

Fig. 2.2: Schematic representation of the mechanical scrape (a) Oxidized copper wire along with NWs on the surface before the scrape (b) CuO NWs on substrate after the scape with tweezer

2.3 Results and Discussion

2.3.1 Material Characterization

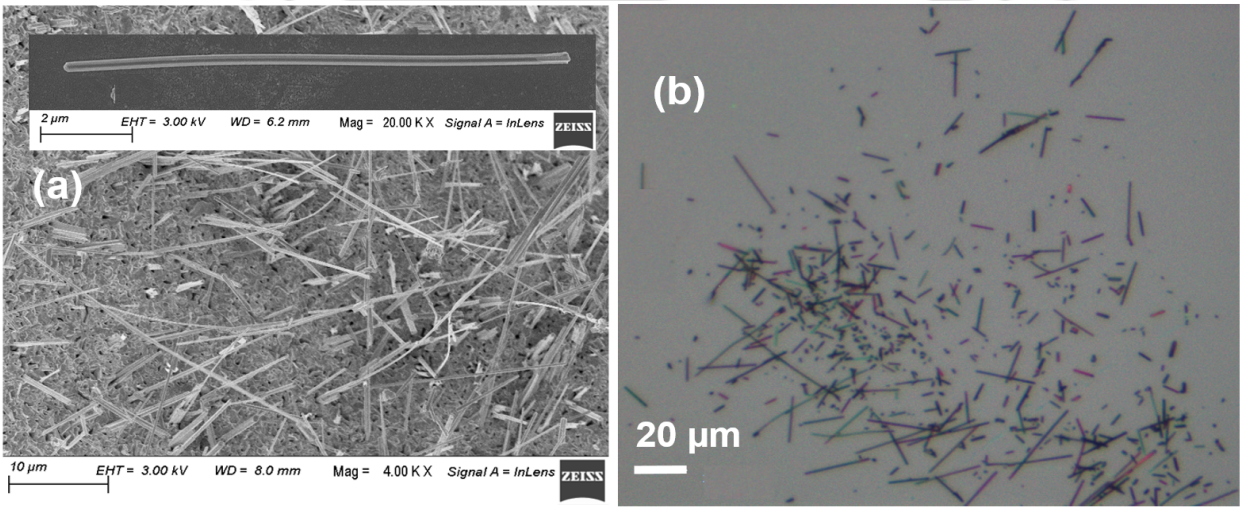

Fig. 2.3: (a) SEM image of CuO NWs on Cu wire. (b) Optical image of the NWs on the Si-substrate.

Fig. 2.3(a) shows the field-emission scanning electron microscopy (FESEM) [Make: Zeiss, Model:

TH-2675_186102019

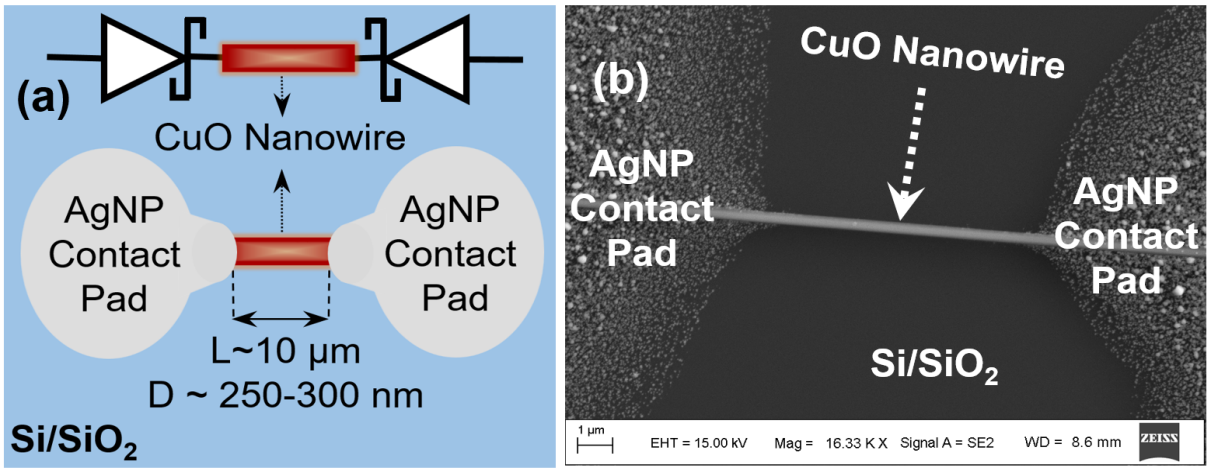

Fig. 2.4: (a) Schematic of the CuO SNW photodetector, L: length and D: diameter. (b) SEM image of CuO SNW device.

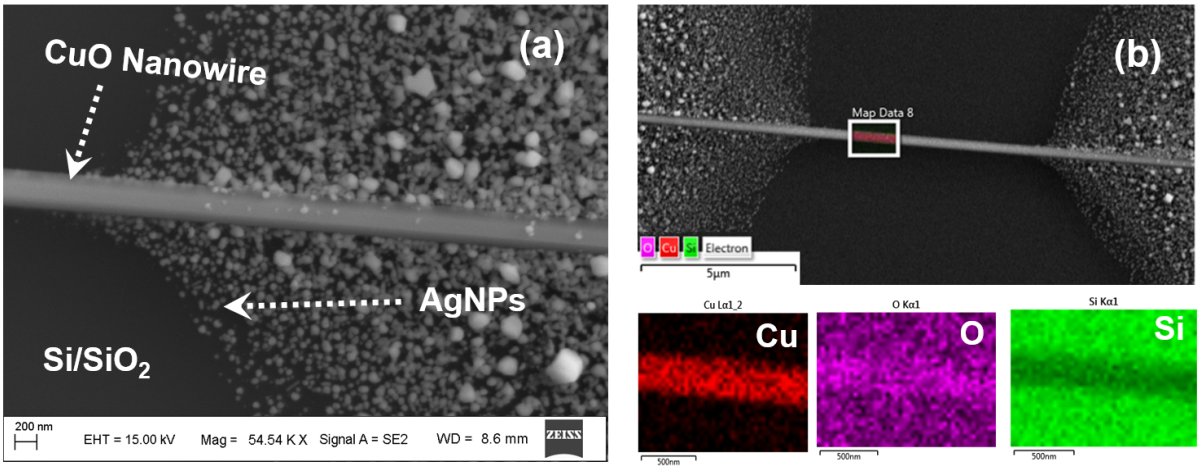

Fig. 2.5: (a) SEM image of CuO SNW/AgNPs interface. (b) SEM image of the CuO SNW device highlighting the CuO NW for the elemental mapping. Elemental mapping of the highlighted area indicating the presence of Cu, O, and Si.

Sigma] of CuO NWs on the Cu wire after the thermal oxidation. The inset in Fig. 2.3(a) shows one of the CuO SNW on Si/SiO_2-substrate after the mechanical scrape. Fig. 2.3(b) shows the optical image of the CuO NWs on Si/SiO_2-substrate, after the mechanical scrape. The schematic of the CuO SNW device is shown in Fig. 2.4(a); the fabricated photodetector FESEM image is shown in Fig. 2.4(b). The device has CuO SNW of length 10 μm and diameter 250 nm. Fig. 2.5(a) shows the SEM image of the CuO SNW/AgNPs interface. The elemental mapping of CuO SNW is obtained via energy-dispersive X-ray spectroscopy (EDS) as shown in Fig. 2.5(b). Elements Cu, O, and Si are found; Si and O are spread due to Si/SiO_2 substrate.

TH-2675_186102019

Fig. 2.5(a) shows the SEM image of the CuO SNW/AgNPs interface. The elemental mapping of CuO SNW is obtained via energy-dispersive X-ray spectroscopy (EDS) as shown in Fig. 2.5(b). Elements Cu, O, and Si are found; Si and O are spread due to Si/SiO_2 substrate. To verify the oxidized Cu substrate structural properties, X-ray Diffraction (XRD) [Make: Rigaku, Model: Micromax-007HF] spectra are obtained as shown in Fig. 2.6(a). The peaks are well matched with standard JCPDS data 00-005-0661 and 00-005-0667. The growth follows a two-layer microstructure, consisting of a Cu-rich Cu_2O phase on Cu substrate, over which CuO is the topmost layer in a diffusion-limited metal oxidation process [49]. The UV-Vis absorbance spectra are recorded [Make: Shimadzu, Model: UV-2600] as shown in Fig. 2.6(b). The optical band gap energy is obtained using the Tauc plot [40, 42], as shown in Fig. 2.6(c) and (d) by extrapolating the line segment. The general equation of the method is as follows

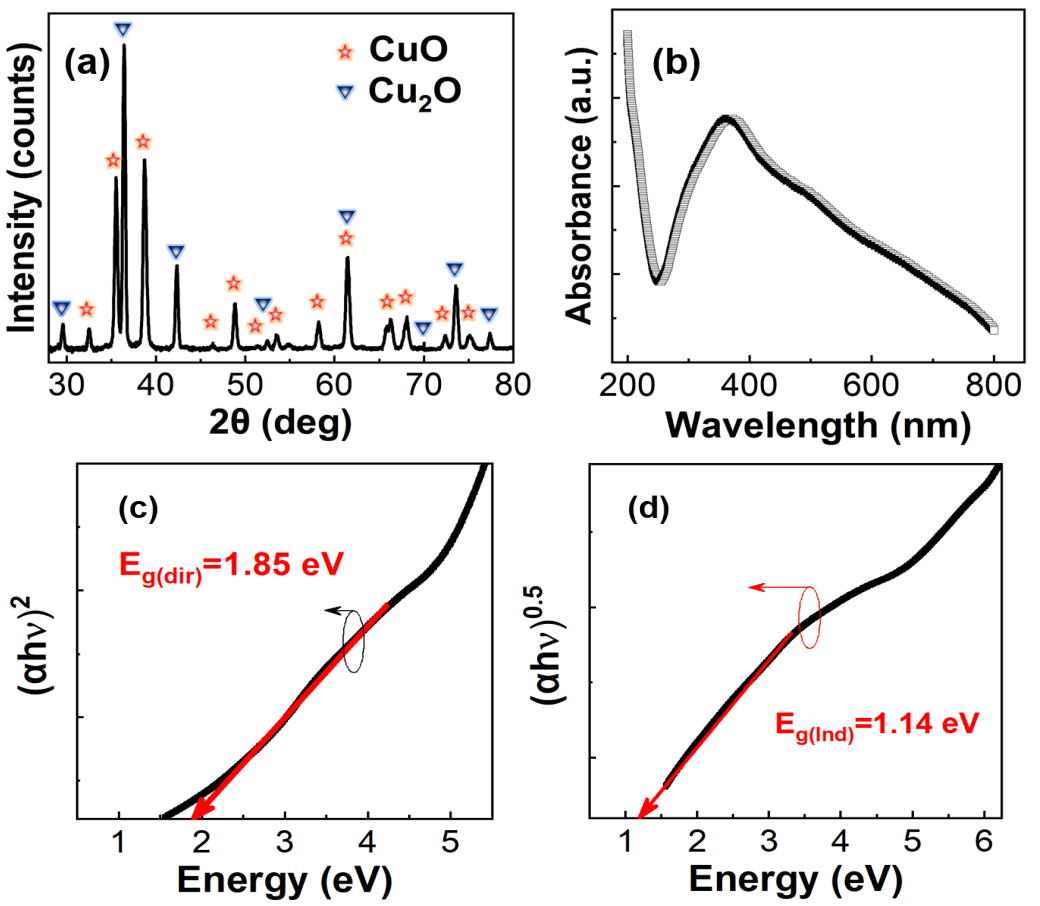

Fig. 2.6: (a) XRD spectrum of thermally oxidized copper wire. (b) UV-Vis absorption spectra of CuO NWs. Tauc plot: (c) direct and (d) indirect transitions.

TH-2675_186102019

$$(\alpha h\upsilon)^n = K(h\upsilon - E_g) \tag{2.1}$$

where α is the absorption coefficient, K is energy independent constant, E_g is the semiconductor bandgap, and n is the nature of the transition which can take value 2, $\frac{1}{2}$, $\frac{2}{3}$, and $\frac{1}{3}$, direct, allowed direct, forbidden direct, and forbidden indirect transitions.

2.3.2 Electrical Characterization

The electrical characterization has been carried out at room temperature using a source meter [Make: Keithley, Model:4200A-SCS] and a DC probe station [Make: EverBeing, Model: BD6]. White LED light sources with variable intensity and a light meter [Make: Gentec-EO, Model: Pronto-Si] are used for optical measurements. Xenon lamp with a monochromator [Make: Newport] is used for the spectral response. Fig. 2.7(a) and (b) shows the dark current and photocurrent with applied bias voltage ±10 V at 10 mV step. The photodetector I-V corresponds to back-to-back Schottky diode behavior.

The photocurrent in Fig. 2.7(a) and (b) are measured with irradiating white light intensity 16 $mWcm^{-2}$. Fig. 2.7(c) shows the photoresponse-current-transient of light power ranging from 500 $nWcm^{-2}$ to 16 $mWcm^{-2}$, with bias voltage -6 V. Fig. 2.7(d) also shows the dynamic photoresponse of the device obtained by switching the photoexcitation (16 $mWcm^{-2}$) on and off with 6 V bias. The device current during the excitation is higher than three orders compared to the dark; meanwhile, the current recovers back to 1.40±0.1 nA for every cycle during the continuous operation under the bias stress for five hours. Furthermore, the rise (t_r) and fall (t_f) times are found to be 40 ms and 22 ms as shown in Fig. 2.8(a) and (b), respectively. The device spectral response is shown in Fig. 2.8 (c), performed with an intensity 90 μWcm^{-2} under bias -6 V by sweeping the wavelength from 200-900 nm with an increment of 10 nm. The device responds well in the visible region 380-750 nm.

The dark and light current transport mechanism is illustrated in the schematic band diagram, as shown in Fig. 2.9(a-c). The MSM structure at thermal equilibrium is shown in Fig. 2.9(a). Fig. 2.9(b) shows the device under bias condition without illumination, gives rise to dark current, mainly determined by thermionic emission of carriers at the reverse-biased junction. The depletion region is broad in the dark, limiting the carrier flow, in turn, the current. After exposure to the light, the photogenerated electrons are mostly trapped in the reverse-biased depletion region, as shown in Fig.

TH-2675_186102019

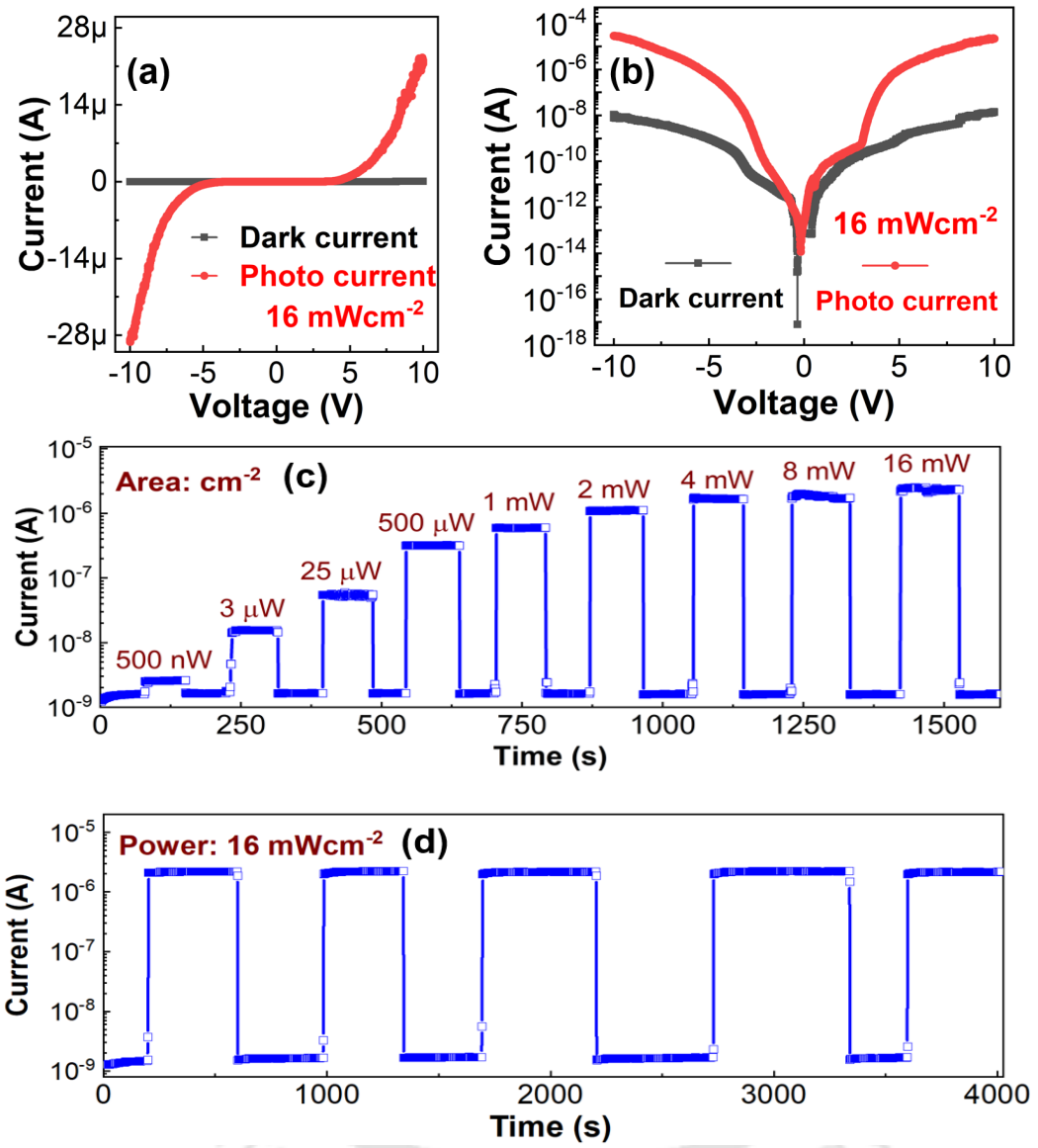

Fig. 2.7: CuO SNW I-V charactersitics (a) and (b), dark and photocurrent. Photoresponse-current-transient (c) at bias voltage -6 V, with light power 500 nWcm^{-2} to 16 mWcm^{-2} (k) at bias voltage 6 V with constant light power 16 mWcm^{-2}.

2.9(c). The charge redistribution in the depletion region thins down the barrier and allows the carrier to tunnel [62]. The device performance parameters such as photosensitivity (S), responsivity (R), detectivity (D), and external-quantum-efficiency (EQE, η) are calculated as follows

$$S = \frac{I_{ph}}{I_d} = \frac{I_l - I_d}{I_d} \tag{2.2}$$

$$R = \frac{I_{ph}}{AP_l} \tag{2.3}$$

TH-2675_186102019

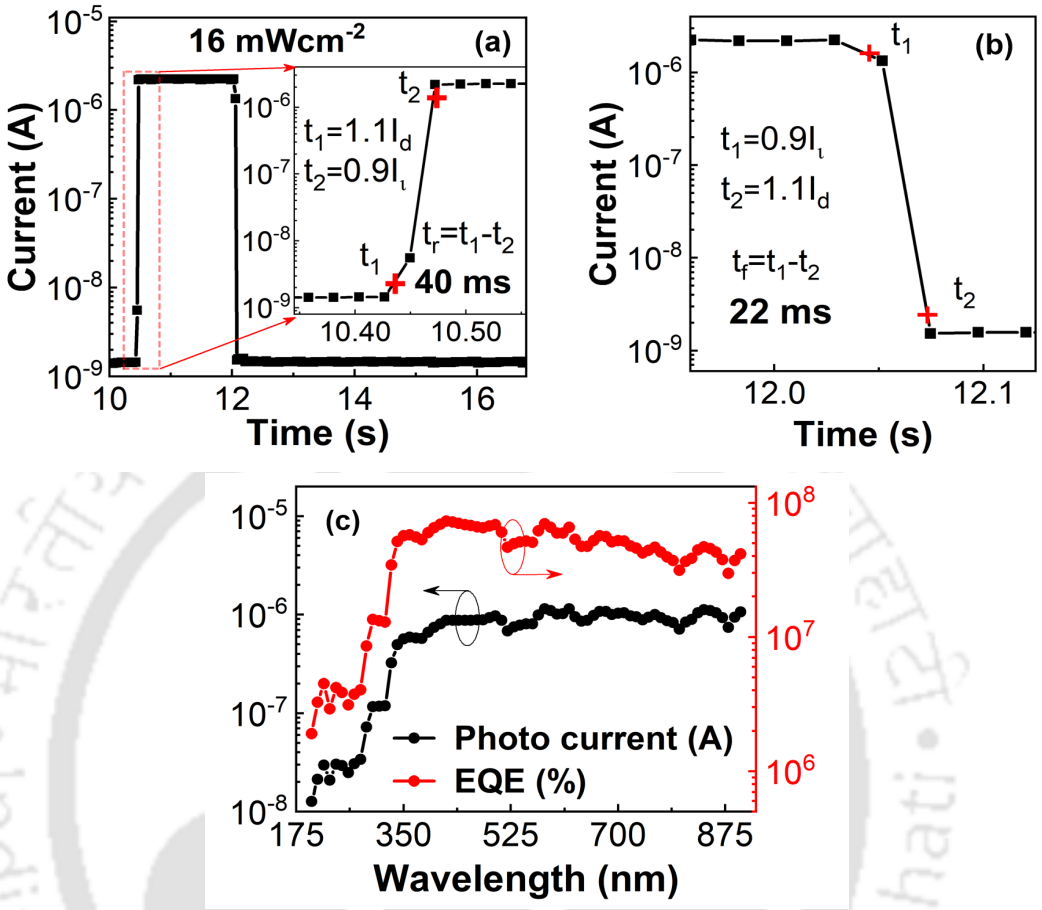

Fig. 2.8: (a) Rise time (40 ms), (b) Fall time (22 ms) for Cuo SNW biased at 6 V with light power 16 mWcm^{-2}. (b) Photocurrent and external-quantum-efficiency response to wavelength spectra 200-900 nm.

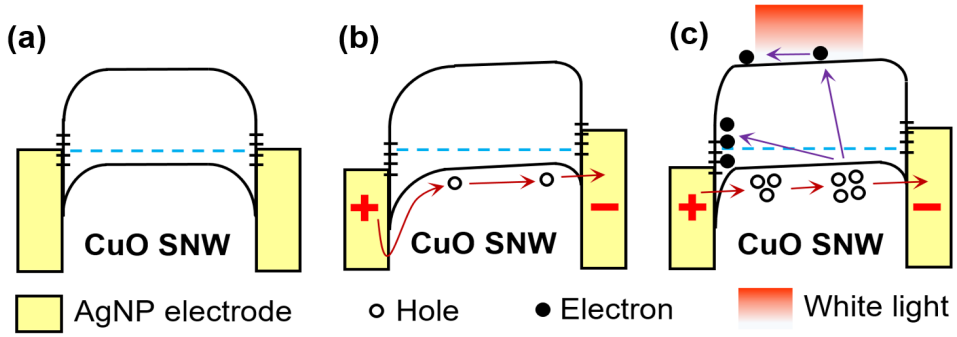

Fig. 2.9: Energy band diagrams of CuO SNW MSM structure (a) at thermal equilibrium. Biased with dark and light illumination are shown in (b) and (c) respectively.

$$D = \frac{RA^{0.5}}{(2qI_d)^{0.5}} \tag{2.4}$$

TH-2675_186102019

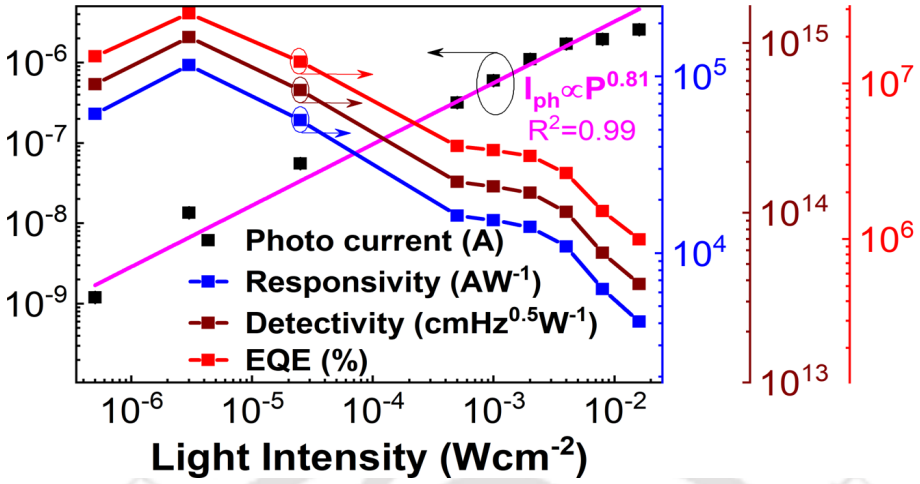

Fig. 2.10: Variation of photocurrent, responsivity, detectivity, and EQE with different white light power in logarithmic plot.

$$\eta = \frac{Rhc}{q\lambda} \tag{2.5}$$

where I_d is the dark current, I_l is the light current, I_{ph} is the photocurrent, A is the exposed area, P_l is the light intensity, and λ is the wavelength. h, q, and c are Plank's constant, electron charge, and speed of the light, respectively. Table 2.1 shows the computed values of S, R, D, and η for the white light intensity 16 mWcm^{-2} with a bias volatge -6V.

The dependency of I_{ph} and other performance parameters on the light intensity is shown in Fig. 2.10. Curve fit for the I_{ph} by a power-law yield the exponent 0.81 [63]. Power law illustrates the dependence of photocurrent on the light intensity can be represented as follows

$$I_{ph} = K_0 P^{\theta} \tag{2.6}$$

where K_0 is a constant, and the exponent θ defines the photocurrent response to light intensity. However, the device response at lower bias voltage ($\leq \pm 3$ V) for both dark and photoexcitation is bit anomalous, and its reason is still under investigation. The device's high performance could be

Table 2.1: CuO SNW photodector performance in white light 16 mWcm^{-2}

Performance parameters	Estimated value
Photosensitivity (S)	1820
Responsivity (R)	4085 AW^{-1}
Detectivity (D)	3.81×10^{13}cmHz$^{0.5}$ W^{-1}
External quantum efficiency (η)	7.23×10^{5} % to 1.27 $\times10^{6}$ %

TH-2675_186102019

Table 2.2: Comparison of recent CuO based photodetectors with our work

[Ref.] Device	CuO Morphology	Fabrication Methodology	Spectra (nm)	Power ($mWcm^{-2}$)	Dark current	Photo current	S	R ($A\ W^{-1}$)	D ($cm\ Hz^{0.5}\ W^{-1}$)	η (%)
[38] Al/Cuo/Al$^{\Psi}$	Nanorod array	AAO $^{\alpha}$	808	0.1	2.5 μA	18.2 μA	6.28	1.6	NA	139
[50] Au-Cu/Cuo/Cu-Au*	Single nanowire	Lithography$^{\alpha}$	600	2	≈1.75 nA	2.1 nA	1.2	200	6.38×10^{11}	$41.39 \times 10^{+3}$
[40] Au/CuO/Au†	NSs thin film	Shadow mask‡	210-290	NA	0.23 nA	140 nA	610	14.02	3.59×10^{13}	$5.90 \times 10^{+3}$
[42] Au/CuO/Au*	Thin film	Shadow mask‡	633	500	10 nA	100 nA	10	0.17	1.38×10^{11}	33.29
[66] Au/Ni-Cuo/Au$^{\Psi}$	Thin film	Shadow mask‡	635	5	400 nA	200 nA	0.5	3.3	0.32×10^{11}	644.32
[39] Cu/CuO/Cu$^{\Psi}$	Thin film	Shadow mask‡	250–900	5	200 pA	200 nA	1000	0.08	2.24×10^{11}	11.02
[41] AZO/CuO/AZO$^{\Psi}$	Nanowire network	Lithography$^{\phi}$	380-750	4.54	≈0.8 nA	160 nA	224	NA	NA	NA
[This work] AgNP/CuO/AgNP$^{\Psi}$	**Single nanowire**	**Printing**	**380-750**	**16**	**1.40 nA**	**2.55 μA**	**1820**	**4085**	**3.81×10^{13}**	**$9.95 \times 10^{+5}$**

$^{\Psi}$Back-to-Back Schottky Diode, †Resistor, *TFT, $^{\alpha}$e-beam evaporation, ‡thermal evaporation, $^{\phi}$Sputter and DEP, NA: Not Available

attributed as follows:

(i) Fig. 2.6(a) shows CuO NWs are highly crystalline, with no impurity peaks; this helps to confine the charge carriers in one-dimension.

(ii) Electrodes are printed, which is additive and does not alter the metal-semiconductor-metal interface significantly, as shown in Fig. 2.5(a).

(iii) The sharp response and recovery transitions during the on-off operation are due to the Schottky interface; AgNP (≈30 nm) with CuO (< 250 nm), where depletion width varies exponentially with photoexcitation as compared to square root dependence in case of bulk material [64]. Also, the absence of the oxygen vacancies may lead to fast separation of photogenerated electrons, and holes towards the AgNP electrodes [65].

(iv) The CuO NWs absorbs photons extensively in the visible region (380-750 nm), as shown in Fig. 2.6(b) with a peak at 365 nm.

Table 2.2 shows the comparison of the device performance parameters with recently reported devices using CuO [38–42, 50, 66]. The device response is in range and well maintained even after four months from the fabrication, which indicates the device has good stability.

2.4 CuO SNW Printed Devices Irregular Response Investigation at Lower Bias Voltages

To analyze the irregular response in the CuO SNW printed devices, further material characterization and device characterization have been carried to understand the root cause.

TH-2675_186102019

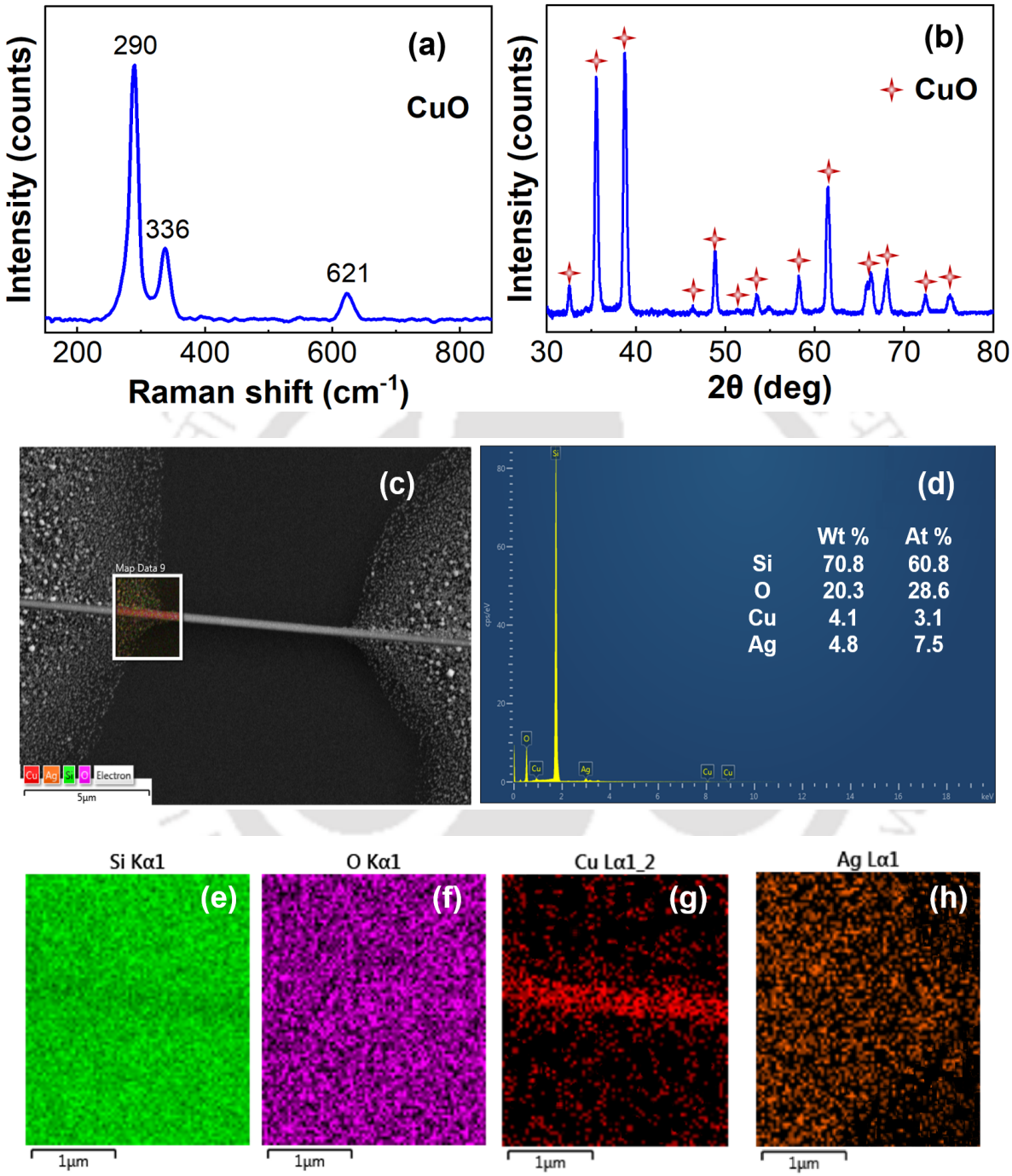

Fig. 2.11: (a) Raman spectra of CuO NWs. (b) XRD spectra of CuO NWs. (c) SEM image of the CuO SNW device highlighting the CuO NW and AgNP interface area for the elemental mapping. (d) EDS of the interface in Wt % and At %. Elemental mapping of the interface area indicating the presence of Si, O, Cu, and Ag (e-h), respectively.

TH-2675_186102019

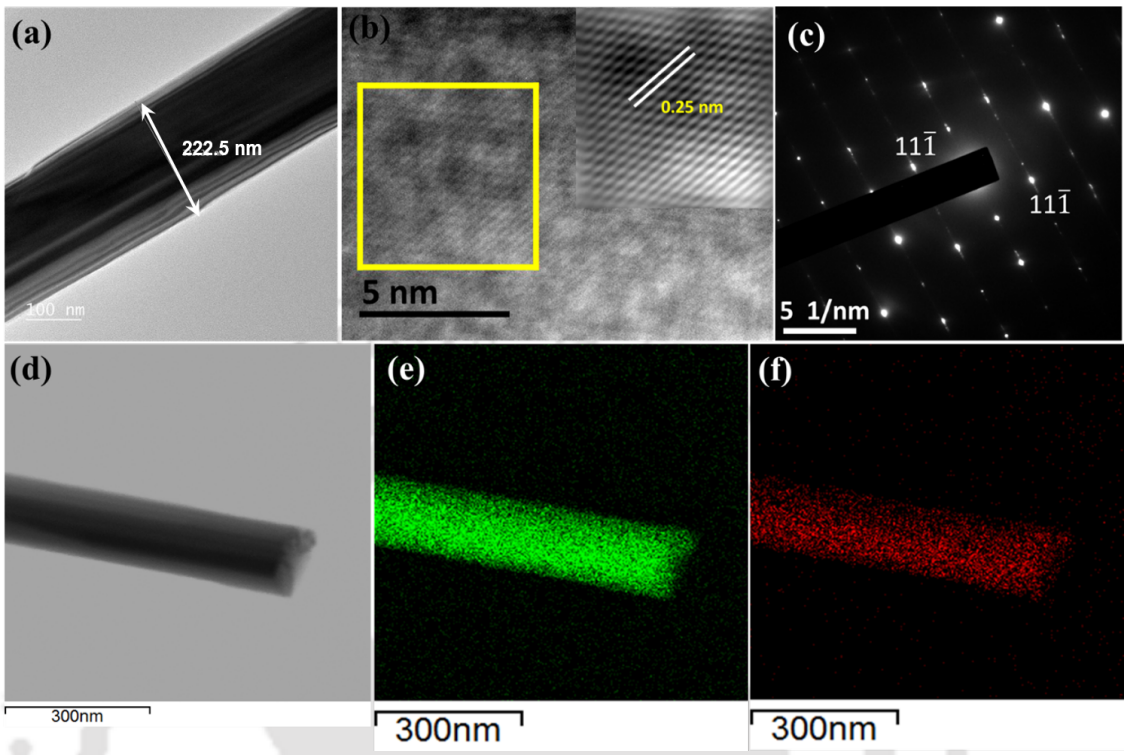

Fig. 2.12: (a) TEM image of the CuO NW. (b) High-resolution TEM and corresponding IFFT pattern. (c) SAED pattern of the as-prepared CuO NW. (d) TEM image of the CuO NW recorder during the elemental mapping. Elemental mapping of the same image indicating presence of Cu (e), and O (f).

2.4.1 Material Characterization

In this section, material characterization is performed in complement with section 2.3.1 to understand the CuO NWs structure, composition, and interface in detail. Fig. 2.11(a) shows the Raman spectra of CuO NWs [Make: Horiba, Model: LabRam HR Evolution]. A 532 nm laser source has been used for Raman scattering experiments. Characteristic peaks at 290, 336 and 621 cm^{-1} are identified. The peak appearing at 290 cm^{-1} is assigned as A_g mode of vibration. On the other hand, peaks at 336 and 621 cm^{-1} are assigned as B_1g and B_2g modes, respectively, characteristics of CuO nanowires (CuO NWs) [67]. XRD [Make: Rigaku, Model: Micromax-007HF] spectra are obtained as shown in Fig. 2.11(b). The peaks are well-matched with standard JCPDS data 00-048-1548, which indicates the CuO NWs are crystalline in nature. The composition at the CuO SNW and AgNP electrode interface is carried out by elemental mapping using EDS. The EDS has elements Si, O, Cu, and Ag with atomic % 60.8 %, 28.6 %, 3.1 %, and 7.5 %, respectively as shown in Fig. 2.11(e - h).

TH-2675_186102019

The TEM image in Fig. 2.12(a) confirms that nanowire is with 222.2 nm diameter. Furthermore, high-resolution TEM and corresponding inverse fast fourier transform analysis showed that highly crystalline nanostructures are formed with the calculated d-spacing value of 0.25 nm as shown in Fig. 2.12 (b). It is important to note that 0.25 nm d-spacing corresponds to 1 1 $\bar{1}$ plane in CuO nanostructure (Powder Diffraction File (PDF) No. 48-1548). The presence of 1 1 $\bar{1}$ lattice plane along with crystalline characteristics are also observed in the selected-area electron diffraction (SAED) analysis as in Fig. 2.12(c). Furthermore, as presented in Fig. 2.12 d-f, the material is composed of 58.7 % of Cu and 41.3 % of O, indicating that CuO is formed rather than Cu_2O.

2.4.2 Device Characterization

The CuO SNW printed devices' electrical response is carried out using a source meter [Make: Keithley, Model:4200A-SCS] and a DC probe station [Make: EverBeing, Model: BD6]. Fig. 2.13(a) shows the dark and photo IV characteristics by sweeping the voltage from -10 to 10 V with stepsize 100 mV in normal mode. Fig. 2.13(b) shows the enlarged portion of the device response, which has irregular behavior (i.e., -3 to 3 V); the device has the same response under fast mode too. Similar responses are reported with different step sizes (i.e., 25, 50, and 200 mV) under the normal and fast modes with ±5 % deviation. When the source meter is operated under quiet mode with a step size 5 mV and 10 mV, the responses are smooth as shown in Fig. 2.7(b); but couldn't find any current modulation between the dark and white light condition. The devices are further analyzed to investigate the reason.

(i) P Chand *et al.* shows the CuO nanostructures optical and ferroelectric behavior synthesized at different pH values [68]. In this direction, the device is tested with a ferroelectric tester [Make: Radiant Technologies, Model: Precision LCII 10kV HVI-SC] to measure the ferroelectric (P-E loops) properties. Despite the repeated attempts with different length devices, didn't get P-E loops, the reasons could be as follows:

   (a) The MSM structure has a length of 10 μm to 50 μm, polarization may be a difficult task in spite of the single-crystal material as shown in Fig. 2.12(c).

   (b) Interaction of CuO SNW with the atmosphere oxygen may change the conductivity and polarization of the material in the device [69, 70].

(ii) The device capacitance-voltage (C-V) characteristics are measured by applying the DC voltage

TH-2675_186102019

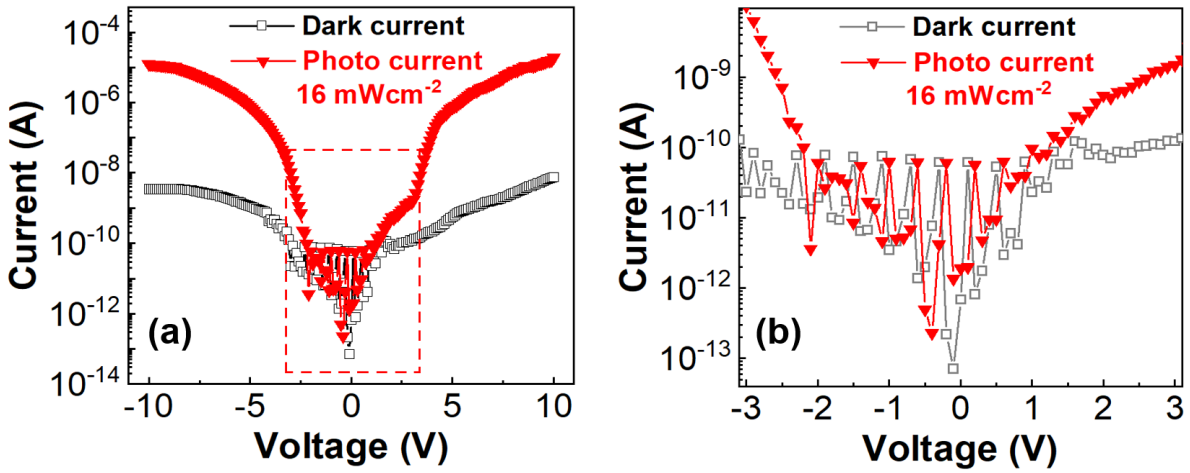

Fig. 2.13: CuO SNW I-V characteristics (a) dark and photocurrent in normal mode with 100 mV step. (b) Enlarged portion of the irregular response of (a) from -3 to 3 V.

from -4 to 4 V with 100 mV step at a frequency 100 kHz. Fig. 2.14(a) shows the variation of capacitance with the bias voltage for the device. C–V curves around the zero bias are bit non-symmetrical; but butterfly curves with a valley are hardly seen [71].

(iii) CuO SNW devices of length 10 μm to 50 μm have been fabricated and characterized; the dark and white light responses are similar to Fig. 2.14(a); with negligible deviations at higher voltage. The results indicate that the device length has little effect on the response and highlights the CuO/ AgNP junction effect. Fig. 2.14(b) shows the Responsivity (R) variations of the device over-voltage range 0 to 6 V.

(iv) DC voltage dual sweep is performed from -3 to 3 V with 10 mV step size under dark condition in quite-mode exhibits hysteresis as shown in Fig. 2.14(c) and (d). The hysteresis window in the IV data is very narrow along with less current range of femto to pico ampere. The white light condition has a similar hysteresis curve, indicating a negligible effect on the window size. Fig. 2.14(e) shows the dual sweep from 0 to -3 V; immediately same sweep is followed, and its IV is shown in Fig. 2.14(f). Its observed that in Fig. 2.14 (f), the initial current recorded is in reverse direction (i.e., 0 to -0.20V). The hysteresis observed in the AgNP/CuO-SNW/AgNP device at lower bias may attribute to restive switching offered by the CuO SNW [72–74].

It is mainly found that the interface between CuO SNW and AgNP electrode has a high barrier, which requires high bias voltage for the conduction. At high bias voltage, the MSM structure has

TH-2675_186102019

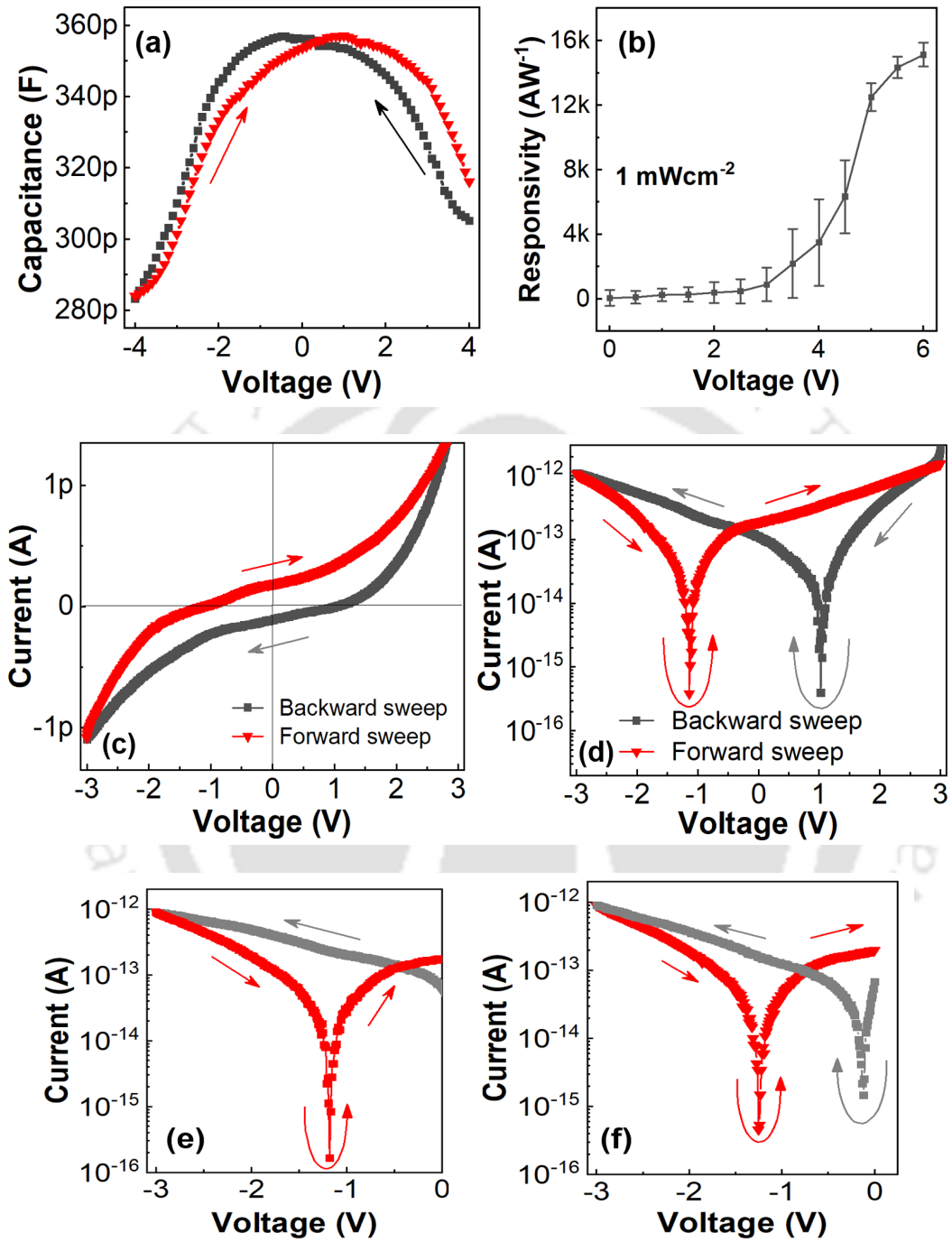

Fig. 2.14: (a) Relationship of capacitance versus the bias voltage for the AgNP/CuO-SNW/AgNP, $f = 100$ kHz. (b) Device response for 0 to 6 V with white light 1 mWcm^{-2}. (c) and (d) I-V characteristics, DC dual sweep -3 to 3 V with 10 mV step in quite mode. (e) and (f) I-V characteristics, DC dual sweep 0 to -3 V with 10 mV step in quite mode.

both forward and reverse-biased junctions. However, the flow of charge carriers is mainly limited by the reverse-biased junction. Under white light illumination, the depletion width of the reverse-biased

TH-2675_186102019

junction is thinned down and allows more charge carriers to flow across the junction [62]. Further, the device may be explored with different metal nanoparticles for photodetection and ferroelectric properties.

2.5 Summary

CuO SNW photodetector has been fabricated using low-cost thermal oxidation and printing technique. The CuO NW printed device reports a high sensitivity, responsivity, detectivity, and EQE. Moreover, the detector also reports fast response and recovery, 40 ms and 22 ms, respectively. The device has an irregular response in lower bias voltages; exhaustive material and device characterization is done to understand the cause.

TH-2675_186102019

TH-2675_186102019

3

Controlled Environment Chamber Design and Development for the Gas and VOC Sensor

Contents

TH-2675_186102019

3.1 Introduction

In sensor development, the measurement system is one of the crucial elements. Generally, static and dynamic gas sensing measurement systems are used [7–10, 75]; irrespective of the methods, gas or VOCs sensing measurement system has the following parts

(i) Chamber for the creation of a controlled environment for the analyte gas.

(ii) Ports, flow control valves, and regulators for the analyte and carrier gas.

(iii) Relative humidity (RH) generator with a regulator to maintain required RH in the chamber while sensing; also, heater and its controller to measure sensor response at elevated temperature.

(iv) Proper electrical feedthrough to take out/in signals from/to the chamber. Comprehensively electrical connection for sensor response measurement, heater, and light, etc., to be managed effectively.

(v) Pumps, plumbing, and fittings to direct the gas flow during the sensor measurement.

In some systems, the above parts may vary to meet the specific requirements. Gas and VOC sensing have been widely explored for many decades by modifying the materials and sensor design [26,37,76–81]. Few reports discussed the dependence of chamber design as an important factor in measuring sensor performance [82, 83]. Some studies have presented the effect of chamber shape, sensor placement, and volume on the gas-particle distribution in the chamber and on the sensor [84–86]. These factors affect the sensor characteristics and performance, viz. response, sensitivity, the limit of detection (LOD), and response and recovery time.

This chapter covers the design and development of two sensor measurement systems for the gas and VOC sensors. The first controlled environment chamber (CEC 2.0) is developed to update our lab's existing sensing setup (CEC 1.0) to overcome the shortcomings. The CEC 2.0 has mass flow controllers (MFCs) to regulate the gas flow continuously, known to be a dynamic system. The second VOC sensing setup consists of an airtight borosilicate glass chamber, and sensing is performed mostly in the presence of air. The desired concentration of the VOC in the chamber is achieved by the static liquid gas distribution method [87], a static system.

TH-2675_186102019

3.2 Controlled Environment Chamber (CEC 2.0)

3.2.1 CEC 1.0 Features

Our lab had an in-house developed CEC set up for measuring the sensor response, i.e., CEC 1.0. The in-house development provides first-hand information about various domains and also to work in the interdisciplinary areas. There is always scope for improving such a system. Following is the list of areas where the CEC 1.0 requires renovation.

(i) Volume: The sensing chamber had a capacity of approximately 9-10 L, which led to

  (a) Large consumption of analyte and carrier gas. Most of our analyte gas cylinders are of 3 L in size and get empty in a couple of experiments.

  (b) Variations in exposure time, in turn, affect the response time, recovery time, limit of detection (LOD), and sensitivity of the sensor [84]

(ii) Sealing: The chamber door had gasket sealing arrangement to isolate the chamber environment from the outside ambient, which led to leakage during the sensor measurement at desired pressure.

(iii) Chamber door: The chamber door had six hexagon cap nuts to seal the gasket; while closing the door every time, aligning and tightening nuts was tedious. Further, to avoid the leak, the user had to tighten all nuts rigorously to compress the gasket at maximum, which led to finger injuries. Moreover, each time opening/closing took approximately 15–20 minutes; also, the accessibility of backside nuts in the chamber for tightening/loosening was difficult.

(iv) Temperature: Inside the chamber, the sample temperature couldn't rise above the ambient during the measurement. However, the temperature of the analyte gas could be increased by using electric heat tape. In sensor research, sensor material is heated up most of the time for better sensor performance; in rare cases, analyte gas heats up.

(v) Feedthrough: Chamber had one DB 9-pin interface suitable for sensor response measurement (CF-35). Power feedthrough is required to set up a heater inside the chamber as the rating is different, but no such provision is made in CEC 1.0. On the other hand, using the existing DB-9 interface for sensor measurement and heater may not be wise. If the same feedthrough is used, the possibility of interference of sensor signals and power signals is high, especially if the sensor had a surface acoustic wave (SAW) configuration.

TH-2675_186102019

(vi) Bubbler: The bubbler setup was not present in CEC 1.0, which is essential to connect the VOC/liquid source.

3.2.2 CEC 2.0 Design Highlights

To overcome CEC 1.0 shortcomings as mentioned above; CEC 2.0 design and development is proposed

(i) Volume: The new sensing chamber is cylindrical and has a minimum volume, ≈1.5 L.

(ii) Sealing: The new chamber door has an O-ring sealing, which is most appropriate instead of the gasket.

(iii) Chamber door: The chamber door has a knurled nut instead of six hexagon cap nuts to seal with an O-ring, which quickly makes the loading and unloading process of the sensor and is safe for the operator as well. Spare C-type clamps are provided to the chamber door to seal further.

(iv) Temperature: CEC 2.0 has a heater in which the temperature can reach 400 °C, which helps to check the sensor's response at elevated temperatures.

(v) Feedthrough: CEC 2.0 has a power feedthrough for the heater to connect with the PID controller, power supply, and thermocouple. Sensor measurement signals are connected via a DB-9 interface.

(vi) Bubbler: CEC 2.0 has a bubbler that can hold liquid/VOCs of 50 ml connected in line to perform

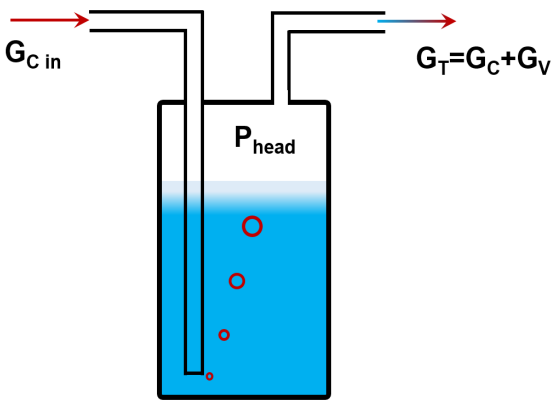

Fig. 3.1: Schematic of the bubbler for the VOC sensor setup.

TH-2675_186102019

the VOCs sensing. The flow rate of VOC vapor in the bubbler is as follows.

$$G_T = G_C + G_V \tag{3.1}$$

where G_T is the total gas flow, G_c is carrier gas flow, and G_v is VOC vapour flow

$$G_T = G_{Cin} \times \frac{P_v}{P_{head} - P_v} + G_{Cin} \times \frac{P_{head}}{P_{head} - P_v} \tag{3.2}$$

where G_{Cin} is carrier gas flow, P_v is vapour pressure, and P_{head} is pressure in the headspace of the bubbler. The schematic of the bubbler is shown in Fig. 3.1.

3.2.3 CEC 2.0 Plumbing Layout

Fig. 3.2 shows the schematic layout of CEC 2.0 consisting of three Mass Flow Controllers (MFCs) [Make: Alicat Scientific] with different flow rates 0 to 5 liters per minute (LPM), 0 to 0.5 LPM, and 0 to 0.01 LPM. The MFCs are configured in such a way that the carrier gas and analyte gas are regulated precisely using a proportional-integral-derivative (PID) controller. MFCs, along with the mixing unit, could obtain the analyte gas (test gas) in low concentrations in ppm and ppb ranges. Computer with Alicat's Flow Vision MX^{TM} gas-blending software is used to regulate the gas flow in the SS316 $\frac{1}{4}$ inch pipe with metal compression fittings. The pressure regulator is used to maintain the required pressure in the sensing chamber. The unidirectional valves with auto cut-off switch are used to ensure any pressure fluctuations during pressurizing the sensing chamber and evacuating. RH generator is connected with the sensing chamber, which facilitates carrying out RH-related experiments and maintains the required RH during the sensing.

Solid works 2019 CAD tool is employed to draw the engineering drawings in detail for the CEC 2.0 parts and assembly. The salient features of the chamber design are as follows: SS 316 material is used to fabricate the chamber with an approximate volume of 1.5 L (Cylindrical shape with a 150 mm outer diameter and a height of 150 mm). Separate feedthrough are provided for power (CF-16) and sensor measurement signals (CF-35, DB-9). Three ports are provided to control the flow of gases, along with the viewport of OD 60 mm. The top door of the chamber has a hinge connection on one side and knurled nut on the opposite side with an O-ring seal for the easy accessibility of the loading and unloading of the samples/sensor. Fig. 3.3 shows the assembly drawing of the sensing chamber and associated parts. The chamber assembly has more than twenty-five parts—the drawing of each part

TH-2675_186102019

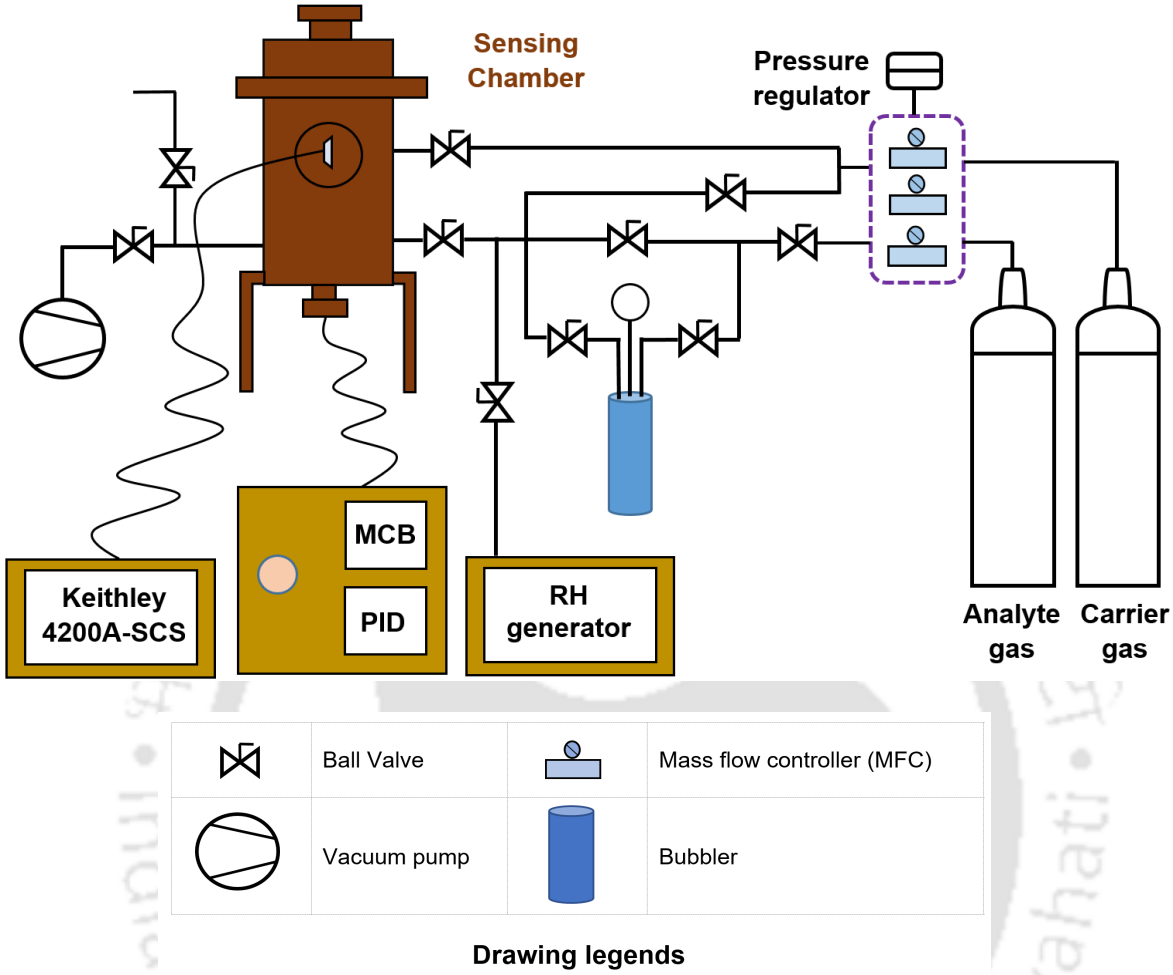

Fig. 3.2: Schematic of the proposed new sensing setup CEC 2.0 with plumbing layout.

is detailed except the standard parts, but in the thesis, the drawings of important parts such as CEC Base, CEC Top are shown in Fig. 3.4 and 3.5 respectively. Fig. 3.6 shows bubbler assembly and its associated parts. The bubbler base is designed to hold 50 ml of the liquid/VOC using SS 316 material. Bubbler base is sealed with KF-40 at the top for easy handling while conducting the sensing. The positioners are used to keep the probing crocodile clips and sample at desired positions on the sample holder stud. Sensing can be carried out from room temperature to elevated temperature up to 400 °C by using the heater.

TH-2675_186102019

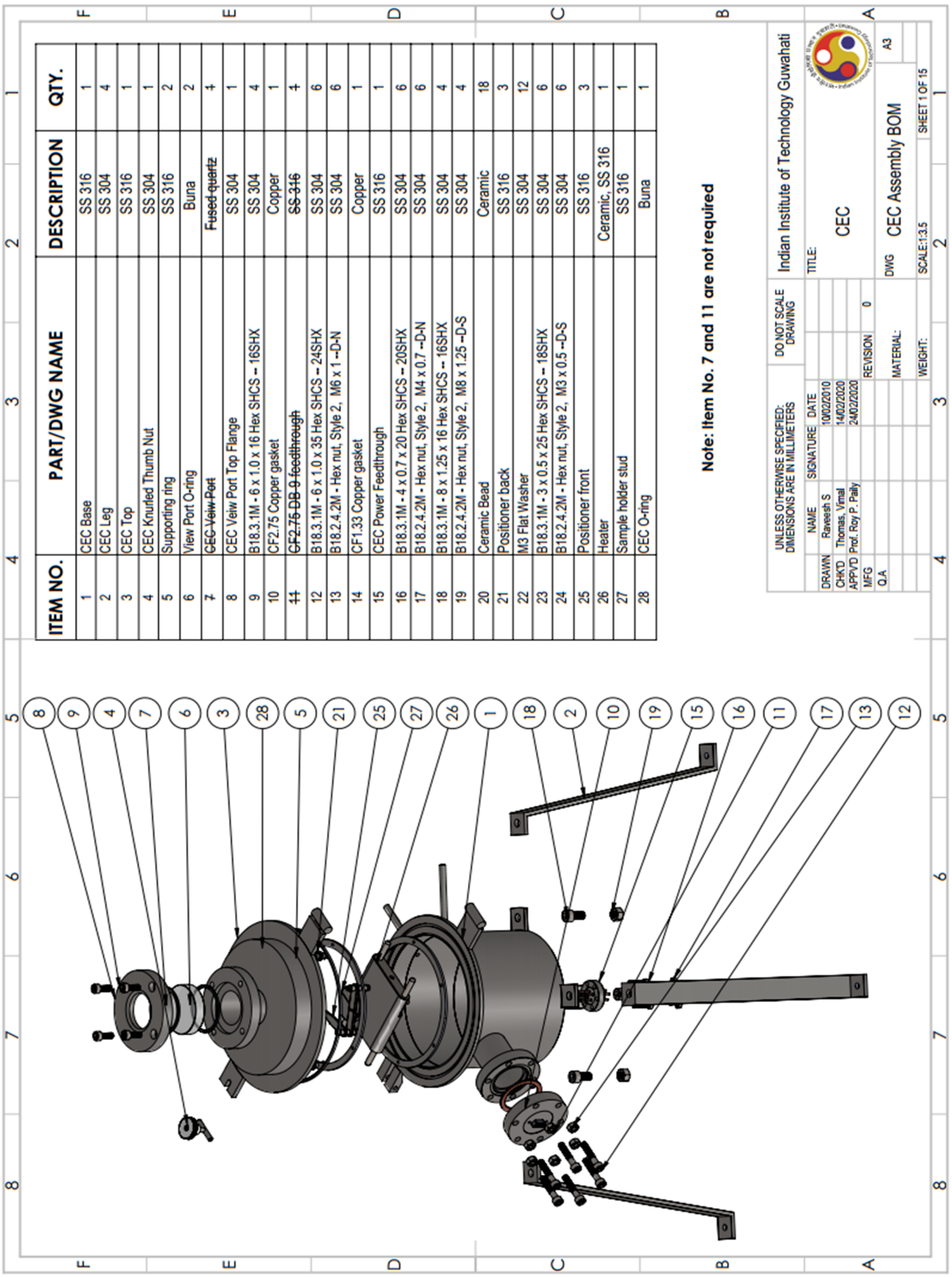

Fig. 3.3: Sensing chamber parts and assembly drawing.

TH-2675_186102019

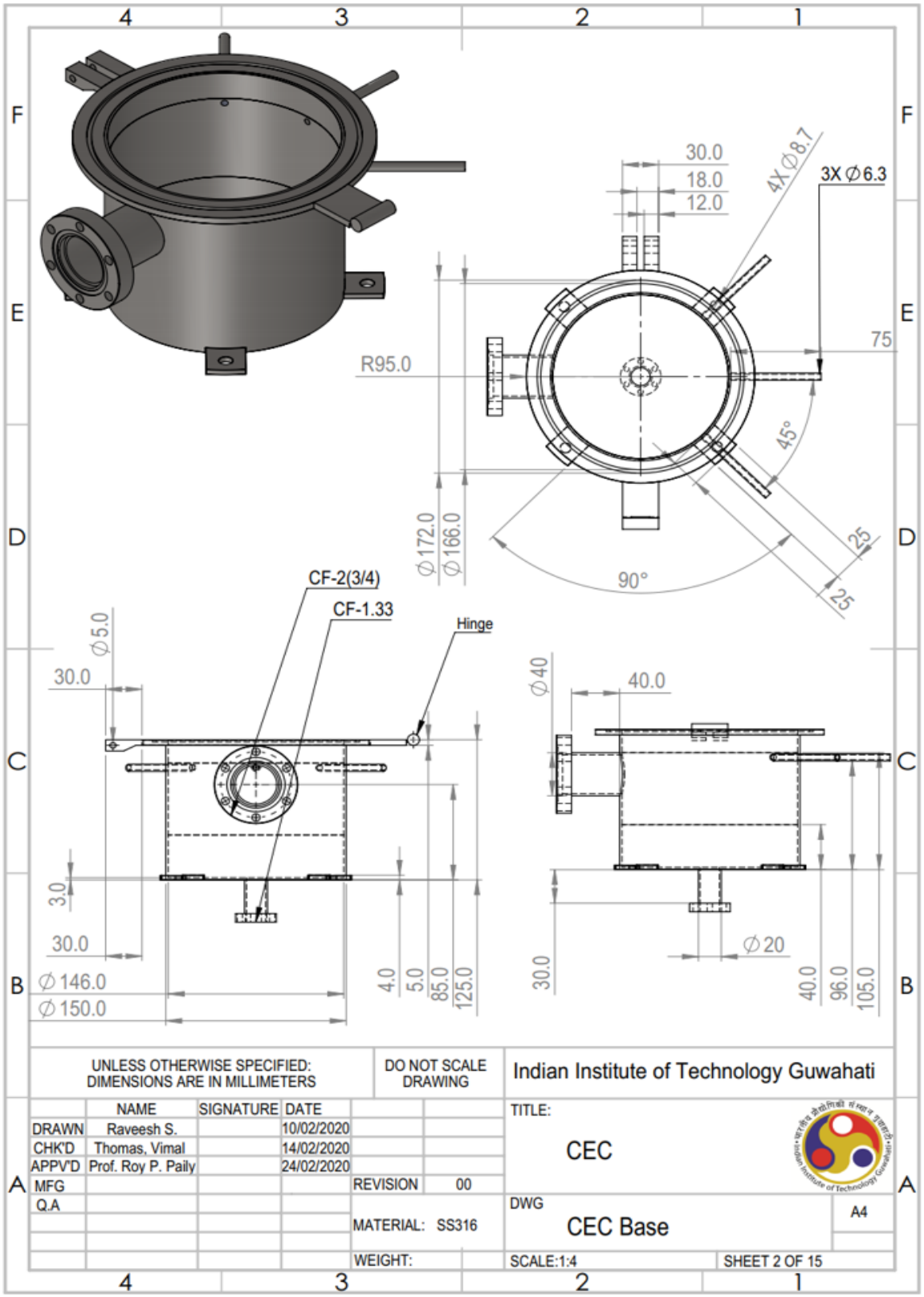

Fig. 3.4: Sensing chamber base part drawing details.

TH-2675_186102019

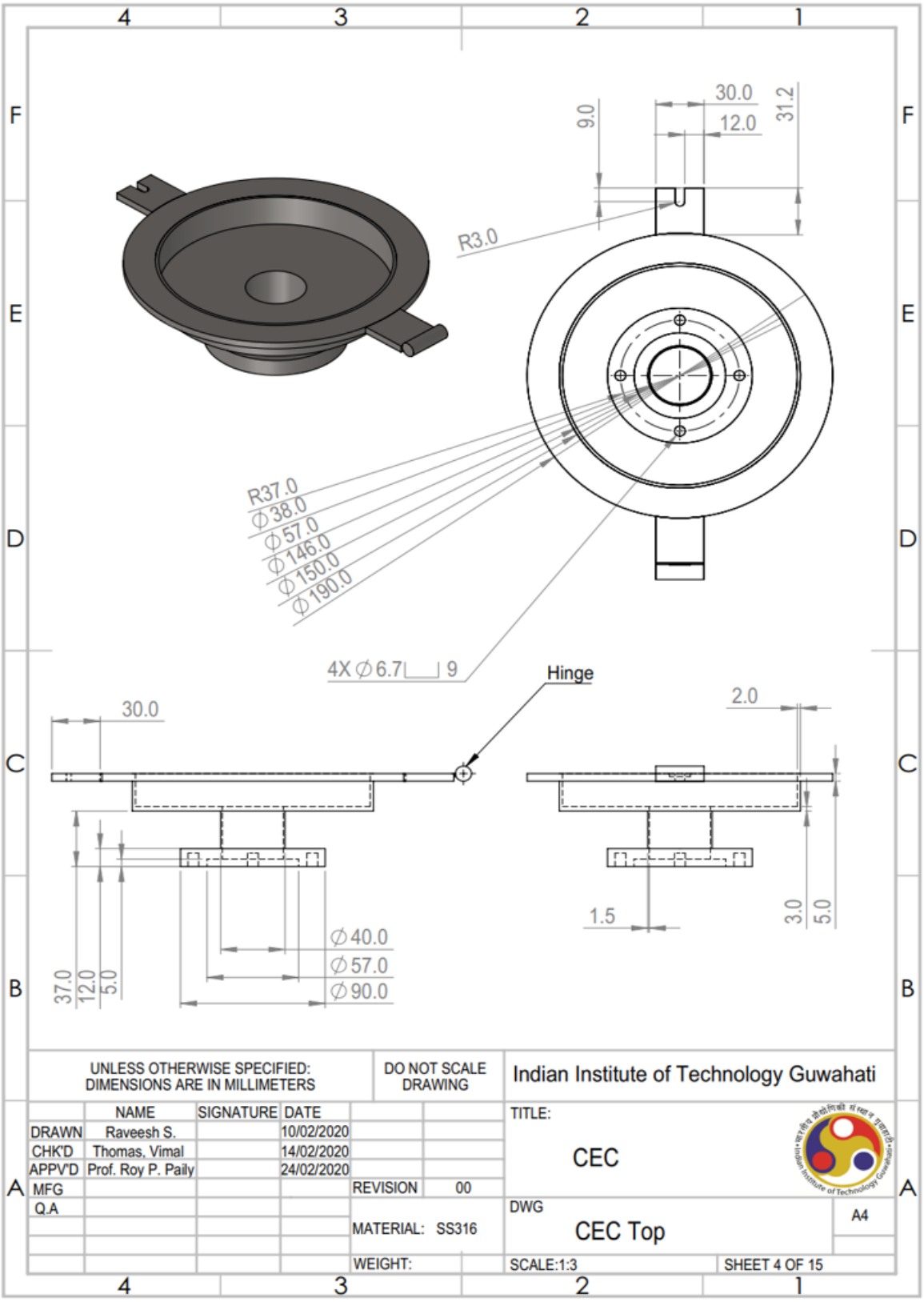

Fig. 3.5: Sensing chamber top part drawing details.

TH-2675_186102019

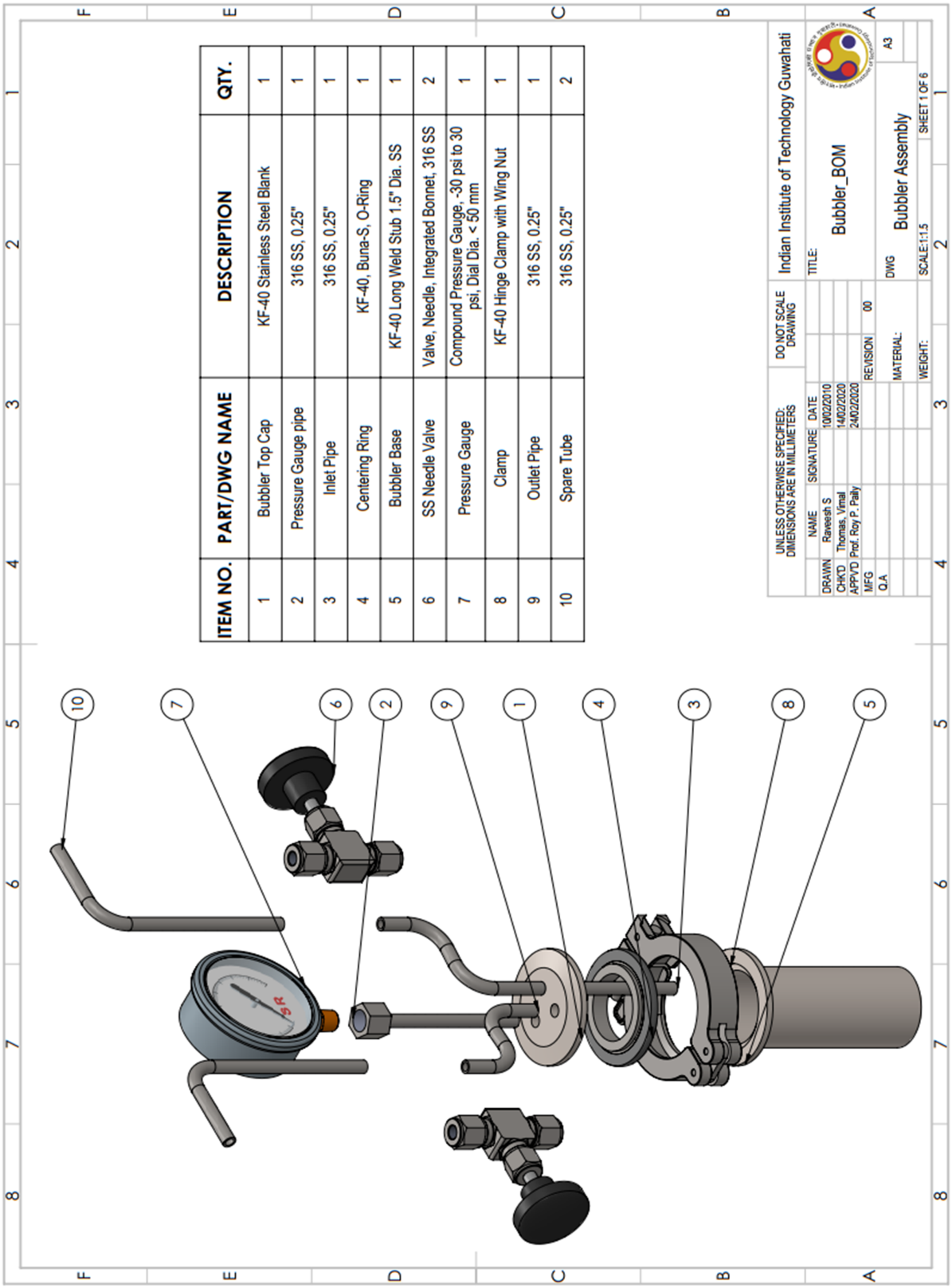

Fig. 3.6: Bubbler parts and assembly drawing.

TH-2675_186102019

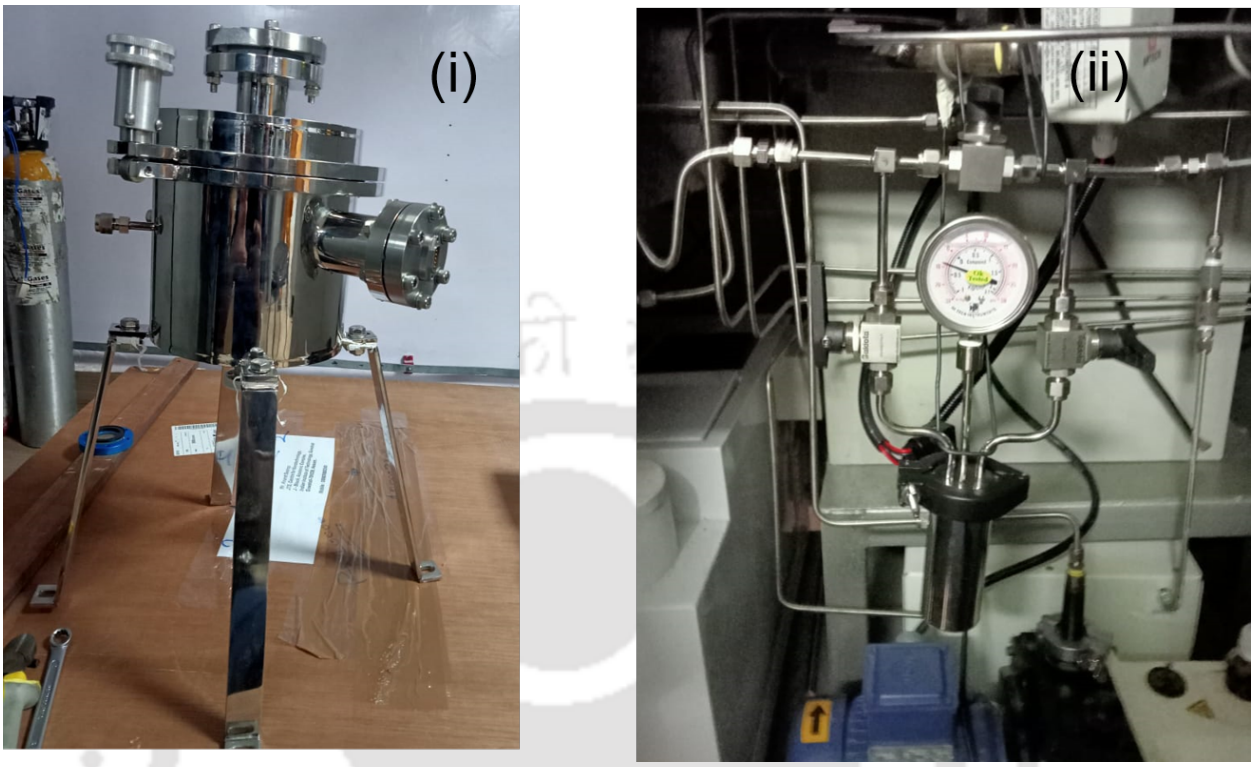

Fig. 3.7: (a) Sensing chamber after fabrication and assembly. (b) Bubbler after fabrication and assembly.

The drawings are sent to Excel Instruments Private Limited, Mumbai, for fabrication. Fig. 3.7(a) shows the sensing chamber after the assembly of chamber parts, and Fig. 3.7(b) shows the bubbler connected with the CEC 2.0. After assembling all the fabricated parts, the system is tested and performed the sensing experiments.

3.3 VOC Sensing System

Although CEC 2.0 has a VOC sensing provision, an exclusive VOC sensing setup is developed due to the following reasons.

(i) CEC 2.0 uses carrier gas for bubbling, which may affect the sensor performance against the atmospheric air measurement [88, 89].

(ii) The pressure maintained inside the chamber during the sensor response measurement may also affect the sensor performance [90, 91].

(iii) CEC 2.0 has MFCs, bubbler, RH generator, and pumps that enhance the system's complexity, cost, and size are not convenient where the application demands portability. Also, CEC 2.0

TH-2675_186102019

ergonomic is built to create a controlled environment using inert gas with desired analyte gas concentrations via pre-mixed analyte gas and carrier gas in compressed cylinders.

(iv) In the case of breath sensors, exhale breath is transferred directly from the respiratory system to the test chamber; this process is not easy to perform using MFCs. Furthermore, lungs can push the air at different flow rates, which may affect the sensor response [92, 93].

A custom-made VOC sensing setup is developed to evaluate the sensor response as shown in Fig. 3.8. The design consists of an airtight borosilicate glass chamber of volume 1.5 L. The chamber is connected with crocodile clips to probe the devices, relative humidity (RH), temperature sensor, heater, white LED, and associated controllers. The chamber has two inlets and one outlet port; one inlet port to take atmosphere air and another to inject the VOCs. The outlet port is connected with a fan that can pump at the rate of 5 SLPM. All the ports are connected with Tygon tubing (PFA, 1/4J), push-type fitting, and valve system. The desired concentration of the VOC in the chamber is achieved by the static liquid gas distribution method [87], which is calculated as

$$C = \frac{22.4 \times \phi \times \rho \times V_1}{M \times V_2} \times 1000 \tag{3.3}$$

where C is the target gas concentration in ppm, ϕ is the required gas volume fraction, ρ is the density of the VOC liquid (gml^{-1}), V_1 is the volume of VOC (μl), V_2 is the volume of the chamber

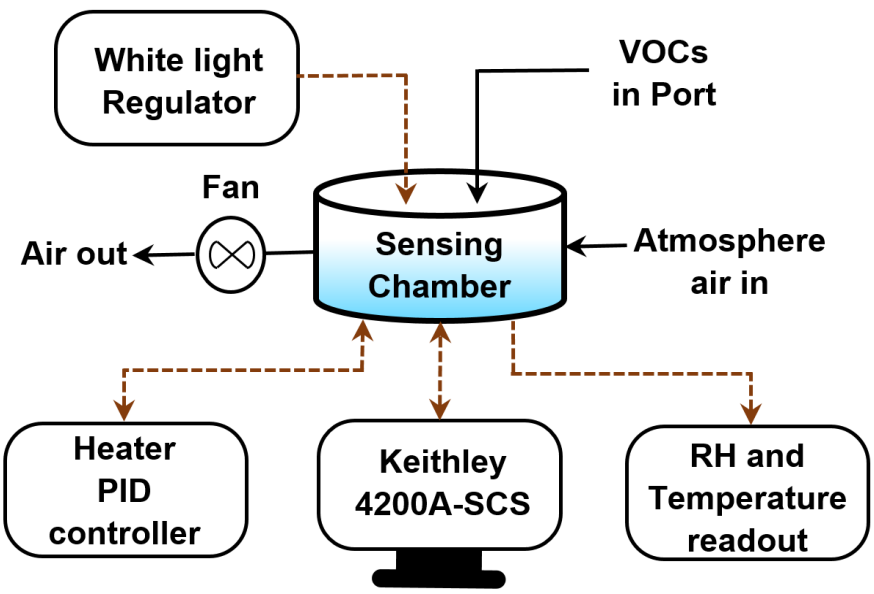

Fig. 3.8: Schematic diagram of VOC sensing system.

TH-2675_186102019

(l), and M is the molecular weight of the VOC ($gmol^{-1}$). VOCs hold high vapour pressure at room or low temperature.

3.4 Summary

This chapter focuses on the design and development of CECs for gas and VOCs sensor measurement. The CEC 2.0 is developed to overcome the shortcomings of the in-house developed setup CEC 1.0. The revised CEC design, fabrication, installation, and testing are done successfully. CEC 2.0 allows sensing of analyte gas with the carrier gas in premixed compressed cylinders; also, VOC sensing can be carried out via 50 ml in-line connected bubbler, via bubbling method. Further, a VOC sensing setup is fabricated to perform the sensor measurements in atmospheric air using the static liquid distribution method for the VOCs.

TH-2675_186102019

TH-2675_186102019

4

CuO Single-Nanowire-Based Devices for VOCs Detection

Contents

TH-2675_186102019

4.1 Introduction

The development of sensors to sense volatile organic compounds (VOCs) is essential in real-time applications. The VOC sensor is used to detect toxic and flammable VOCs in environmental monitoring for human safety, especially indoor air quality; it is also vital in public and workplaces. Guidelines for various VOC concentrations are addressed in terms of permissible exposure limits (PEL). PEL defines the threshold limit of the VOCs that may be present in the air so that the probability of harming human health is less or negligible. The PEL for benzene, ammonia, ethanol, and methanol is one ppm, 50 ppm, 1000 ppm, and 200 ppm, respectively, as per the occupational safety and health administration (OSHA) guidelines [94]. Besides ambient monitoring, VOC detection is crucial in industrial manufacturing plants, such as beverages, agricultural, and pharmaceuticals [95,96]. Further, VOCs also play a prominent role in diagnosis and medication of the diseases. VOCs are released in human bodies due to different metabolic actions. Relation between human health and VOCs are instrumental in diagnosing various diseases like lungs, breasts, colorectal, and prostate cancer from exhaled breath [4].

Analytical techniques, such as gas chromatography-mass spectroscopy (GC-MS), high-performance liquid chromatography (HPLC), electrochemical, and spectrophotometry, have been employed to detect the VOC accurately [97–100]. However, instrumentation associated with these techniques has drawbacks, such as heavy, costly, low throughput, and requires skilled operators, leading to difficulty in real-time monitoring and delay in disease diagnosis. The delay in disease diagnosis results in more transmission and fatalities, fast detection of infectious diseases is the need of the hour. The metal oxide semiconductor-based VOC sensors offer a better choice for sensing

In chapter 2, the CuO SNW device exhibits exceptional performance for white light detection with high reliability; these results drive to use a back-to-back Schottky CuO SNW MSM structure to detect VOCs. In this chapter, CuO SNW devices are fabricated to sense the VOCs such as ethanol, acetone, and 2-propanol, etc. Devices with channel lengths 10, 20, and 30 μm are fabricated using microcantilever contact print (μCCP) of silver nanoparticles (AgNP) on Si-SiO_2 substrate. Sensing is carried at room temperature, 150 °C, and in white light (1 $mWcm^{-2}$) by using an in-house developed VOC sensing setup (chapter 3, section 3.3). The experiment is performed using the static liquid distribution method in open atmosphere. The device exhibits limited response but stable performance for four months.

TH-2675_186102019

4.2 Materials and Methods

CuO NWs are grown using high-purity copper (Cu) wires (99.99%) of 0.5 mm diameter using thermal oxidation [60]. All the chemicals, VOCs, and AgNP ink are procured from Merck, India, and used as received from the supplier. The Nano eNabler system and its surface patterning tools (SPTs) are used to fabricate the devices. Si-substrate with 300 nm SiO_2 oxide layer is used as a substrate; the sensing experiment is performed in a custom-made VOC sensing setup.

4.2.1 Fabrication of CuO NW Devices

The details of CuO NW synthesis and the device fabrication are covered in Chapter 2, Section 2.2. Devices of length 10-30 μm and diameter of 250-300 nm are fabricated by employing the methods mentioned above.

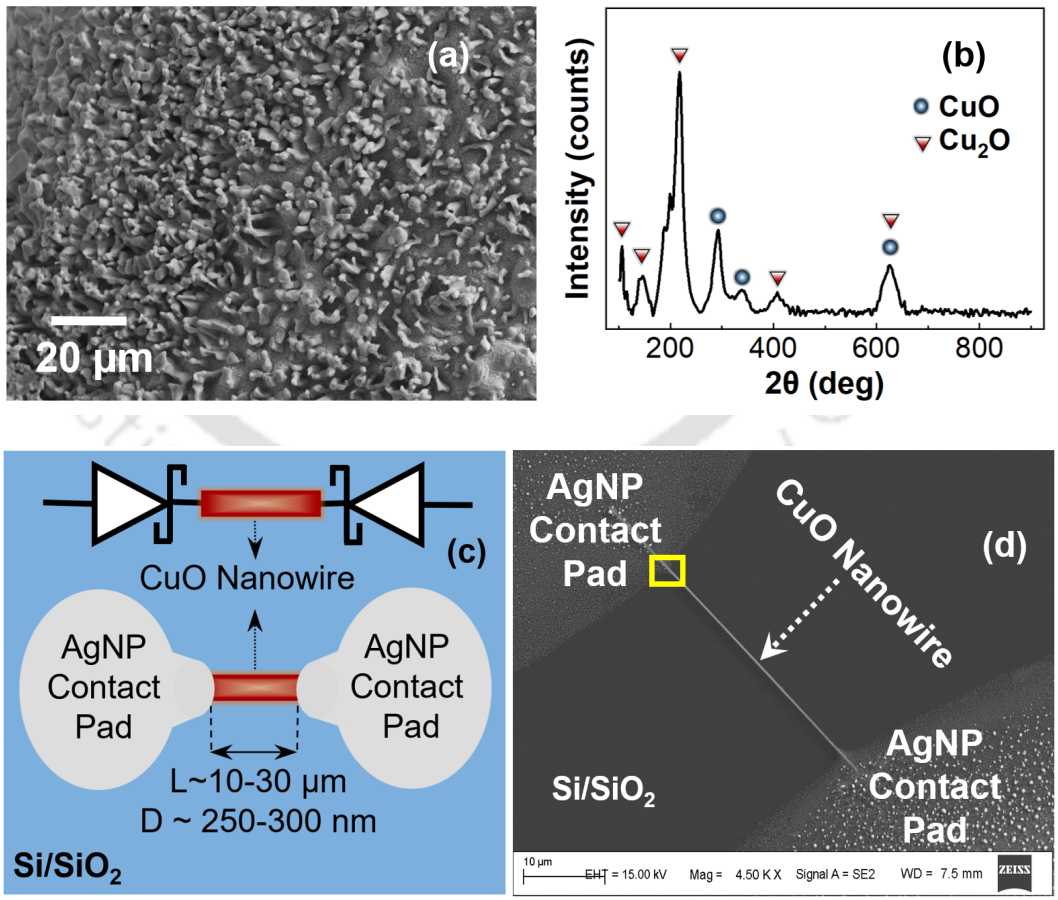

Fig. 4.1: (a) FESEM image of CuO NWs on Cu wire. (b) Raman spectra of thermally oxidized Cu wire. (c) Schematic of the CuO SNW device. (d) FESEM image of CuO SNW device, L: length = 30 μm and D: diameter 250 nm.

TH-2675_186102019

4.3 Results and Discussion

Fig. 4.1(a) shows the FESEM [Make: Zeiss, Model: Sigma] of CuO whiskers (NWs) over the copper substrate. The oxidized Cu wire substrate composition has been studied by Raman scattering [Make: Horiba, Model: LabRam HR Evolution]. The Raman scattering is performed at room temperature using a 532 nm wavelength laser. Fig. 4.1(b) shows the Raman spectra of oxidized Cu wire. Peaks at 109, 148, 216, 414, and 626 cm^{-1} are observed in Cu_2O [101, 102]; also, characteristic peaks at 291, 336, and 626 cm^{-1} belong to CuO [103] NWs. CuO SNW printed device schematic is shown in Fig. 4.1(c). The CuO SNW device of length 30 μm is shown in Fig. 4.1(d). Also, the device with 10 μm length can be found in chapter 2, section 2.3. Fig. 2.4(b) shows the CuO SNW/AgNPs interface FESEM. Fig. 4.2(a) shows the elemental composition of CuO NWs, obtained via energy-dispersive X-ray spectroscopy (EDS). The weight % of CuO NWs have 83.4% and 16.6% Cu and O, respectively.

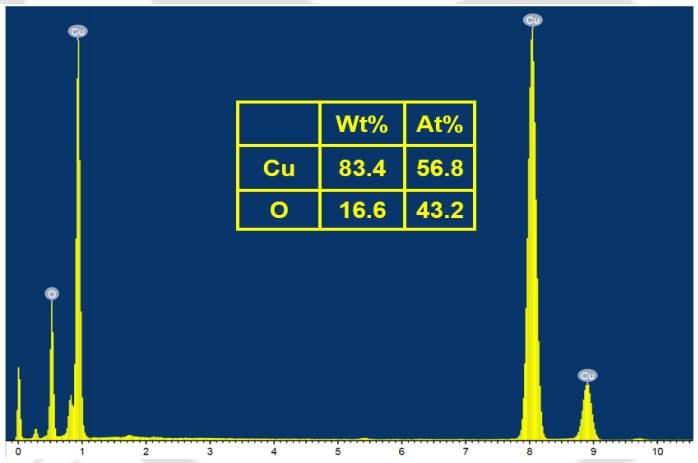

Fig. 4.2: (a) EDS data for CuO NWs.

4.3.1 Sensing Mechanism

VOC sensing strongly involves the CuO NW channel surface adsorption and desorption process, leading to electrical conductivity change. In general, when CuO is exposed to atmospheric air, the surface of CuO NW covers with negatively charged oxygen ions which leads to hole accumulation layer on the surface. The concentration of oxygen ions on the CuO NW depends on the operating temperature, area, and active sites. In p-type semiconductors, adsorption of oxygen species results in trapping electrons from the materials, which leads to increase in the concentration of holes near the NW surface. Whereas, in the reducing gas environment exposure, negatively charged oxygen species at

TH-2675_186102019

surface reduces; in turn, hole concentration decreases [37, 104]. The fabricated devices have Schottky contacts, current transport through the CuO NW dominated by the thermionic-emission [105]. The barrier height plays a vital role as shown in the following equation

$$I_{TE} = AA^*T^2 e^{\frac{-q\phi_B}{kT}}[e^{\frac{qV}{\eta kT}} - 1] \tag{4.1}$$

where, A is the device contact area, A* is the effective Richardson constant, ϕ_B is the barrier height. k is the Boltzmann constant T is the absolute temperature, q is the elementary electric charge, V is applied voltage, and η is the ideality factor. Keeping all other parameters constant, except ϕ_B, current through the device could be modulated to a large extent because of the exponential dependency. When the device is exposed to atmospheric air, holes concentration increases, which reduces the barrier height and results in more current through the device. On the other hand, when it is exposed to VOCs, the hole concentration is reduced, leading to an increase of barrier height; the resultant current in the device reduces.

4.3.2 Electrical Characterization

Parametric analyzer [Make: Keithley, Model:4200A-SCS] and light meter [Make: Gentec-EO, Model: Pronto-Si] are used to perform the electrical characterization and optical measurements, respectively. The device is kept inside the sensing chamber, and a bias voltage of ±10 V with a step size 5 mV has been applied. The device response under dark conditions is shown in Fig. 4.3(a) and (b), the device I-V matches back-to-back Schottky diode behavior. Then device response to various VOCs at room temperature is evaluated by biasing the device at +5 V. The higher voltage is applied to the device, due to anomalous response in the lower voltage ($\leq \pm 3$ V). Prior to sensing, the chamber is evacuated for a minute with fresh air at 5 SLPM to remove contaminants. Then desired concentration of VOC is injected into the chamber, followed by evacuation with atmosphere air. Fig. 4.3(c) shows the transient response of the device for ethanol injection of 25, 50, 75, and 100 ppm concentration and evacuation at regular intervals.

The device response is estimated as follows

$$R = \frac{|I_{voc} - I_{air}|}{I_{air}} \times 100\% \tag{4.2}$$

where I_{voc} is the current after injection of VOC, I_{air} is the current in the presence of atmospheric air,

TH-2675_186102019

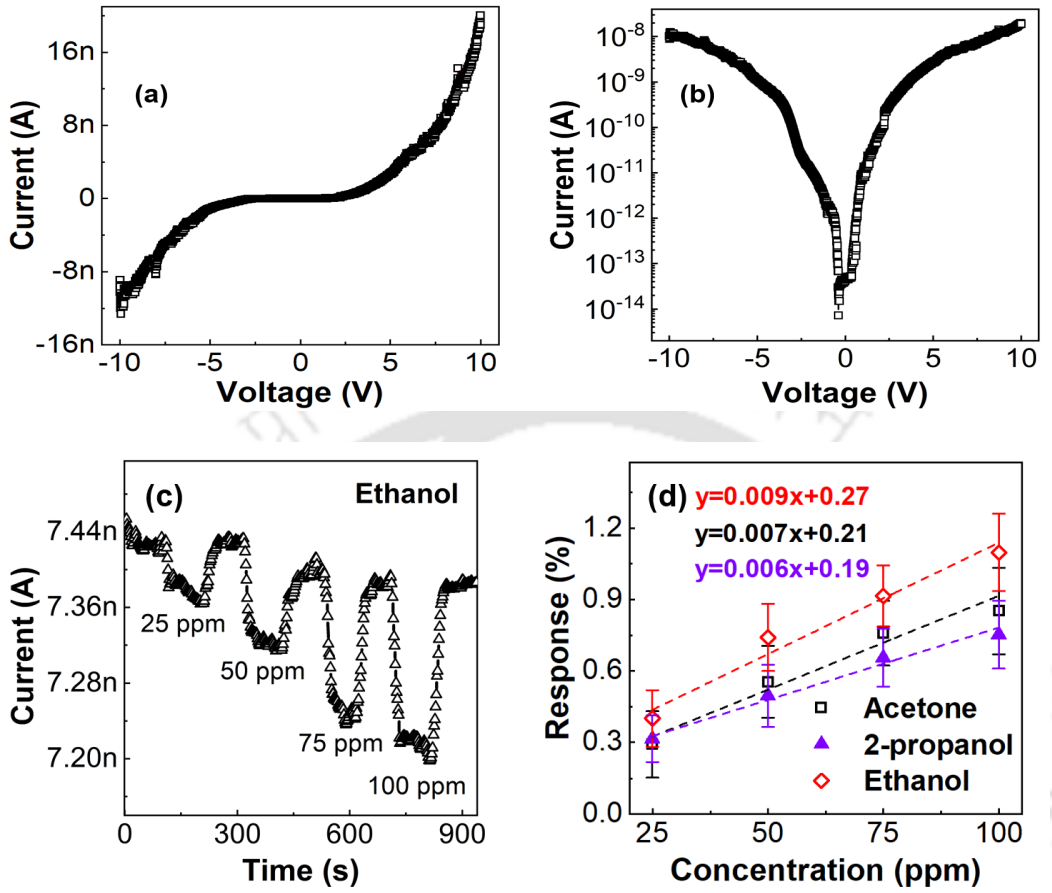

Fig. 4.3: I-V characteristics of the CuO SNW sensor (a) linear scale, (b) log scale. (c) Transient response of the sensor for different concentrations of ethanol at room temperature. (d) Response of the CuO SNW sensor for different concentrations of ethanol, acetone, and 2-propanol.

respectively. The response % for 25, 50, 75, and 100 ppm are 0.40, 0.74, 0.91, and 1.10% respectively. From Fig. 4.3(c), the base current is changed slightly during the recovery, may be due to the incomplete desorption of ethanol from the NW surface. Similarly, acetone and 2-propanol are injected, and the response is recorded. Fig. 4.3(d) shows the response of ethanol, acetone, and 2-propanol. Further, the limit of detection (LOD) is calculated as follows

$$LOD = \frac{3 \times \sigma}{S} \tag{4.3}$$

where, σ represents the standard deviation of the response and S is the sensitivity. LOD of the VOCs is calculated by performing linear regression analysis on the response vs concertation plot. The regression analysis provides standard error of the response and slope of the linear fit (sensitivity). Fig. 4.3(d) shows the linear fit of the ethanol, acetone, and 2-propanol and LOD found to be 20.6, 24.1, and

TH-2675_186102019

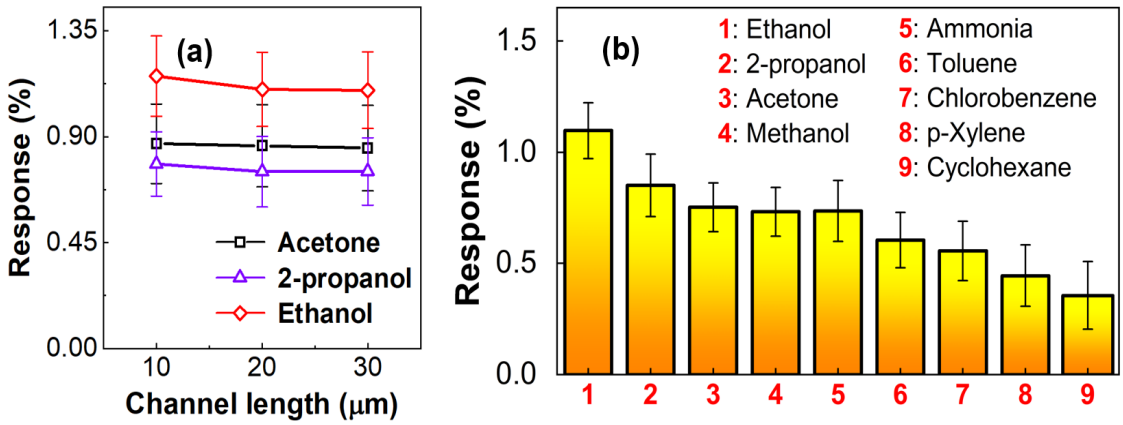

Fig. 4.4: (a) Response of CuO SNW sensor with varying channel lengths. (b) CuO SNW VOCs response at 100 ppm concentration.

15.4 ppm along with sensitivity 0.009, 0.0075, and 0.0059%ppm^{-1} respectively. In addition, devices with length 20 and 10 μm are employed to check the response. Fig. 4.4(a) shows the response of the devices with different channel lengths against the 100 ppm concentration of ethanol, acetone, and 2-propanol. The channel length of the sensor has a negligible effect on the VOC response. Moreover, VOCs such as methanol, ammonia, toluene, chlorobenzene, p-Xylene, and cyclohexane are injected at 100 ppm concentration, and device response is shown in Fig. 4.4(b)

4.3.3 Thermal and Photoactivated Sensing

In general, metal oxides have a better response at high temperature due to increased rate of adsorption and desorption, and change in the bandgap. Fig. 4.5(a) shows the effect of temperature from 25 to 150 °C on the device. As the temperature increases, the current also increases proportionally except at lower temperature up to 50 °C; This can be attributed to the rise of charge carriers at high temperature. For sensing, the temperature is set to 150 °C, and the device is biased at +5V, then desired concentration of VOCs injection and evacuation is carried to record the device response. Fig. 4.5(b) shows the transient response of the device for ethanol injection of 25, 50, 75, and 100 ppm concentration and evacuation. The device exhibits slight improvement in the response. The device response to the injection of ethanol mostly follows the equation

$$I_{Res} = I_{air} + C_0 \times e^{\frac{-t}{t_0}} \tag{4.4}$$

where I_{air} is the current in the presence of atmospheric air, C_0 is arbitrary constant, t_0 is time

TH-2675_186102019

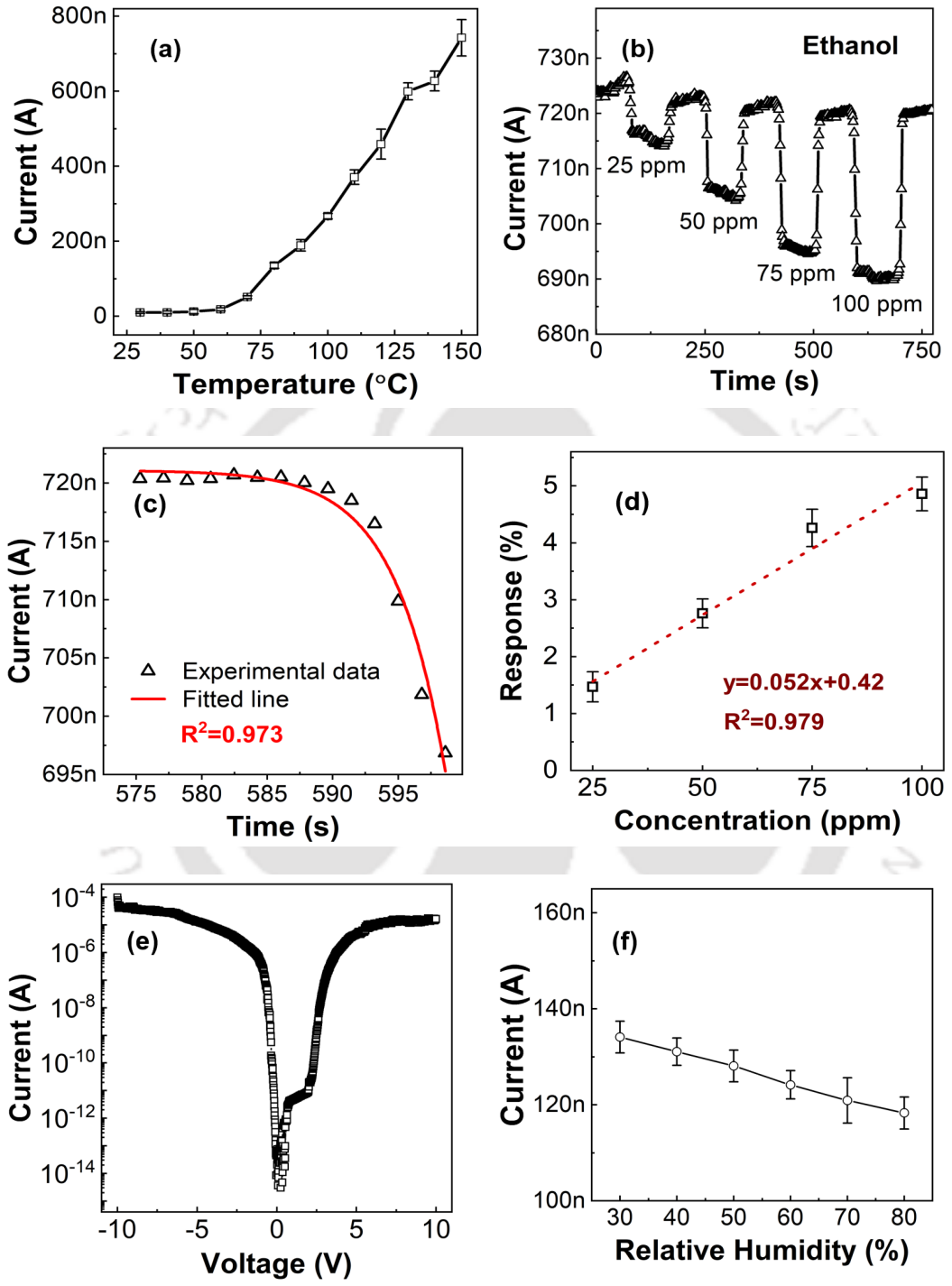

Fig. 4.5: (a) Temperature response of the sensor. (b) Transient response of the sensor for different concentrations of ethanol at 150 °C. (c) Adsorption (fitted line) with experimental data. (d) Response of the device for different concentrations of ethanol. (e) I-V characteristics of the CuO SNW photocurrent. (f) Humidity response of the sensor.

TH-2675_186102019

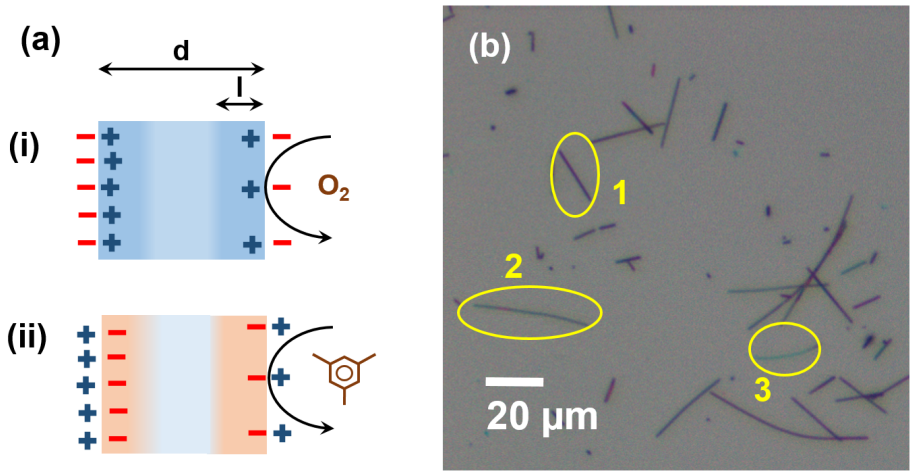

Fig. 4.6: (a) Schematic of CuO NW interaction with (i) Oxygen species and (ii) with VOCs. (b) Optical image of CuO NWs assemblage with various diameters.

constant, and t is time. Fig. 4.5(c) shows the experimental data and the fitted line with R^2 value 0.973. Similarly, recovery also follows the same equation, except time constant with R^2 value 0.982. Device response against various concentrations are plotted as shown in Fig. 4.5(d). Also, the linear fit is performed on data with R^2 value 0.979 results in LOD of 19.2 ppm and sensitivity of 0.052% ppm $^{-1}$.

Further, sensing is performed under the white light, as it exhibits good photoresponse. Fig. 4.5(e) shows the photocurrent with applied bias voltage ±10 V at 5 mV step under the white light 25 mWcm^{-2}. For sensing, white light is set to 1 mWcm^{-2} and biased at +5V. A similar procedure is followed to record the device response to various concentrations of ethanol and other VOCs. The response is at par with the high temperature with negligible deviations. Table 4.1 shows the response of the device for 100 ppm ethanol, acetone, and 2-propanol with CuO SNW sensor under different conditions. Fig. 4.5(f) shows the effect of humidity on the sensor. The current through the sensor decreases with an increase in relative humidity due to the adsorbance of OH^- ions over the surface of NW [106].

Table 4.1: Comparison of CuO SNW device response (%) to VOCs at various operating conditions

VOCs at 100 ppm	**Room temperature**	**At 150 °C**	**White light 1 mWcm^{-2}**
Ethanol	1.1	4.86	4.91
Acetone	0.85	4.14	4.20
2-propanol	0.75	4.24	4.18

TH-2675_186102019

Table 4.2: Comparison of recent CuO based ethanol sensor with our work

CuO Morphology	Concentration ppm	Operating temperature	Response	Response time	Recovery time	Fabrication methodology	Device [Ref.]
Nanowires	100-1000	240 °C	1.5†	30-235 s	60-245 s	Ag painting	Cu-Ag/CuO NWs/Ag-Cu [35]
Nanowires	100	300 °C	1.12 †	NA	NA	Lithography, Sputtering	Cu/Cu_2O-CuO NWs/Cu_2O-Cu [104]
Nanoplates	100	RT	176%	NA	NA	IDE, Doctor blade	Pt/CuO/Pt [36]
Thin film	50-300	225 °C	108-269%	10-32 s	3-5 min	IDE, Sputtering	Au/CuO/Au [107]
Single nanowire	100	RT	202†	195 ms	195 ms	FIB/SEM	Au-Pt/CuO SNW/Pt-Au [26]
Lance-shaped leaflets	100	300 °C	9.1†	9.1 s	127 s	NA	Au/CuO/Au [37]
Nanocubes	300	300 °C	1.51†	NA	NA	Lithography E beam evaporation	Pt/CuO/Pt [108]
Single nanowire	**100**	**RT**	**1.09%,1.02†**	**NA**	**NA**	**Microcantilever contact print (μCCP)**	**AgNP/CuO SNW/AgNP [This work]**
		150 °C	**4.86%, 1.06 †**				
		PA	**4.91%, 1.06†**				

RT: Room temperature, Response% =(I_{voc}-I_{air})/I_{air} × 100% or Response†=(I_{voc}/I_{air}), NA: Not available, PA: Photo activated (white light power =1 mWcm^{-2})

4.3.4 Challenges for Improving the Device Response

Despite the device having a single nanowire with proper contact, the response is not significant under room temperature, at 150 °C, and under white light conditions. Table 4.2 shows the comparison of the response of the device with recent CuO-based sensors. We suggest two reasons for the limited performance of the sensors and methods to improve them:

(i) Sensing is primarily a surface phenomenon, which involves analyte molecules interaction over the nanowire surface. When oxygen species interact with CuO NW, the hole accumulation increases near the surface of NW, which increases the holes in NW, as shown in Fig. 4.6(a)(i); and Fig. 4.6(a)(ii) shows the converse with VOC. The overall conductivity of the NW has significant effect only when the diameter is small, i. e. d≤2l [109, 110] where d is the diameter of the nanowire and l is the length of the depletion layer, which will be few nanometers. In our case, the diameter of the NW is ≈ 200-300 nm; hence the overall charge concentration change in NW is minimal, inturn the Schottky barrier.

(ii) Electrodes are fabricated using μCCP using Nano eNabler, equipped with microscope 1000X magnification, and have 6.5:1 zoom ratio. With this setup, we can observe NWs, as shown in Fig. 4.6(b). The numbering in the image shows the NWs with reducing diameter. NWs with lesser diameter are also available (< 200 nm) but couldn't be visualized optically. Also, the NWs with smaller diameter (spot 3 in Fig. 4.6(b)) have problem in printing the electrode using AgNP ink, as it pierces through the NWs and shorts the device. However, the device response to ethanol at different conditions is well maintained even after four months from the fabrication, as shown in Fig. 4.7(c), which indicates the device has good stability.

TH-2675_186102019

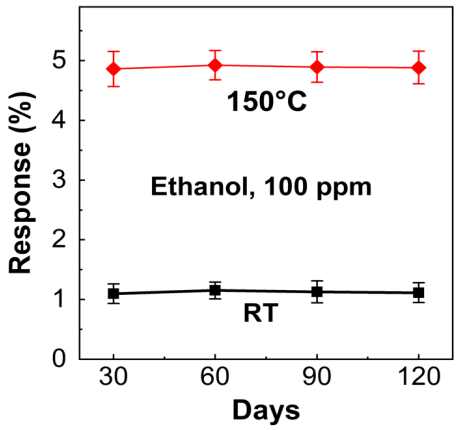

Fig. 4.7: Sensor response to ethanol at room temperature and 150 °C for four months.

4.4 Summary

This work has explored the possibility of realising CuO SNW devices by μCCP for sensing the VOCs. CuO SNW sensor has been fabricated using thermal oxidation and μCCP. The CuO NW sensor response to VOCs such as ethanol, acetone, 2-propanol, etc., at room temperature, 150 °C, and in white light is reported. The sensor has a limited response, and its reasons are analyzed. The performance of the sensor may be improved with different metal nanoparticles ink to fabricate electrodes, which leads to ohmic contact instead of Schottky. Also, NW with a smaller diameter may be used to fabricate the device using distinct imaging techniques to print electrodes.

TH-2675_186102019

TH-2675_186102019

5

CuO SNW FETs and Solution-processed Planar Printed Capacitor and FET

Contents

TH-2675_186102019

5.1 Introduction

FETs are a vital part of the integrated circuits (ICs) known to have very high switching speed; also essential in the design of the command-control-communication system parts. However, FETs are used in sensors with various configurations to sense gases, biomarkers, and VOCs. FET-based sensors are more attractive due to their miniaturized size, low power consumption, and high reliability. The previous chapters 2 and 4 showed CuO SNW as a two-terminal device used for photodetection and VOC sensing. In this chapter, the gate terminal is added in various configurations to realize the FET.

This chapter includes two parts; the first part comprises of CuO SNW FET with back gate, coplanar gate by employing SiO_2 as a gate oxide; the top gate is realized by using aluminum nitrate nonahydrate. The second part comprises fully printed devices metal-insulator-metal (MIM) capacitor and adjacent gate FET by preparing suitable ink for the channel and oxide.

5.2 CuO SNW FET Fabrication

5.2.1 CuO SNW Back Gate FET

The silicon with phosphorous doped (n-type, the resistivity 1-10 Ω-cm at 300 K, <100> orientation) substrate is used for back gate FET fabrication. The SiO_2 thickness is 300 nm with 500 μm thickness. The source and drain terminal is fabricated, similar to section 2.2.2. Further, for the back gate, the native oxide is etched at backside of the substrate using buffered HF (BHF). After etching the oxide layer, AgNP ink has been drop-casted and annealed to act as the gate contact. Since the source and drain have back-to-back Schottky, these FETs are referred to as Schottky barrier FETs (SBFETs). Fig. 5.1(a) shows the schematic of the fabricated back gated SBFET. Optical image of the printed CuO SNW back gate devices (top view) of lengths 30 and 10 μm, respectively, as shown in Fig. 5.1(b-c).

5.2.2 CuO SNW Coplanar Gate FET

The coplanar gate FET is fabricated on Si substrate with 30 nm SiO_2 thickness. The oxide layer is obtained by dry oxidation of Si in the oxidation furnace [Make: Tempress, Model-TS6303]. The source and drain terminal is fabricated similar to section 2.2.2. Further, one more electrode on the same plane is printed to serve as a gate terminal. Fig. 5.2 (a) shows the schematic of the coplanar gate SBFET. Optical image of the printed CuO SNW coplanar gate devices (top view) of lengths 10 and 50 μm, respectively, as shown in Fig. 5.2 (b) and (c).

TH-2675_186102019

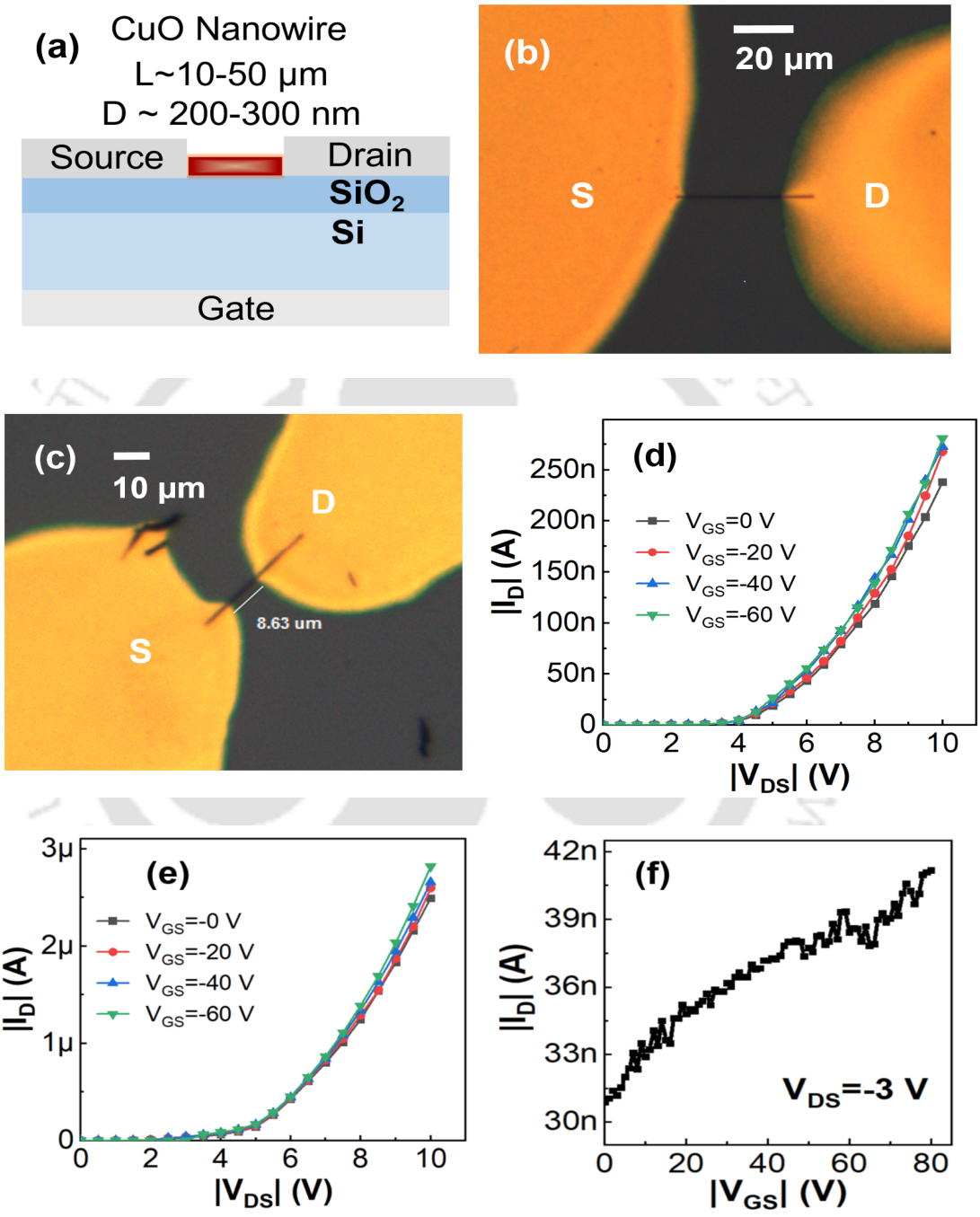

Fig. 5.1: (a) Schematic of the CuO SNW SBFET in back gate configuration (side view). (b) and (c) Optical image of the printed CuO SNW back gate devices of lengths of 30 and 10 μm, respectively (top view). CuO SNW back gate (d) Output characteristics in the dark, (e) Output characteristics in white light 1 mWcm^{-2}. (f) Transfer characteristic in the dark with V_{DS}= -2 V and sweeping the back gate from 0 to -80 V.

TH-2675_186102019

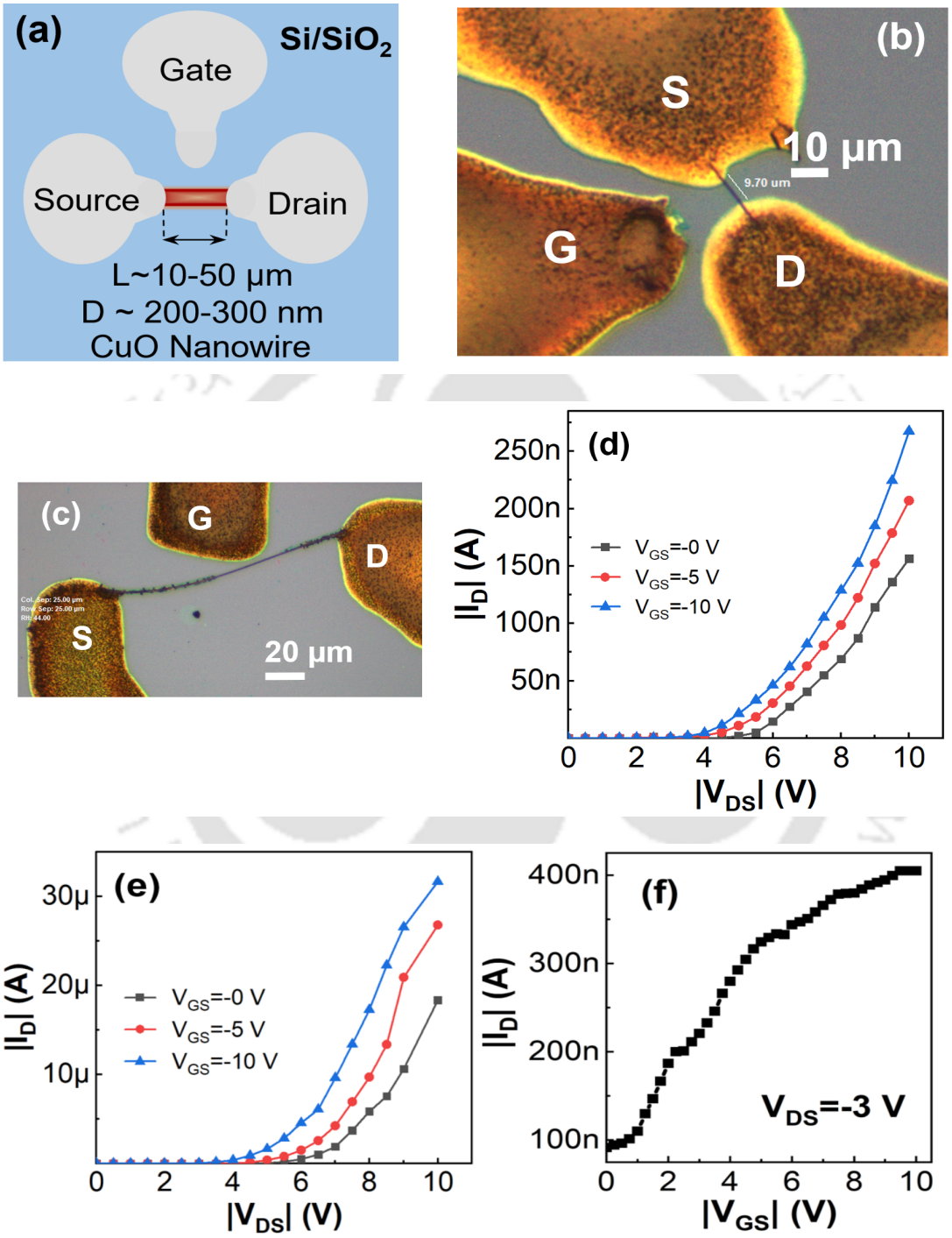

Fig. 5.2: (a) Schematic of the CuO SNW SBFET in coplanar gate configuration (top view). (b) and (c) Optical image of the printed CuO SNW coplanar gate devices of lengths of 10 and 50 μm, respectively (top view). CuO SNW coplanar gate (d) Output characteristics in the dark (e) Output characteristics in white light 1 mWcm^{-2}. (f) Transfer characteristic in the dark with V_{DS}= -3 V and seeping the back gate from 0 to -10 V.

TH-2675_186102019

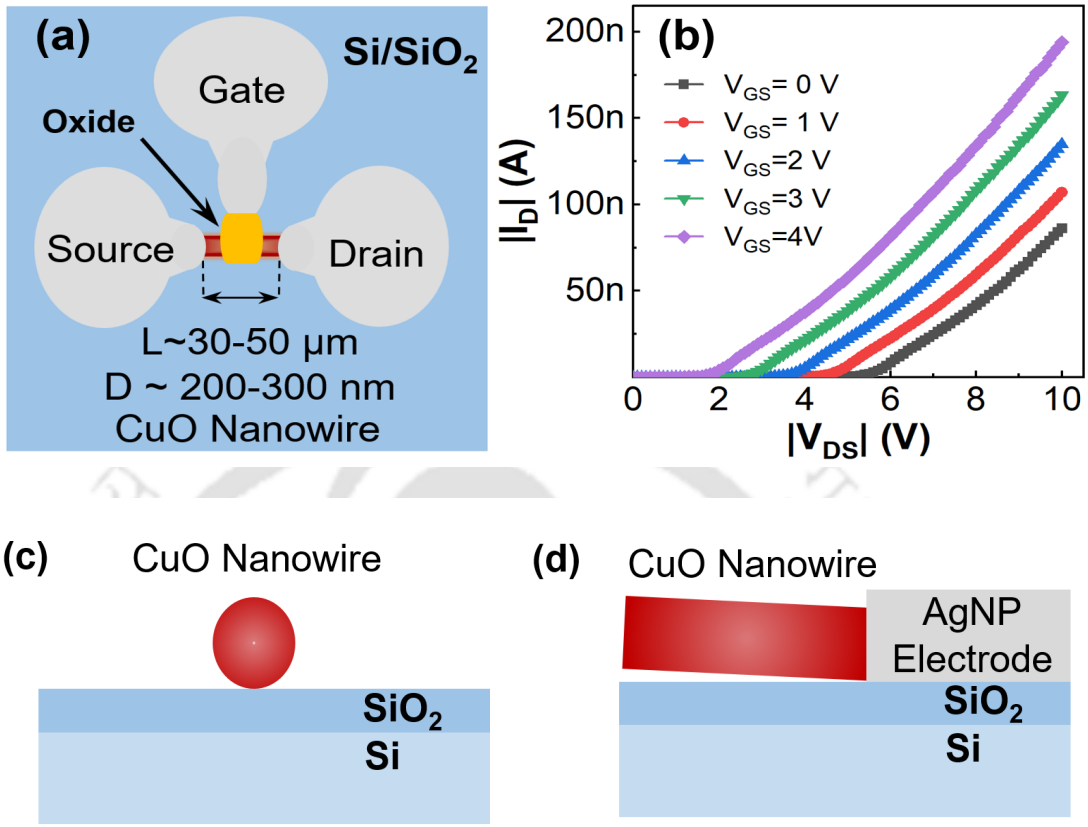

Fig. 5.3: (a) Schematic of the CuO SNW FET in top gate configuration (top view). (b) Output characteristics of the top gate CuO SNW SBFET. (c) Sectional view of the CuO SNW across source and drain. (d) CuO SNW orientation near electrodes.

5.2.3 CuO SNW Planar Top Gate FET

The top gate FET is fabricated on Si substrate with 300 nm SiO_2 thickness. For the device fabrication, a procedure similar to the coplanar gate is followed; then, 0.3 M aluminum nitrate nonahydrate (Product Id:36291) $Al(NO_3)_3 \cdot 9H_2O$ ink is printed over CuO SNW and annealed from 25 °C to 200 °C with a rate of 2 °Cmin^{-1}. Then gradually cooled down to room temperature, followed by AgNP printing over the aluminum oxide to the gate terminal. Fig. 5.3 (a) shows the schematic of the top gate SBFET (top view).

5.2.4 Electrical Characterization

The fabricated devices are electrically characterized with the help of Keithley 4200A-SCS, a parametric analyzer with low-noise cables. Light meter [Make: Gentec-EO, Model: Pronto-Si] is used to perform optical measurements. The device, as shown in Fig. 5.1 (a-c) are fabricated with the back

TH-2675_186102019

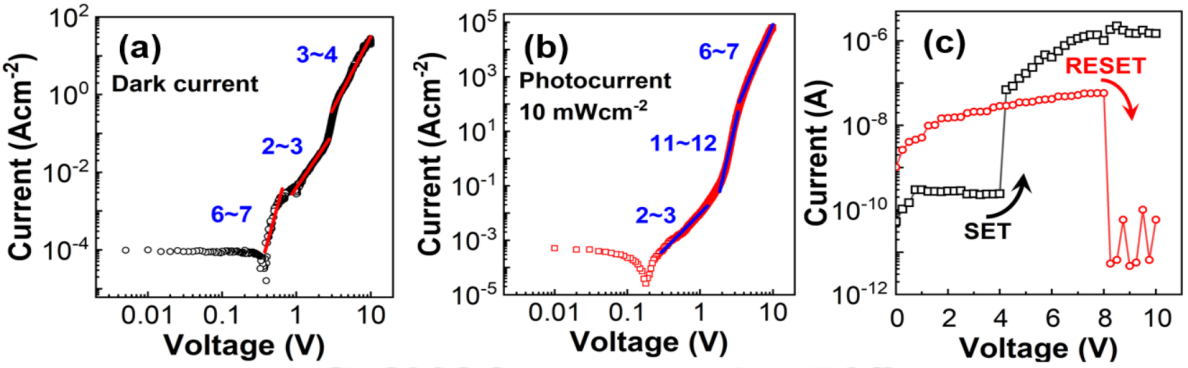

Fig. 5.4: (a) and (b) Current density-voltage (J-V) dark and under white light 1 mWcm^{-2}. (c) Unipolar resistive switching I–V characteristics of CuO SNW devices.

gate configuration. Initially, two-terminal I–V is recorded without applying the gate, typically almost a symmetrical behavior [111, 112]. AgNP/CuO SNW/AgNP structures form a metal-semiconductor-metal (MSM) with two Schottky barriers in series with the resistance of the semiconductors, more often observed in NW devices. It is also reported that thin wires are sensitive to space-charge-limit (SCL) current, characterized with a slope closer to 2 [113,114]. In this direction, to estimate the slope, dark and photocurrent density- voltages (J-V) are plotted as shown Fig. 5.4 (a-b). Slopes vary at different voltages due to tarp states, which may arise due to growth conditions [115, 116]. However, current reduces with increasing voltage at the lower range may attribute the negative differential conductivity (NDC). Also, for the CuO NW device, the intrinsic carrier concentration (n_i) estimation is as follows [113].

$$n_i = \frac{\epsilon_0 \epsilon_{CuO} V_t}{qr^2} \tag{5.1}$$

where ϵ_0 and ϵ_{CuO} are the permittivities of free space and copper oxide, V_t is the transition voltage from NDC to trap mediated SCL conduction, q is the electron charge, and r is the CuO NW radius ($\approx$ 115 nm). The intrinsic carrier densities are found to be in the range of 10^{16}–10^{17} cm^{-3}. The MSM device also exhibits a nonpolar switching behavior with different step sizes and modes of the parametric analyzer, as shown in Fig. 5.4 (c). But, the unipolar switching is not consistent; this current variation may be due to the incomplete formation and rupture of the conductive pathway, at the same polarity [117].

Further, to study the transport properties of CuO SNW, the back-gate voltage is applied. Fig.

TH-2675_186102019

5.1 (d) shows the output characteristics for V_{ds} range 0 to -10 V with V_{gs} voltage 0 to -80 V in dark conditions. Fig. 5.1(e) shows the output characteristics under white light 1 mWcm^{-2}. Further, transfer characteristic is performed in the dark with V_{ds}= -2 V and sweeping the V_{gs} from 0 to -80 V as shown in Fig. 5.1 (f). Similarly, Fig. 5.2 (d-e) shows the coplanar gate output characteristics for V_{ds} range 0 to -10 V with V_{gs} 0 to -10 V in dark and under white light 1 mWcm^{-2}. Fig. 5.2 (f) shows the transfer characteristics under white light 1 mWcm^{-2} with V_{ds}= -3 V and sweeping the V_{gs} from 0 to -10 V. In both back and coplanar gate configurations FETs exhibit weak gate coupling to CuO SNW as reported in the literature [118]. The variation in the transfer characteristics may be attributed to the defect concentration distribution, carrier density, and orientation of the crystal in the NW. The characteristics indicate the normally-on type FETs; negative gate voltage increases the I_{ds}, while a positive voltage reaches the limit, and the current cannot further decrease. This indicates the p-type conduction; the existence of copper vacancies in NW leads to the production of holes [116]. However, in contrast, the CuO NW should be completely depleted of charge carriers at threshold voltage, but NW is not depleted fully or the presence of an additional conduction path. The I_{gs} is significantly less compared to I_{ds}. Transconductance (g_m) of the CuO SNW FET is evaluated as follows

$$g_m = \frac{dI_{ds}}{dV_g} \tag{5.2}$$

For back and coplanar gate configurations g_m is found to be 0.16 nS at -30 V and 0.30 nS at -5V. In addition, CuO SNW hole mobility (μ_h) is estimated using the following equation [50]

$$\mu_h = g_m \frac{ln(\frac{4h}{d})l}{2\pi\epsilon_0\epsilon_{SiO_2}V_{ds}} \tag{5.3}$$

where h, d, and l denote the thickness of gate oxide, CuO NW diameter, and channel length of the device, respectively. ϵ_0 is the permittivity of free space and ϵ_{SiO_2} relative permittivity of silicon dioxide. The hole mobility is estimated to be 0.14 and 0.36 cm^{-2}V^{-1} s^{-1} for CuO SNW back and coplanar gate configurations, respectively. Further, hole concentration (n_h) is calculated as follows

$$n_h = \frac{\sigma}{q\mu_h} \tag{5.4}$$

where σ is the conductivity of the CuO NW. The hole concentration (n_h) in dark and photo-exicitation found to be in the range of 10^{16}–10^{17} cm^{-3} and 10^{17}–10^{19} cm^{-3}, respectively. For FETs, normalized drain current and transconductance are important figures of merit. In NW channel devices, I^*_{ds}=I_{ds}/d

TH-2675_186102019

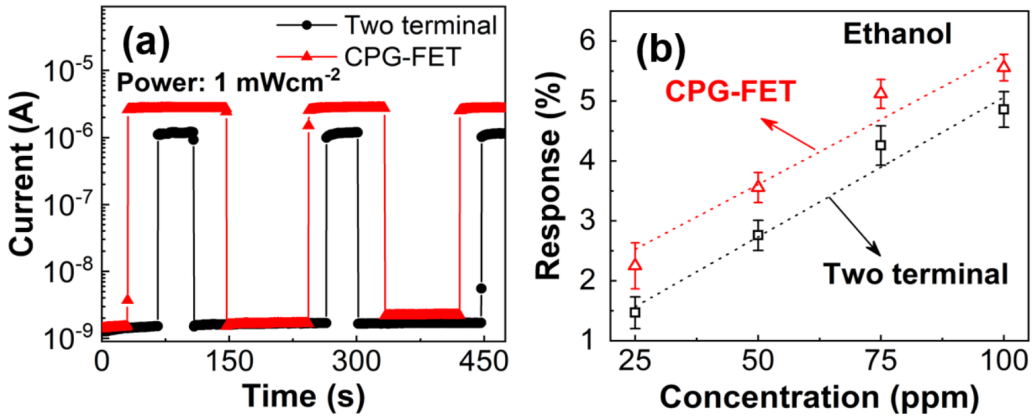

Fig. 5.5: (a) Transient response of two-terminal device, at 5 V, and CPG-FET at V_{ds}= -5V, V_{gs}= -9V with light power 1 mWcm^{-2}. (b) Ethanol sensing response of two-terminal device, -5 V, and CPG-FET at V_{ds}= -5V, V_{gs}= -9V, at 150 °C .

and g_m^*= g_m/d, where d is diameter of the NW (≈ 230nm), and * indicates the normalized value. Table 5.1 shows the comparison of the recently reported CuO NW FETs with our work. The CuO SNW FETs with μCCP exhibit high output current and decent transconductance.

Table 5.1: Comparison of recent CuO NW based FETs with our work

Source/drain contact	Fabrication Methodology	Gate structure	Gate-dielectric	Gate-oxide thickness (nm)	Threshold voltage (V)	I_{ds}/d (A/cm)	g_m/d (μS/cm)	Carrier mobility (cm^{-2}V^{-1} s^{-1})	I_{on}/I_{off}	Ref. Year
Au-Ti/CuO-SNW/Ti-Au	Lithography †	BG	SiO_2	150	NR	NR	NR	NR	950	[117], 2020
Au-Cu/CuO-SNW/Cu-Au	Lithography†	BG	SiO_2	300	-12	3.2 m	43.2	0.134	2	[50], 2014
Ag/CuO-SNW/Ag	Lithography$^{\Psi}$	BG	SiO_2	150	9	NR	NR	NR	NR	[116], 2010
Au-Cr/CuO-SNW/Cr-Au	Lithography$^{\Psi}$	BG	SiO_2	100	NR	NR	250	632 μ	15.5	[119], 2009
AgNP/CuO-SNW/AgNP	**Microcantilever contact print (μCCP)**	**BG**	**SiO_2**	**300**	**20**	**18.2**	**7.2**	**0.14**	**1.8**	**This work**
		CPG	**SiO_2**	**30**	**3**	**18.5**	**13.6**	**0.36**	**5.5**	
		TG	**AlO_x**	**NR**	**NR**	**18.1**	**NR**	**NR**	**NR**	

†e-beam evaporation, $^{\Psi}$thermal evaporation, NR: not reported, BG: back gate, TG: top gate, CPG: coplanar gate

Fig. 5.5 (a) shows the photo-transient response of two-terminal and CPG-FET. Also, Fig. 5.5 (b) shows the ethanol sensing response of two-terminal and CPG-FET at 150 °C. These results indicate that adding a third terminal had a minimal effect on the sensor responses.

5.2.5 Challenges in CuO SNW SBFETs Fabrication

CuO SNW SBFETs with various configurations are explored; But, none of the gate configurations have better control over I_{DS}. The reasons could be attributed as follows:

(i) In the bottom and coplanar gate configuration, the interface between oxide and CuO SNW is minimal, as shown Fig. 5.3(c). That leads to weak gate coupling with CuO SNW; in turn, it affects the drain current (I_{DS}).

TH-2675_186102019

(ii) Fabrication of source and drain electrodes to the CuO SNW are carried out sequentially using μCCP. While printing the electrodes, there may be a chance of CuO NW offset from the SiO_2 surface as shown in Fig. 5.3(d).

(iii) Gate all around the NW increases the gate coupling [120]; this encourages printing oxide ink over the NW, and then AgNP is printed over the oxide layer as a gate. However, the gate oxide has high leakage in the order of μA. Gate leakage could be avoided by higher temperature annealing beyond 200 °C, but the AgNP printed electrodes flay off and lead to difficulty in probing the device.

(iv) μCCP process depends on various parameters like the humidity of the chamber, substrate surface wettability, and viscosity of the printing ink. These parameters, in turn, affect the interface of CuO SNW and SiO_2. In non-favorable conditions, ink pierces through the NW and shorts the devices.

TH-2675_186102019

5.3 Solution Processed Completely Printed Devices

5.3.1 Fabrication of in-plane Capacitor and FET

The in-plane metal insulator metal (MIM) capacitor and adjacent gate FET are fabricated, as shown in Fig. 5.6 on a glass substrate using the μCCP technique, [121], [122] [123]. Oxide of the MIM capacitor is fabricated using 0.3 M aluminum nitrate nonahydrate (Product Id:36291) $Al(NO_3)_3 \cdot 9H_2O$ concentration and AgNP ink (Product Id: 736481) used for the formation of electrodes. The printed features are annealed gently till 200 °C from room temperature. For the FET, 0.1 M sodium molybdate dihydrate (Product Id:331058) $Na_2MoO_4{\cdot}2H_2O$ is printed as a channel, along with the 0.3 M aluminum nitrate nonahydrate as oxide layer; the printed features are annealed. The gap between two electrodes for the MIM capacitor is 3-5 μm and the FET channel length is $\approx$ 5-10 μm, thickness of printed features $\approx$ 300-500 nm. The fabrication of the MIM capacitor and adjacent gate FET structure

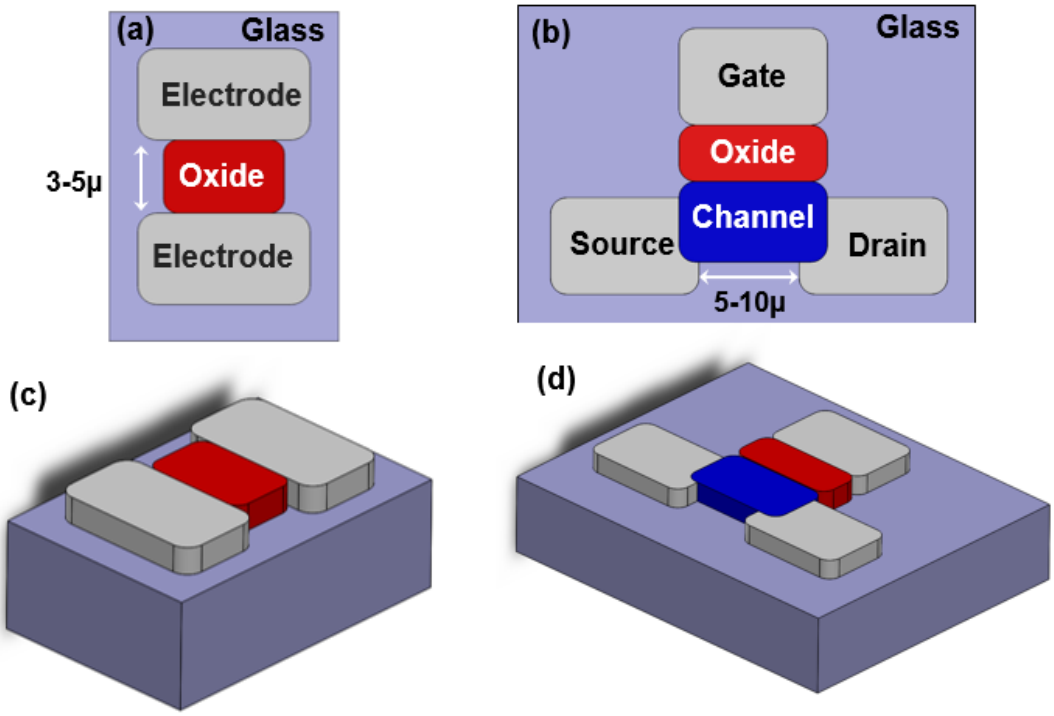

Fig. 5.6: (a) and (b) Top view of the in-plane capacitor and adjacent gate FET, (c) and (d) Isometric view of the in-plane capacitor and adjacent gate FET.

is carried by sequential printing. Fig. 5.7 (a) (i) and (ii) show the flow chart of printing the features of capacitor and FET, respectively. Soon after printing each feature UV treatment is done for 3 minutes, followed by annealing in the atmosphere from 25 °C to 200 °C with a rate of 2 °Cmin^{-1} and then gradually cooled down to room temperature.

TH-2675_186102019

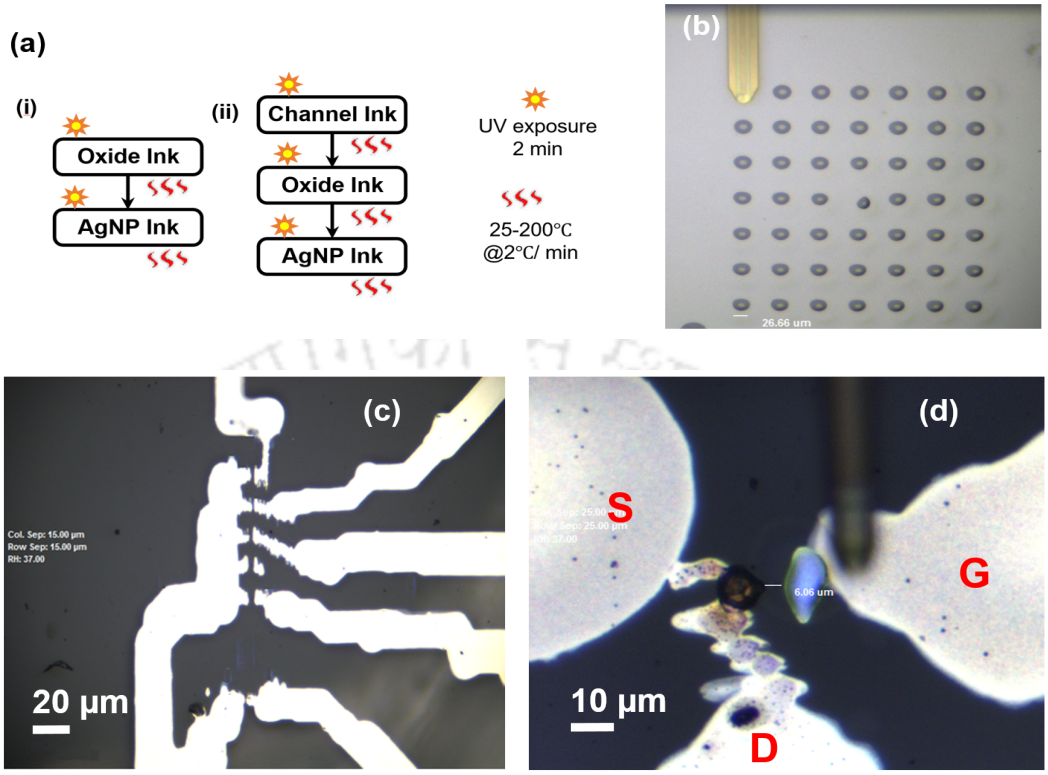

Fig. 5.7: (a) (i) and (ii) Flow chart for printing the features of the capacitor and FET. (b) Printing of microstructures with oxide ink approximate size 20 μm. (c) Optical image of the printed multiple MIM structure with gaps varying from 3 μm - 5 μm. (d) The printed adjacent gate FET, sodium molybdenum oxide ink as a channel, and aluminum oxide ink as gate oxide between the channel and AgNP electrode.

Fig. 5.7(b) shows the printing of microstructures of size 20 μm. Fig. 5.7(c) shows the multiple printed MIM structure with gaps varying from 3 μm - 5 μm. The printed FET is shown in Fig. 5.7(d). The channel sodium molybdenum oxide has $\approx$ 5 μm, and aluminum oxide has a gap of $\approx$5 μm between the channel and AgNP electrode.

5.3.2 Material Characterization

Fig. 5.8(a) shows the XRD [Make: Rigaku, Model: Micromax-007HF] spectra of Na_2MoO_4. The peaks are well-matched with standard JCPDS data 00-012-0773. The Raman scattering is performed at room temperature using a 633 nm wavelength laser. Fig. 5.8(b) shows the Raman spectra of sodium molybdenum oxide. Peaks at 302, 379, 810, and 892 cm^{-1} are observed in Na_2MoO_4 [124]. Fig. 5.8 (c) shows the elemental composition of aluminum oxide, obtained via energy-dispersive X-ray spectroscopy (EDS). The weight % of aluminum oxide has 54.7 % and 45.3 % Al and O, respectively; 33.3 % and 66.7 % in atomic %. Fig. 5.8 (d) elemental composition of Na_2MoO_4 in weight % has 33.3 %, 44.8 %, and 21.9 % Mo, O, and Na, respectively; also, 21.1 %, 66.5 %, and 12.4 % in atomic %.

TH-2675_186102019

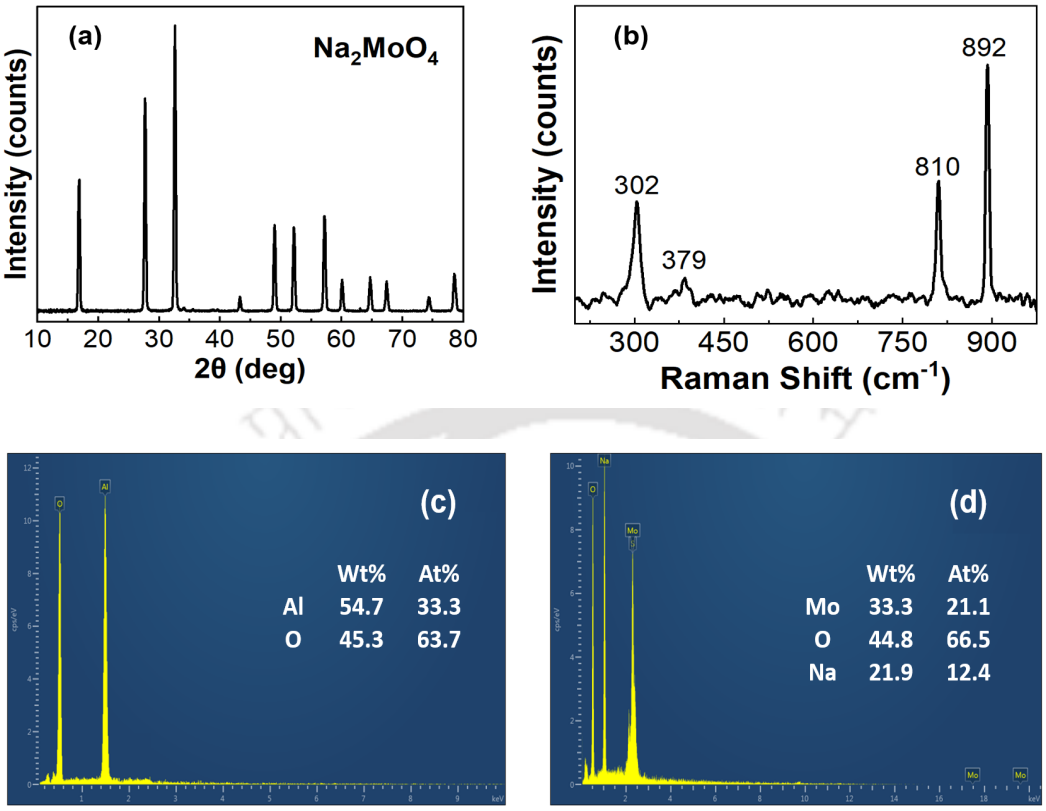

Fig. 5.8: Printed sodium molybdenum oxide (Na_2MoO_4) (a) XRD spectrum, (b) Raman spectra. EDS of (a) Alumiunum oxide, and (b) Na_2MoO_4.

5.3.3 Electrical Characterization

The electrical characterization of the MIM capacitor has been performed with the help of a Keithley 4200A-SCS parametric analyzer and a DC probe station. Fig. 5.9(a) shows the leakage current vs voltage measurements to evaluate the leakage behavior of the in plane MIM capacitor. From the plot, a sample with 150 °C annealing temperature has high leakage compared to the 200 °C, which is likely associated with the defects of incomplete decomposition [125, 126]. The residual nitrate and hydroxyl groups provide a leakage current path, resulting in high leak current. The leakage was found to decrease with increasing annealing temperature, reducing the electronic defects [127].

Fig. 5.9(b) shows the capacitance (C) as a function of frequency (f) for in-plane AlO_x capacitors. The trend between 150 and 200 °C can be attributed to the densification of the metal–oxide complex. Also, an increase in temperature leads to removing nitrates, hydroxides, and absorbed water, reducing the number of mobile charges. The presence of mobile charge species (OH^-) also contributes to the overall polarizability of the material. The devices annealed with above 200 °C provide better results,

TH-2675_186102019

but the printed electrodes start peeling, whereas other materials are sturdy. Printed silver contact pad peeling creates problem for the probing.

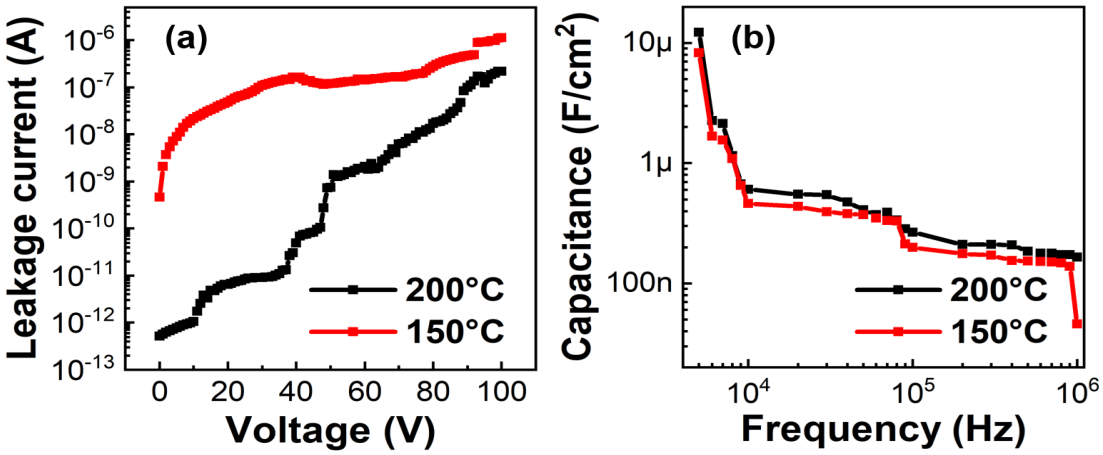

Fig. 5.9: (a) Leakage-current a function of bias voltage. (b) Capacitance a function of frequency.

The following assumptions are made for adjacent gate FET analysis

(i) The channel has homogenous material, charge carriers are readily available without applying the external bias.

(ii) In channel, notable interface and shallow traps are available in the channel due to incomplete decomposition and the densification of the metal–oxide complex.

Fig. 5.10(a) depicts the initial-level behavior of the device FET, and exhibits a high level of noise for the V_{DS} greater than ±2. Fig. 5.10(b) and (c) show the variation of the drain current for the different gate to source voltage. The plots show the back-to-back Schottky-contact with the gate voltage [128], such types of plots described by thermionic emission theory. The diode current is expressed as

$$I = I_o[e^{\frac{qV}{\eta kT}} - 1] \tag{5.5}$$

where, I_o is the diode saturation current, k is the Boltzmann constant T is the absolute temperature (300 K), q is the elementary electric charge, V is the applied voltage, and η is the ideality factor.

$$I_o = AA^*T^2e^{\frac{-q\phi_B}{kT}} \tag{5.6}$$

where, A is the device contact area($2.14\text{x}10^{-7}\text{cm}^{-2}$), A* is the effective Richardson constant (≈ 60.72 A cm^{-2} K^{-2}), ϕ_B is the barrier height.

TH-2675_186102019

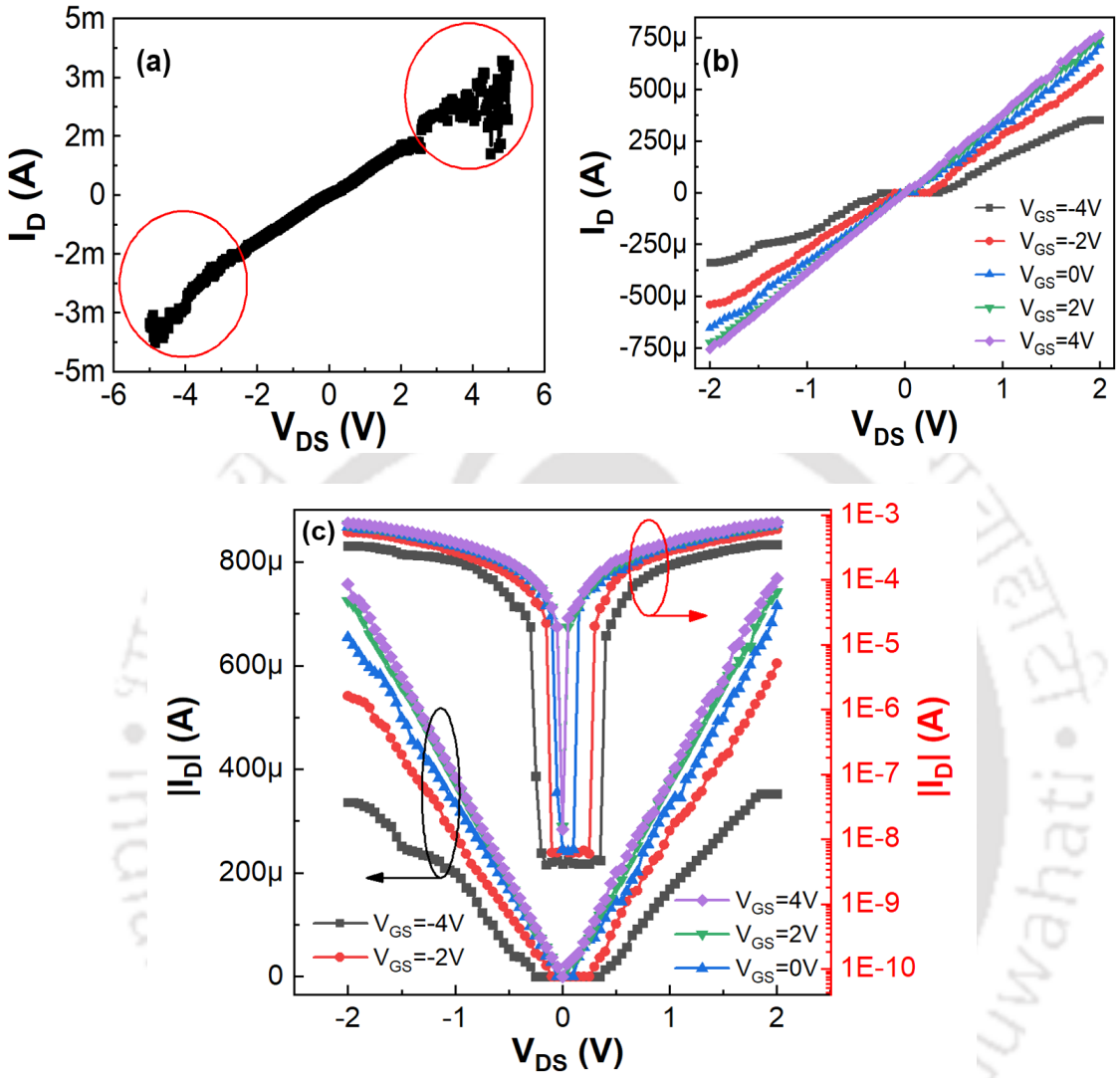

Fig. 5.10: (a) IV characteristics of the channel for the V_{DS}=±5 V. (b) I_D vs V_{DS} FET output characteristics V_{DS} = ±2 V. (c) I_D vs V_{DS} FET output characteristics log scale.

The ideality factor η =2.1 is extracted as the slope of the linear region of ln(I)-V plots for V > 3kT [129] as shown in Fig. 5.11(a). Using the Cheung and Cheung method [130], it is found that, η =2.08 and R_s = 2.83 KΩ series resistance. The difference in η may be due to the presence of, interface states and to the voltage drop across the interfacial layer. Fig. 5.11(b) shows the plot of dV/d(InI) vs. I, the R_s of the devices can be obtained as the slope of a linear portion of dV/dln(I) versus I with ηkT/q as the intercept as follows

$$\frac{dV}{d(\ln I)} = \frac{\eta kT}{q} + I_D R_s \tag{5.7}$$

TH-2675_186102019

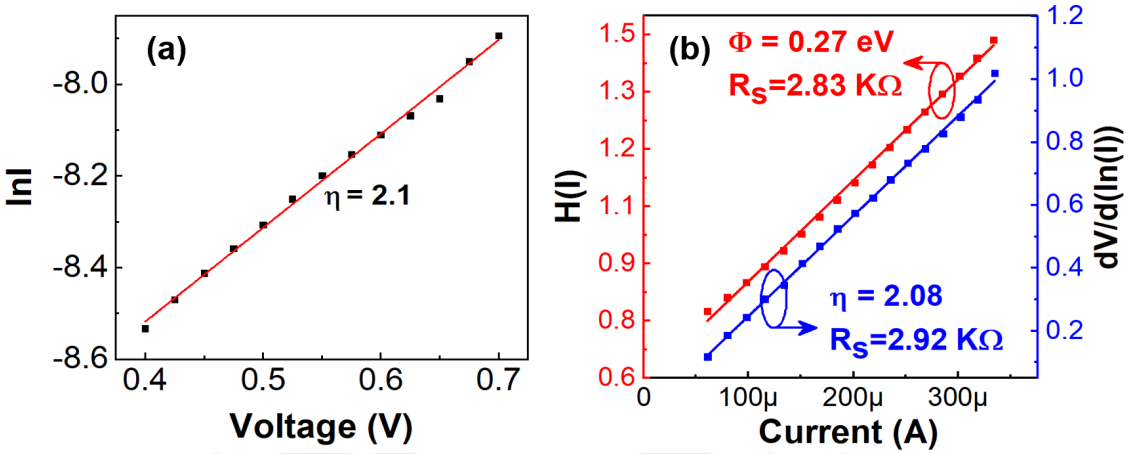

Fig. 5.11: (a) ln(I)-V plot with linear fit to data. (b) dV/dln(I) vs I and H(I) vs I plot with linear fit to data.

η from the above method is used to determine the ϕ_B with the help of the following equation [130, 131]

$$H(I) = V - \frac{\eta kT}{q} \ln \frac{I_D}{AA^*T^2} \tag{5.8}$$

$$H(I) = \eta\phi_B + I_D R_s \tag{5.9}$$

where, $\eta\phi_B$ is the intercept of the linear fit and R_s is the slope of linear fit as shown in Fig. 5.11(b).The values of R_s extracted from H(I)-I plot can be used to verify the same extracted from dV/dln(I)-I plot. Barrier height of the device is calculated as follows:

$$\phi_B = \frac{kT}{q} \ln \frac{AA^*T^2R_s}{V} \tag{5.10}$$

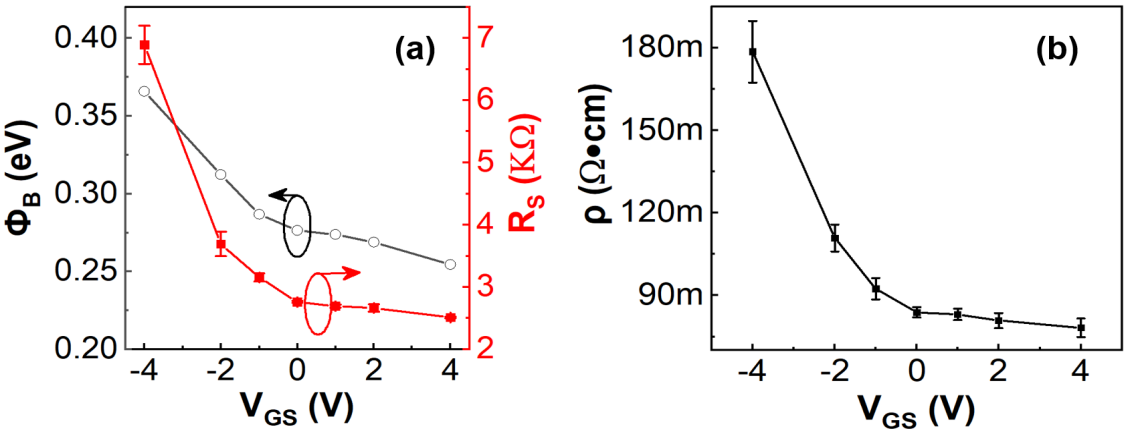

Fig. 5.12: Effect of V_{GS} on (a) Barrier height and series resistance of the adjacent gate FET, (b) Channel resistivity.

TH-2675_186102019

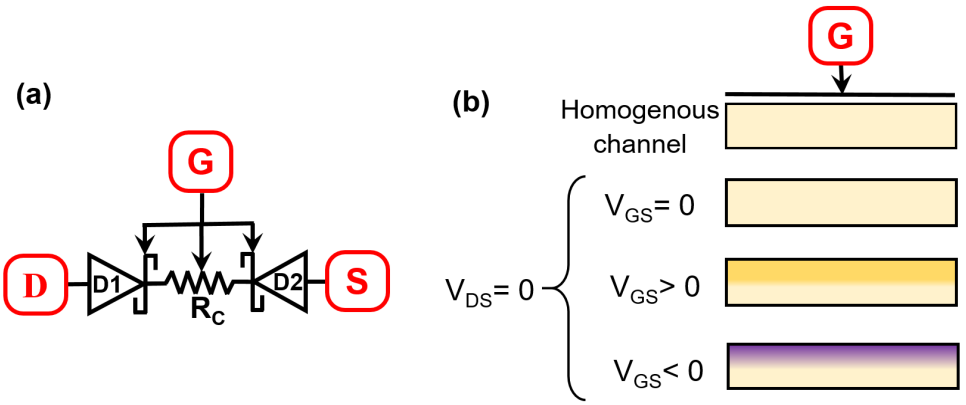

Fig. 5.13: (a) Adjacent gate FET electrical equivalent circuit. (b) Effect of V_{GS} on the channel in the absence of V_{DS}.

Fig. 5.12(a) shows the effect of V_{GS} on barrier height and its series resistance. With zero applied gate to source voltage(V_{GS}=0) device exhibits ϕ_B = 0.27 eV and R_s = 2.83 KΩ. From the plot, with increasing in V_{GS} (+ve), the barrier height is almost unaltered, can be attributed as further no tarps or shallow tarps are not available for the conduction; besides, the series resistance is slightly increased maybe because of the increased carriers scattering. On the other hand, with decreasing in V_{GS} (-ve), barrier height and series resistance increases to ϕ_B =0.41 eV and R_s = 6.2 KΩ, respectively. Similarly, Fig. 5.12(b) shows the effect of V_{GS} on channel resistivity (ρ) varying from 83.8 - 178.5 Ω·cm, for the V_{GS} sweep 0 to -4V, and for the +ve V_{GS} sweep, resistivity slightly decreased. Fig. 5.13(a) shows the approximate equivalent circuit of the adjacent gate FET and Fig. 5.13(b) shows the V_{GS} effect on the channel in the absence of V_{DS}

5.3.4 Challenges in Full Printed MIM Capacitor and Adjacent Gate FET

Solution-processed devices using metal oxide complex inks have limited performance and its reasons are attributed as follows:

(i) Despite minimal gate interface, adjacent gate FET configuration is motivated due to high leakage problem observed in the printed oxide of CuO SNW SBFET with top configuration.

(ii) The annealing temperature after printing each feature is limited to 200 °C; beyond this temperature, AgNP electrodes disintegrate.

TH-2675_186102019

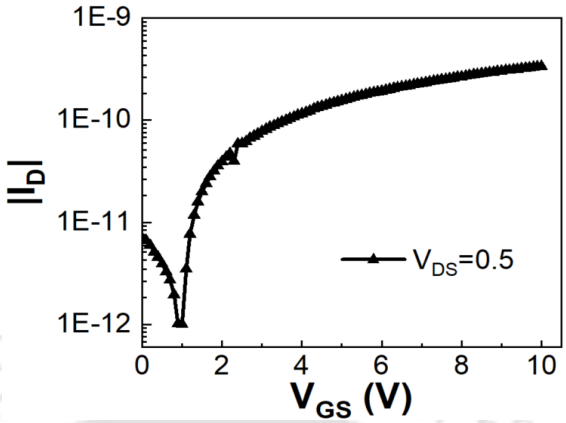

Fig. 5.14: Transfer characteristics (I_D vs V_{GS}) of adjacent gate FET, V_{GS} 0 to 10 V, V_{DS}= 0.5 V.

(iii) Since the annealing temperature is confined to 200 °C, the metal oxide ink decomposition is half-done, which gives rise to the path for the leakage current.

(iv) The configuration adopted in adjacent gate FET has minimal gate interface with the channel, in turn, control over the I_D as shown in Fig. 5.14 for V_{DS} 0.5 V. Further, high V_{DS} take over the control of V_{GS} on I_D.

(v) The printed MIM capacitor and FETs reliability are very poor. The device exhibits proper response for few days only (≈five days); later, the devices are either shorted or have irregular response. This may happen due to the metal oxide complexes' further oxidation in atmospheric air [132].

5.4 Summary

The CuO SNW SBFETs with back, coplanar, and top configuration has been evaluated in dark and white light conditions. Back and coplanar gate structure has less control over I_D due to minimal gate coupling offered by the configurations. The top gate structure is explored to increase the gate coupling with oxide ink results in high gate leakage. Further, printed MIM capacitors and adjacent gate FET are evaluated using oxide and channel ink. The solution-processed FET shows decent performance with $I_{ON}/I_{OFF} > 10^5$, and exhibits poor reliability.

TH-2675_186102019

TH-2675_186102019

6

Conclusions and Future Directions

Contents

TH-2675_186102019

6.1 Conclusion

The fabrication of one-dimensional devices using TMOs to exploit unique electrical properties is in the development stage; this work has contributed to the synthesis and fabrication of the CuO SNW devices using μCCP techniques. Further, two-terminal and FET configurations are explored and employed in applications like photodetection and VOC sensors. As IoT requires small and low-power sensors, NW device architectures are optimum in this regard. NWs use Joule heating in gas sensors with reduced power consumption, which avoids external heaters' requirements. The major contributions and the respective conclusions are as follows:

- The initial work involves developing CuO SNW two-terminal devices using thermal oxidation and μCCP techniques.
  - CuO NWs synthesis is carried using thermal oxidation of Cu wires at temperature 640 °C for 12 h in an open atmosphere using a muffle furnace. The synthesized CuO NWs are characterized using SEM, XRD, TEM, Raman, and UV to understand the material composition and morphology.
  - The synthesized CuO NWs are then transferred to Si/SiO_2 substrate by mechanical scarpe to fabricate single nanowire devices. The electrodes are then printed over a well-separated NW on the Si-substrate using AgNP ink in a sequence. μCCP is carried out using surface patterning tools by employing spot overwrite and drag printing techniques.
- The fabricated two-terminal CuO SNW MSM structure is explored for photodetection.
  - CuO SNW device IV characterization in dark and white light exhibits back-to-back Schtoky behavior. The device exhibits exceptional high sensitivity, responsivity, detectivity, and EQE. Moreover, the detector also reports fast response and recovery, 40 ms and 22 ms, respectively.
  - Exhaustive material and electrical characterization have been carried out to analyze the irregular response of CuO SNW devices at low bias voltage.
- The sensing chamber strongly affects the sensor performance parameters such as response, sensitivity, response time, and recovery time. The design and development of CECs for sensing the gases and VOCs sensor are explored.

TH-2675_186102019

- CEC 2.0 is designed to overcome the shortcomings of homemade CEC 1.0; fabrication and installation are done. The plumbing work uses SS 316 $\frac{1}{4}$ inch tube with compression fittings to handle the carrier and analyte gases in compressed cylinders. CEC 2.0 can carry out sensing at room temperature and also at elevated temperatures up to 400 °C. Further, sensor measurement can be carried out at different pressure.
- An exclusive VOC sensing setup is developed to avoid the carrier gas and the pressure effect; it also increases the portability compared to CEC 2.0. The sensor measurement is carried in atmospheric air, which is essential for validating the breathing sensors.

- Motivated by the CuO SNW photodetection performance, CuO SNW devices are explored for VOC sensing.
  - CuO SNW devices of channel length 10-30 μm are used to detect the VOC, such as ethanol, acetone, 2-propanol, etc., of 100 ppm at various operating conditions.
  - CuO SNW device exhibits response of 1.1%, 4.86 %, and 4.91 % for 100 ppm ethanol at room temperature, 150 °C, and in white light. Device channel length has a negligible effect, and reasons for the limited response are examined.
- In the last phase, the gate terminal is explored in various configurations to realize CuO SNW FET. With the advent of the μCCP technique, the full solution-processed MIM capacitor and the adjacent gate are explored with oxide and channel inks.
  - CuO SNW Schottky barrier field-effect transistors (SBFETs) have been fabricated by printing the source, drain, and gate with AgNP ink. The back, coplanar, and top gate configurations are explored. The gate has less effect on the devices, and its reasons are examined.
  - Fully printed MIM capacitor and adjacent gate FET are explored; the oxide and channel inks are prepared with aluminum nitrate nonahydrate and sodium molybdate dihydrate, respectively. The printed devices exhibit reasonable performance.

Table 6.1 shows the Complete summary of each chapter, including fabrication of devices, applications, and results; also Fig. 6.2 shows the schematic of the overall work.

TH-2675_186102019

6.2 Future Directions

This work mainly emphasizes on synthesis and fabrication of one-dimensional devices using μCCP along with an instrumentation setup for measuring the sensors. Some of the future research scopes are inspired by the challenges faced while exploring the devices and setup.

- **Development of metal nanoparticles ink for electrodes:** Thesis focuses on the development of two-terminal and FET devices using AgNP ink by employing μCCP techniques. After proper annealing, the device structure AgNP/CuO-SNW/AgNP exhibits the Schottky barrier at the interface AgNP/CuO-SNW. Furthermore, AgNP/ZnO-SNW/AgNP also exhibits back-to-back Schottky behavior. However, metals such as copper, indium tin oxide, and gold nanoparticles ink could be examined as shown in Fig. 6.1(a) and (b) for the electrodes. The metal nanoparticles may establish ohmic contact depending on the size and structure. This may change the device behavior significantly and can be used for various applications.

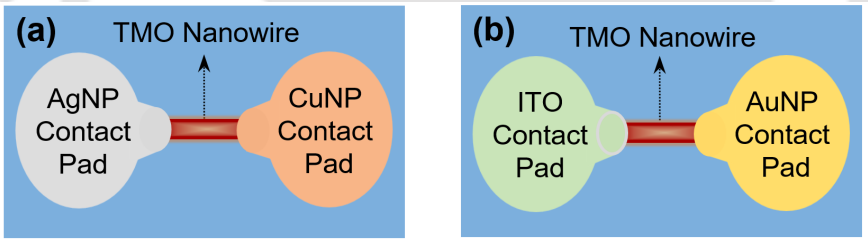

Fig. 6.1: (a) and (b) TMO NW with different metal nanoparticles for Schottky/Ohmic interface.

- **CEC instrumentation:** The CEC 2.0 has the capability of sensing the gases and VOCs. The whole plumbing setup uses compression fittings with manually operated valves to control gas flow during the sensing. Instead, automated valves may be used to direct the gas flow using pneumatics, which will further help to characterize the sensor response more accurately.

- **One dimensional devices:** The CuO SNW devices exhibit good stability and reliability in photodetection and VOC sensing. With recent remarkable developments in machine learning and neural networks, 1D sensor response may be predicted accurately by developing algorithms for more accurate sensing of different VOCs and gases with variable concentrations [133, 134]. Furthermore, μCCP can be scaled to fabricate logic gates, memristors, and circuits that have dimensions in the micrometer size.

TH-2675_186102019

TH-2675_186102019

Table 6.1: Complete summary of each chapter, including fabrication of devices, applications, and results

Chapter	Fabricated devices/ structures details	Application	Results
2: Fabrication of CuO Single-Nanowire Based White-Light Photodetector	AgNP/ CuO-SNW/AgNP Device length ≈ 10 μ m	White light detection 500 nWcm^{-2} to 16 mWcm^{-2}	Photosensitivity (S) =1820 Responsivity (R) = 4085 AW^{-1} Detectivity (D) = 3.81×10^{13}cmHz$^{0.5}$ W^{-1} EQE (η) = 7.23×10^{5} % to 1.27 ×10^{6} Rise (t$_r$) time = 40 ms Fall (t$_f$) time =22 ms\item Power-law: exponent(θ) = 0.81
3: Controlled Environment Chamber design and development for the gas and VOC sensor	CEC 2.0 Plumbing: SS 316 ($\frac{1}{4}$ "), compression fitting, and valves System operation: Manual	Gas and VOCs sensing	Volume ≈ 1.5 L Temperature: Room temperature to 400 °C Analyte and carrier gases: compressed cylinders Bubbler: 50 ml Pressure: Variable
	VOC sensing setup Plumbing: Tygon tubing (PFA, $\frac{1}{4}$ "), push-type fitting, and valves System operation: Manual	VOCs sensing and breath sensor	Volume ≈ 1.5 L Temperature: Room temperature to 150 °C Analyte gas: Static liquid distribution method Pressure: One ATM
4: CuO Single-Nanowire-Based Devices for VOCs Detection	AgNP/ CuO-SNW/AgNP Device length ≈ 10, 20, and 30 μ m	VOCs sensing ethanol, acetone, and 2-propanol, etc.	Ethanol 100 ppm Room tempreture Response = 1.10 %, LOD = 20.6 ppm At 150 °C Response = 4.86 %, LOD = 19.2 ppm White light 1 mWcm^{-2} Response = 4.91 %, LOD = 19.1 ppm
5: CuO SNW FETs and solution-processed planar printed capacitor and FET	CuO SNW SBFETs Channel length ≈ 10-50 μ m Backgate Coplanar gate Top/adjacent gate	Photodetection and VOC sensor	μ_h=0.14 – 0.36 cm^{-2}V^{-1} s^{-1} I$_{on}$/I$_{off}$ = 5.5 n_i=10^{16}–10^{17} cm^{-3} Gate voltage has less effect on I$_d$
	MIM capacitor Length ≈ 3-5 μ m Adjacent gate FET Channel length ≈ 5-10 μ m	VOC sensor	I$_{on}$/I$_{off}$ = 10^3 ϕ_B =0.22 - 0.41 eV R_s = 1.8 -6.9 KΩ Gate voltage has moderate control over I$_d$

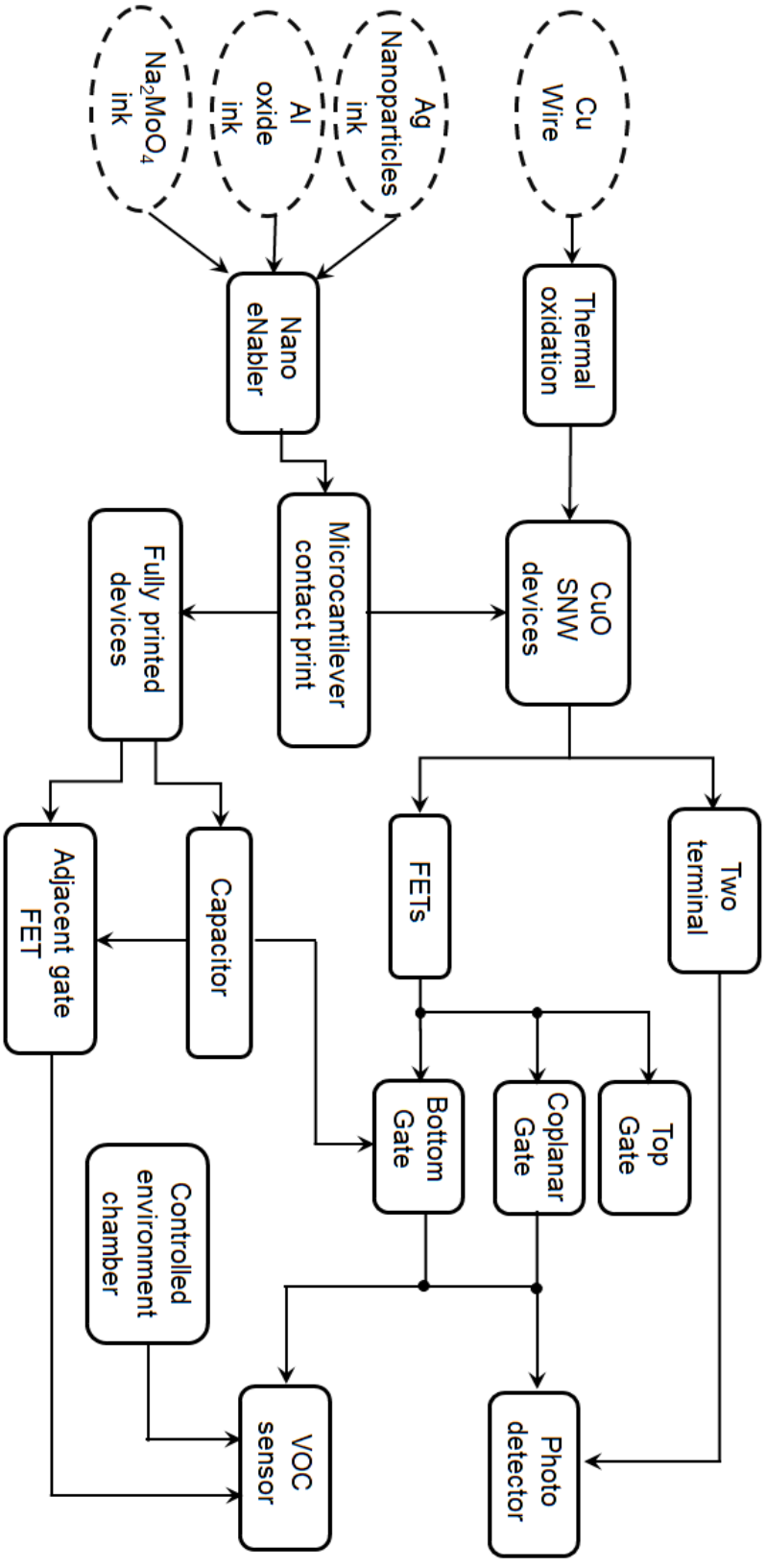

Fig. 6.2: Schematic of the overall work.

TH-2675_186102019

Bibliography

[1] L. A. Thibodeau, R. Reed, Y. Bishop, and L. Kammerman, "Air pollution and human health: a review and reanalysis." *Environmental Health Perspectives*, vol. 34, pp. 165–183, Feb. 1980.

[2] S. H. Cho, J. M. Suh, T. H. Eom, T. Kim, and H. W. Jang, "Colorimetric sensors for toxic and hazardous gas detection: A review," *Electronic Materials Letters*, vol. 17, no. 1, pp. 1–17, Jan. 2021.

[3] G. Korotcenkov, "Handbook of gas sensor materials," *Conventional approaches*, vol. 1, 2013.

[4] G. Peng, M. Hakim, Y. Broza, S. Billan, R. Abdah-Bortnyak, A. Kuten, U. Tisch, and H. Haick, "Detection of lung, breast, colorectal, and prostate cancers from exhaled breath using a single array of nanosensors," *British journal of cancer*, vol. 103, no. 4, pp. 542–551, Aug. 2010.

[5] T. Saidi, O. Zaim, M. Moufid, N. El Bari, R. Ionescu, and B. Bouchikhi, "Exhaled breath analysis using electronic nose and gas chromatography–mass spectrometry for non-invasive diagnosis of chronic kidney disease, diabetes mellitus and healthy subjects," *Sensors and actuators B: chemical*, vol. 257, pp. 178–188, Mar. 2018.

[6] C. Wang, P. Li, A. Lian, B. Sun, X. Wang, L. Guo, C. Chi, S. Liu, W. Zhao, S. Luo *et al.*, "Blood volatile compounds as biomarkers for colorectal cancer," *Cancer biology & therapy*, vol. 15, no. 2, pp. 200–206, Feb. 2014.

[7] S. Li, M. Cheng, G. Liu, L. Zhao, B. Zhang, Y. Gao, H. Lu, H. Wang, J. Zhao, F. Liu *et al.*, "High-response and low-temperature nitrogen dioxide gas sensor based on gold-loaded mesoporous indium trioxide," *Journal of colloid and interface science*, vol. 524, pp. 368–378, Aug. 2018.

[8] K. Kaviyarasu, G. T. Mola, S. O. Oseni, K. Kanimozhi, C. M. Magdalane, J. Kennedy, and M. Maaza, "Zno doped single wall carbon nanotube as an active medium for gas sensor and solar absorber," *Journal of Materials Science: Materials in Electronics*, vol. 30, no. 1, pp. 147–158, Jan. 2019.

[9] W. Maziarz and T. Pisarkiewicz, "Gas sensors in a dynamic operation mode," *Measurement Science and Technology*, vol. 19, no. 5, p. 055205, Apr. 2008.

[10] G. Bailly, A. Harrabi, J. Rossignol, D. Stuerga, and P. Pribetich, "Microwave gas sensing with a microstrip interdigital capacitor: Detection of NH_3 with TiO_2 nanoparticles," *Sensors and Actuators B: Chemical*, vol. 236, pp. 554–564, Nov. 2016.

[11] C. G. García, D. Meana-Llorián, J. M. C. Lovelle *et al.*, "A review about smart objects, sensors, and actuators." *International Journal of Interactive Multimedia & Artificial Intelligence*, vol. 4, no. 3, 2017.

[12] S. Moyer, "IoT Sensors and Actuators," *IEEE Internet of Things Magazine*, vol. 2, no. 3, pp. 10–10, Sep. 2019.

[13] X. Liu, K. Lam, K. Zhu, C. Zheng, X. Li, Y. Du, C. Liu, and P. W. Pong, "Overview of spintronic sensors with internet of things for smart living," *IEEE Transactions on Magnetics*, vol. 55, no. 11, pp. 1–22, Aug. 2019.

[14] A. Kumar and A. Bag, "Ultra-high responsivity (> 12.34 kA W^{-1}) of Ga-In bimetallic oxide nanowires based deep-UV photodetector," *Nanotechnology*, vol. 31, no. 30, p. 304001, May 2020.

[15] C. Zhou, S. Zhang, Z. Lv, Z. Ma, C. Yu, Z. Feng, and M. Chan, "Self-driven WSe_2 photodetectors enabled with asymmetrical van der waals contact interfaces," *npj 2D Materials and Applications*, vol. 4, no. 1, pp. 1–9, Dec. 2020.

TH-2675_186102019

[16] T.-L. Shen, Y.-W. Chu, Y.-K. Liao, W.-Y. Lee, H.-C. Kuo, T.-Y. Lin, and Y.-F. Chen, "Ultrahigh-performance self-powered flexible photodetector driven from photogating, piezo-phototronic, and ferroelectric effects," *Advanced Optical Materials*, vol. 8, no. 1, p. 1901334, Jan. 2020.

[17] J. Ahn, H. Kim, E. Kim, and J. Ko, "Designing a low-cost iot sensing platform for voc material classification," in *2019 15th International Conference on Distributed Computing in Sensor Systems (DCOSS)*. IEEE, 2019, pp. 82–89.

[18] S. Wang, Y. Kang, L. Wang, H. Zhang, Y. Wang, and Y. Wang, "Organic/inorganic hybrid sensors: A review," *Sensors and Actuators B: Chemical*, vol. 182, pp. 467–481, Jun. 2013.

[19] P. Wang, X. Zhao, and B. Li, "ZnO-coated CuO nanowire arrays: fabrications, optoelectronic properties, and photovoltaic applications," *Optics express*, vol. 19, no. 12, pp. 11 271–11 279, May 2011.

[20] Z. Zang, "Efficiency enhancement of ZnO/Cu_2O solar cells with well oriented and micrometer grain sized Cu_2O films," *Applied Physics Letters*, vol. 112, no. 4, p. 042106, Jan. 2018.

[21] Q. Zhang, K. Zhang, D. Xu, G. Yang, H. Huang, F. Nie, C. Liu, and S. Yang, "CuO nanostructures: Synthesis, characterization, growth mechanisms, fundamental properties, and applications," *Progress in Materials Science*, vol. 60, pp. 208–337, Mar. 2014.

[22] S. Raveesh, V. K. S. Yadav, and R. Paily, "CuO single-nanowire-based white-light photodetector," *IEEE Electron Device Letters*, vol. 42, no. 7, pp. 1021–1024, May 2021.

[23] C. J. Lee, T. Lee, S. Lyu, Y. Zhang, H. Ruh, and H. Lee, "Field emission from well-aligned zinc oxide nanowires grown at low temperature," *Applied Physics Letters*, vol. 81, no. 19, pp. 3648–3650, Nov. 2002.

[24] J. B. Baxter and E. S. Aydil, "Nanowire-based dye-sensitized solar cells," *Applied physics letters*, vol. 86, no. 5, p. 053114, Jan. 2005.

[25] F. Hernandez-Ramirez, A. Tarancon, O. Casals, J. Arbiol, A. Romano-Rodriguez, and J. Morante, "High response and stability in CO and humidity measures using a single SnO_2 nanowire," *Sensors and Actuators B: Chemical*, vol. 121, no. 1, pp. 3–17, Jan. 2007.

[26] O. Lupan, V. Postica, V. Cretu, N. Wolff, V. Duppel, L. Kienle, and R. Adelung, "Single and networked CuO nanowires for highly sensitive p-type semiconductor gas sensor applications," *physica status solidi (RRL)–Rapid Research Letters*, vol. 10, no. 3, pp. 260–266, Mar. 2016.

[27] F. Hernandez-Ramirez, J. D. Prades, A. Hackner, T. Fischer, G. Mueller, S. Mathur, and J. R. Morante, "Miniaturized ionization gas sensors from single metal oxide nanowires," *Nanoscale*, vol. 3, no. 2, pp. 630–634, Nov. 2011.

[28] S. Rackauskas, N. Barbero, C. Barolo, and G. Viscardi, "ZnO nanowire application in chemoresistive sensing: A review," *Nanomaterials*, vol. 7, no. 11, p. 381, Nov. 2017.

[29] Q.-H. Wu, J. Li, and S.-G. Sun, "Nano SnO_2 gas sensors," *Current Nanoscience*, vol. 6, no. 5, pp. 525–538, Oct. 2010.

[30] Q. Jin, W. Wen, S. Zheng, R. Jiang, and J.-M. Wu, "Branching TiO_2 nanowire arrays for enhanced ethanol sensing," *Nanotechnology*, vol. 32, no. 29, p. 295501, Apr. 2021.

[31] Z.-X. Cai, H.-Y. Li, X.-N. Yang, and X. Guo, "NO sensing by single crystalline WO_3 nanowires," *Sensors and Actuators B: Chemical*, vol. 219, pp. 346–353, Nov. 2015.

[32] D. Wu, Q. Zhang, and M. Tao, "LSDA+ U study of cupric oxide: Electronic structure and native point defects," *Physical Review B*, vol. 73, no. 23, p. 235206, Jun. 2006.

[33] M. Bettahar, G. Costentin, L. Savary, and J. Lavalley, "On the partial oxidation of propane and propylene on mixed metal oxide catalysts," *Applied Catalysis A: General*, vol. 145, no. 1-2, pp. 1–48, Oct. 1996.

[34] Z. Zhang, C. Shao, X. Li, C. Wang, M. Zhang, and Y. Liu, "Electrospun nanofibers of p-type NiO/n-type ZnO heterojunctions with enhanced photocatalytic activity," *ACS applied materials & interfaces*, vol. 2, no. 10, pp. 2915–2923, Oct. 2010.

TH-2675_186102019

[35] P. Raksa, A. Gardchareon, T. Chairuangsri, P. Mangkorntong, N. Mangkorntong, and S. Choopun, "Ethanol sensing properties of CuO nanowires prepared by an oxidation reaction," *Ceramics International*, vol. 35, no. 2, pp. 649–652, Mar. 2009.

[36] A. Umar, A. A. Ibrahim, U. T. Nakate, H. Albargi, M. A. Alsaiari, F. Ahmed, F. A. Alharthi, A. A. Alghamdi, and N. Al-Zaqri, "Fabrication and characterization of CuO nanoplates based sensor device for ethanol gas sensing application," *Chemical Physics Letters*, vol. 763, p. 138204, Jan. 2021.

[37] A. Umar, J.-H. Lee, R. Kumar, O. Al-Dossary, A. A. Ibrahim, and S. Baskoutas, "Development of highly sensitive and selective ethanol sensor based on lance-shaped CuO nanostructures," *Materials & Design*, vol. 105, pp. 16–24, Sep. 2016.

[38] K. M. Chahrour, N. M. Ahmed, M. Hashim, N. G. Elfadill, and M. Bououdina, "Self-assembly of aligned CuO nanorod arrays using nanoporous anodic alumina template by electrodeposition on Si substrate for ir photodetectors," *Sensors and Actuators A: Physical*, vol. 239, pp. 209 – 219, Mar. 2016.

[39] A. Tripathi, T. Dixit, J. Agrawal, and V. Singh, "Bandgap engineering in CuO nanostructures: Dual-band, broadband, and UV-C photodetectors," *Applied Physics Lett.*, vol. 116, no. 11, p. 111102, Mar. 2020.

[40] T. Dixit, A. Tripathi, S. V. Solanke, K. L. Ganapathi, M. S. R. Rao, and V. Singh, "Ultra-wide bandgap copper oxide: High performance solar-blind photo-detection," *IEEE Electron Device Lett.*, vol. 41, no. 12, pp. 1790–1793, Dec. 2020.

[41] A. García Marín, C. García Núñez, E. Ruiz, J. Piqueras, and J. L. Pau, "Fast response ZnO:Al/CuO nanowire/ZnO:Al heterostructure light sensors fabricated by dielectrophoresis," *Applied Physics Lett.*, vol. 102, no. 23, p. 232105, Jun. 2013.

[42] S. Lee, W. Lee, B. Jang, T. Kim, J. Bae, K. Cho, S. Kim, and J. Jang, "Sol-gel processed p-type CuO phototransistor for a near-infrared sensor," *IEEE Electron Device Lett.*, vol. 39, no. 1, pp. 47–50, Jan. 2018.

[43] W. Wang, Z. Liu, Y. Liu, C. Xu, C. Zheng, and G. Wang, "A simple wet-chemical synthesis and characterization of CuO nanorods," *Applied Physics A*, vol. 76, no. 3, pp. 417–420, 2003.

[44] M. Cao, Y. Wang, C. Guo, Y. Qi, C. Hu, and E. Wang, "A simple route towards CuO nanowires and nanorods," *Journal of nanoscience and nanotechnology*, vol. 4, no. 7, pp. 824–828, Sep. 2004.

[45] C. Yang, X. Su, F. Xiao, J. Jian, and J. Wang, "Gas sensing properties of CuO nanorods synthesized by a microwave-assisted hydrothermal method," *Sensors and Actuators B: Chemical*, vol. 158, no. 1, pp. 299–303, Nov. 2011.

[46] H. Wu, D. Lin, and W. Pan, "Fabrication, assembly, and electrical characterization of CuO nanofibers," *Applied physics letters*, vol. 89, no. 13, p. 133125, Sep. 2006.

[47] X. Fan, Z. Wu, P. Yan, B. Geng, H. Li, C. Li, and P. Zhang, "Fabrication of well-ordered CuO nanowire arrays by direct oxidation of sputter-deposited Cu_3N film," *Materials letters*, vol. 62, no. 12-13, pp. 1805–1808, Apr. 2008.

[48] X. Wen, Y. Xie, C. L. Choi, K. C. Wan, X.-Y. Li, and S. Yang, "Copper-based nanowire materials: templated syntheses, characterizations, and applications," *Langmuir*, vol. 21, no. 10, pp. 4729–4737, May 2005.

[49] L. Yuan, Y. Wang, R. Mema, and G. Zhou, "Driving force and growth mechanism for spontaneous oxide nanowire formation during the thermal oxidation of metals," *Acta Materialia*, vol. 59, no. 6, pp. 2491–2500, Apr. 2011.

[50] L.-B. Luo, X.-H. Wang, C. Xie, Z.-J. Li, R. Lu, X.-B. Yang, and J. Lu, "One-dimensional CuO nanowire: synthesis, electrical, and optoelectronic devices application," *Nanoscale research lett.*, vol. 9, no. 1, pp. 1–8, Dec. 2014.

[51] Z. Fan, J. C. Ho, T. Takahashi, R. Yerushalmi, K. Takei, A. C. Ford, Y.-L. Chueh, and A. Javey, "Toward the development of printable nanowire electronics and sensors," *Advanced Materials*, vol. 21, no. 37, pp. 3730–3743, Oct. 2009.

TH-2675_186102019

[52] A. Vomiero, A. Ponzoni, E. Comini, M. Ferroni, G. Faglia, and G. Sberveglieri, "Direct integration of metal oxide nanowires into an effective gas sensing device," *Nanotechnology*, vol. 21, no. 14, p. 145502, Mar. 2010.

[53] C. M. Hung, D. T. T. Le, and N. Van Hieu, "On-chip growth of semiconductor metal oxide nanowires for gas sensors: A review," *Journal of Science: Advanced Materials and Devices*, vol. 2, no. 3, pp. 263–285, Sep. 2017.

[54] Y. H. Ko, G. Nagaraju, S. H. Lee, and J. S. Yu, "Facile preparation and optoelectronic properties of CuO nanowires for violet light sensing," *Materials Letters*, vol. 117, pp. 217–220, Feb. 2014.

[55] P. Shi, J. Zhang, H.-Y. Lin, and P. W. Bohn, "Effect of molecular adsorption on the electrical conductance of single Au nanowires fabricated by electron-beam lithography and focused ion beam etching," *Small*, vol. 6, no. 22, pp. 2598–2603, Nov. 2010.

[56] C. Huang, X. Tian, J. Liu, Z. Dong, and Y. Wang, "The assembly and fabrication of single CuO nanowire electronic device based on controllable DWS-DEP technology," *IEEE Transactions on Nanotechnology*, vol. 14, no. 1, pp. 101–107, Nov. 2015.

[57] V. K. S. Yadav, G. Natu, and R. Paily, "Analysis of superfine-resolution printing of polyaniline and silver microstructures for electronic applications," *IEEE Transactions on Components, Packaging and Manufacturing Technology*, vol. 8, no. 9, pp. 1678–1685, Jul. 2018.

[58] V. K. S. Yadav, G. Natu, and R. P. Paily, "Fabrication and electrical characterization of printed microresistors of silver nanoparticles using microcantilever-based printing technology," *IEEE Transactions on Components, Packaging and Manufacturing Technology*, vol. 10, no. 1, pp. 57–64, Nov. 2019.

[59] S. N. Das, K.-J. Moon, J. P. Kar, J.-H. Choi, J. Xiong, T. I. Lee, and J.-M. Myoung, "ZnO single nanowire-based UV detectors," *Applied Physics Letters*, vol. 97, no. 2, p. 022103, Jul. 2010.

[60] X. Jiang, T. Herricks, and Y. Xia, "CuO nanowires can be synthesized by heating copper substrates in air," *Nano letters*, vol. 2, no. 12, pp. 1333–1338, Dec. 2002.

[61] V. K. S. Yadav, S. Raveesh, T. T. Daniel, and R. Paily, "Microcantilever printed back-to-back ZnO single-nanowire Schottky diodes," *IEEE Transactions on Electron Devices*, vol. 67, no. 8, pp. 3309–3314, Jun. 2020.

[62] C. Li, Y. Bando, M. Liao, Y. Koide, and D. Golberg, "Visible-blind deep-ultraviolet Schottky photodetector with a photocurrent gain based on individual Zn_2GeO_4 nanowire," *Applied Physics Letters*, vol. 97, no. 16, p. 161102, Oct. 2010.

[63] Q. Hong, Y. Cao, J. Xu, H. Lu, J. He, and J.-L. Sun, "Self-powered ultrafast broadband photodetector based on p–n heterojunctions of CuO/Si nanowire array," *ACS Applied Materials & Interfaces*, vol. 6, no. 23, pp. 20 887–20 894, Dec. 2014.

[64] V. K. Gurugubelli and S. Karmalkar, "Effective medium theory of the space-charge region electrostatics of arrays of nanoscale junctions," *Journal of Applied Physics*, vol. 119, no. 2, p. 024507, Jan. 2016.

[65] D. Y. Guo, Z. P. Wu, Y. H. An, X. C. Guo, X. L. Chu, C. L. Sun, L. H. Li, P. G. Li, and W. H. Tang, "Oxygen vacancy tuned Ohmic-Schottky conversion for enhanced performance in β-Ga_2O_3 solar-blind ultraviolet photodetectors," *Applied Physics Letters*, vol. 105, no. 2, p. 023507, Jul. 2014.

[66] W. Yin, J. Yang, K. Zhao, A. Cui, J. Zhou, W. Tian, W. Li, Z. Hu, and J. Chu, "High responsivity and external quantum efficiency photodetectors based on solution-processed Ni-doped CuO films," *ACS Applied Materials & Interfaces*, vol. 12, no. 10, pp. 11 797–11 805, Feb. 2020.

[67] A. Li, H. Song, J. Zhou, X. Chen, and S. Liu, "CuO nanowire growth on Cu_2O by in situ thermal oxidation in air," *CrystEngComm*, vol. 15, no. 42, pp. 8559–8564, Aug. 2013.

[68] P. Chand, A. Gaur, and A. Kumar, "Structural, optical and ferroelectric behavior of CuO nanostructures synthesized at different pH values," *Superlattices and Microstructures*, vol. 60, pp. 129–138, Aug. 2013.

[69] M. Gerosa, C. E. Bottani, L. Caramella, G. Onida, C. Di Valentin, and G. Pacchioni, "Defect calculations in semiconductors through a dielectric-dependent hybrid DFT functional: The case of oxygen vacancies in metal oxides," *The Journal of chemical physics*, vol. 143, no. 13, p. 134702, Oct. 2015.

TH-2675_186102019

[70] C. Wang, L. Yin, L. Zhang, D. Xiang, and R. Gao, "Metal oxide gas sensors: sensitivity and influencing factors," *sensors*, vol. 10, no. 3, pp. 2088–2106, Mar. 2010.

[71] N. Murari, R. Thomas, A. Winterman, R. Melgarejo, S. Pavunny, and R. Katiyar, "Structural, electrical, and magnetic properties of chemical solution deposited $Bi(Fe_{0.95}Cr_{0.05})O_3$ thin films on platinized silicon substrates," *Journal of Applied Physics*, vol. 105, no. 8, p. 084110, Apr. 2009.

[72] P. Hu, X. Li, J. Lu, M. Yang, Q. Lv, and S. Li, "Oxygen deficiency effect on resistive switching characteristics of copper oxide thin films," *Physics Letters A*, vol. 375, no. 18, pp. 1898–1902, May 2011.

[73] M. Yang, N. Qin, L. Ren, Y. Wang, K. Yang, F. Yu, W. Zhou, M. Meng, S. Wu, D. Bao *et al.*, "Realizing a family of transition-metal-oxide memristors based on volatile resistive switching at a rectifying metal/oxide interface," *Journal of Physics D: Applied Physics*, vol. 47, no. 4, p. 045108, Dec. 2013.

[74] B. Mohammad, M. Abi Jaoude, V. Kumar, D. M. Al Homouz, H. A. Nahla, M. Al-Qutayri, and N. Christoforou, "State of the art of metal oxide memristor devices," *Nanotechnology Reviews*, vol. 5, no. 3, pp. 311–329, Jun. 2016.

[75] U. Patil, N. S. Ramgir, N. Karmakar, A. Bhogale, A. Debnath, D. Aswal, S. Gupta, and D. Kothari, "Room temperature ammonia sensor based on copper nanoparticle intercalated polyaniline nanocomposite thin films," *Applied Surface Science*, vol. 339, pp. 69–74, Jun. 2015.

[76] F. Ren, L. Gao, Y. Yuan, Y. Zhang, A. Alqrni, O. M. Al-Dossary, and J. Xu, "Enhanced BTEX gas-sensing performance of CuO/SnO_2 composite," *Sensors and Actuators B: Chemical*, vol. 223, pp. 914–920, Feb. 2016.

[77] S.-Y. Cho, H.-W. Yoo, J. Y. Kim, W.-B. Jung, M. L. Jin, J.-S. Kim, H.-J. Jeon, and H.-T. Jung, "High-resolution p-type metal oxide semiconductor nanowire array as an ultrasensitive sensor for volatile organic compounds," *Nano letters*, vol. 16, no. 7, pp. 4508–4515, Jul. 2016.

[78] P. Krcmar, I. Kuritka, J. Maslik, P. Urbanek, P. Bazant, M. Machovsky, P. Suly, and P. Merka, "Fully inkjet-printed CuO sensor on flexible polymer substrate for alcohol vapours and humidity sensing at room temperature," *Sensors*, vol. 19, no. 14, p. 3068, Jan. 2019.

[79] N. Sarıca, O. Alev, L. Ç. Arslan, and Z. Z. Öztürk, "Characterization and gas sensing performances of noble metals decorated CuO nanorods," *Thin Solid Films*, vol. 685, pp. 321–328, Sep. 2019.

[80] B. Karunagaran, P. Uthirakumar, S. Chung, S. Velumani, and E.-K. Suh, "TiO_2 thin film gas sensor for monitoring ammonia," *Materials Characterization*, vol. 58, no. 8-9, pp. 680–684, Aug. 2007.

[81] S. Park, Z. Cai, J. Lee, J. I. Yoon, and S.-P. Chang, "Fabrication of a low-concentration H_2S gas sensor using CuO nanorods decorated with Fe_2O_3 nanoparticles," *Materials Letters*, vol. 181, pp. 231–235, Oct. 2016.

[82] L. Lopez, V. Copa, T. Hayasaka, M. A. Faustino-Lopez, Y. Wu, H. Liu, Y. Liu, E. Estacio, A. Somintac, L. Lin *et al.*, "Influence of chamber design on the gas sensing performance of graphene field-effect-transistor," *SN Applied Sciences*, vol. 2, pp. 1–11, Jul. 2020.

[83] R. O. Cebolla, E. Weidner, W. Buttner, C. Bonato, K. Hartmann, and K. Schmidt, "Test methodologies for hydrogen sensor performance assessment: Chamber vs. flow-through test apparatus," *International Journal of Hydrogen Energy*, vol. 43, no. 45, pp. 21 149–21 160, Nov. 2018.

[84] F.-E. Annanouch, G. Bouchet, P. Perrier, N. Morati, C. Reynard-Carette, K. Aguir, and M. Bendahan, "How the chamber design can affect gas sensor responses," in *Multidisciplinary Digital Publishing Institute Proceedings*, vol. 2, no. 13, 2018, p. 820.

[85] P. Sedlák and P. Kuberskỳ, "The effect of the orientation towards analyte flow on electrochemical sensor performance and current fluctuations," *Sensors*, vol. 20, no. 4, p. 1038, Jan. 2020.

[86] A. Lezzi, G. Beretta, E. Comini, G. Faglia, G. Galli, and G. Sberveglieri, "Influence of gaseous species transport on the response of solid state gas sensors within enclosures," *Sensors and Actuators B: Chemical*, vol. 78, no. 1-3, pp. 144–150, Aug. 2001.

TH-2675_186102019

[87] V. K. Tomer and S. Duhan, "Ordered mesoporous Ag-doped TiO_2/SnO_2 nanocomposite based highly sensitive and selective voc sensors," *Journal of Materials Chemistry A*, vol. 4, no. 3, pp. 1033–1043, Jan. 2016.

[88] M. Sriyudthsak, L. Promsong, and S. Panyakeow, "Effect of carrier gas on response of oxide semiconductor gas sensor," *Sensors and Actuators B: Chemical*, vol. 13, no. 1-3, pp. 139–142, May 1993.

[89] Y. Zhou, Y. Wang, Y. Wang, X. Li, and Y. Guo, "The impact of carrier gas on room-temperature trace nitrogen dioxide sensing of ZnO nanowire-integrated film under UV illumination," *Ceramics International*, vol. 46, no. 10, pp. 16 056–16 061, Jul. 2020.

[90] M. Kumar and D. Bhadu, "Design performance and frequency response analysis of SAW-based sensor for dichloromethane gas sensing amidst the COVID-19," *Journal of Vibration Engineering & Technologies*, vol. 9, no. 5, pp. 725–732, Jul. 2021.

[91] Y. Zhang, S. Li, J. Zhang, Z. Pan, D. Min, X. Li, X. Song, and J. Liu, "High-performance gas sensors with temperature measurement," *Scientific reports*, vol. 3, no. 1, pp. 1–7, Feb. 2013.

[92] S. Das and M. Pal, "Non-invasive monitoring of human health by exhaled breath analysis: A comprehensive review," *Journal of The Electrochemical Society*, vol. 167, no. 3, p. 037562, Feb. 2020.

[93] A. F. Van Putten, M. J. van Putten, M. H. van Putten, and P. F. Van Putten, "Multisensor microsystem for pulmonary function diagnostics," *IEEE sensors journal*, vol. 2, no. 6, pp. 636–643, Dec. 2002.

[94] G. Eranna, *Metal oxide nanostructures as gas sensing devices*. CRC press, Dec. 2011.

[95] H. Chung, M. K. Yoon, J. Han, and Y.-S. Kim, "Evaluation of volatile organic compounds in alcoholic beverages consumed in korea," *Journal of the Korean Society for Applied Biological Chemistry*, vol. 58, no. 3, pp. 423–432, Jun. 2015.

[96] F. Brilli, F. Loreto, and I. Baccelli, "Exploiting plant volatile organic compounds (VOCs) in agriculture to improve sustainable defense strategies and productivity of crops," *Frontiers in plant science*, vol. 10, p. 264, Mar. 2019.

[97] P. Vesely, L. Lusk, G. Basarova, J. Seabrooks, and D. Ryder, "Analysis of aldehydes in beer using solid-phase microextraction with on-fiber derivatization and gas chromatography/mass spectrometry," *Journal of Agricultural and Food Chemistry*, vol. 51, no. 24, pp. 6941–6944, Nov. 2003.

[98] L. S. Teixeira, E. S. Leão, A. F. Dantas, H. L. Pinheiro, A. C. Costa, and J. B. De Andrade, "Determination of formaldehyde in brazilian alcohol fuels by flow-injection solid phase spectrophotometry," *Talanta*, vol. 64, no. 3, pp. 711–715, Oct. 2004.

[99] P. J. Sabourin, W. E. Bechtold, and R. F. Henderson, "A high pressure liquid chromatographic method for the separation and quantitation of water-soluble radiolabeled benzene metabolites," *Analytical biochemistry*, vol. 170, no. 2, pp. 316–327, May 1988.

[100] F. Wei, P. Patel, W. Liao, K. Chaudhry, L. Zhang, M. Arellano-Garcia, S. Hu, D. Elashoff, H. Zhou, S. Shukla *et al.*, "Electrochemical sensor for multiplex biomarkers detection," *Clinical Cancer Research*, vol. 15, no. 13, pp. 4446–4452, Jul. 2009.

[101] V. Levitskii, V. Shapovalov, A. Komlev, A. Zav'yalov, V. Vit'ko, A. Komlev, and E. Shutova, "Raman spectroscopy of copper oxide films deposited by reactive magnetron sputtering," *Technical Physics Letters*, vol. 41, no. 11, pp. 1094–1096, Nov. 2015.

[102] D. Powell, A. Compaan, J. Macdonald, and R. Forman, "Raman-scattering study of ion-implantation-produced damage in Cu_2O," *Physical Review B*, vol. 12, no. 1, p. 20, Jul. 1975.

[103] R. K. Sahoo, A. Das, K. Samantaray, S. K. Singh, R. S. Mane, H.-C. Shin, J. M. Yun, and K. H. Kim, "Electrochemical glucose sensing characteristics of two-dimensional faceted and non-faceted CuO nanoribbons," *CrystEngComm*, vol. 21, no. 10, pp. 1607–1616, Jan. 2019.

[104] H. Hsueh, S. Chang, F. Hung, W. Weng, C. Hsu, T. Hsueh, S. Lin, and B. Dai, "Ethanol gas sensor of crabwise CuO nanowires prepared on glass substrate," *Journal of The Electrochemical Society*, vol. 158, no. 4, p. J106, Feb. 2011.

TH-2675_186102019

[105] Y. Hu, J. Zhou, P.-H. Yeh, Z. Li, T.-Y. Wei, and Z. L. Wang, "Supersensitive, fast-response nanowire sensors by using schottky contacts," *Advanced Materials*, vol. 22, no. 30, pp. 3327–3332, Aug. 2010.

[106] S. Steinhauer, E. Brunet, T. Maier, G. Mutinati, A. Köck, and O. Freudenberg, "single suspended CuO nanowire for conductometric gas sensing," *Procedia Engineering*, vol. 47, pp. 17–20, Jan. 2012.

[107] A. Ghosh, A. Maity, R. Banerjee, and S. Majumder, "Volatile organic compound sensing using copper oxide thin films: Addressing the cross sensitivity issue," *Journal of Alloys and Compounds*, vol. 692, pp. 108–118, Jan. 2017.

[108] H. J. Park, N.-J. Choi, H. Kang, H.-K. Lee, S. E. Moon, M. Y. Jung, K. H. Park, and D.-S. Lee, "CuO nanocube gas sensor for ethanol detection," *Sensor Letters*, vol. 12, no. 6-7, pp. 1156–1159, Jun. 2014.

[109] M. Z. Asadzadeh, A. Köck, M. Popov, S. Steinhauer, J. Spitaler, and L. Romaner, "Response modeling of single SnO_2 nanowire gas sensors," *Sensors and Actuators B: Chemical*, vol. 295, pp. 22–29, Sep. 2019.

[110] M. Tonezzer and N. Hieu, "Size-dependent response of single-nanowire gas sensors," *Sensors and Actuators B: Chemical*, vol. 163, no. 1, pp. 146–152, Mar. 2012.

[111] D. Wang, J. G. Lu, C. J. Otten, and W. E. Buhro, "Electrical transport in boron nanowires," *Applied physics letters*, vol. 83, no. 25, pp. 5280–5282, Dec. 2003.

[112] K. Ye, B. Wang, A. Nie, K. Zhai, F. Wen, C. Mu, Z. Zhao, J. Xiang, Y. Tian, and Z. Liu, "Broadband photodetector of high quality Sb_2S_3 nanowire grown by chemical vapor deposition," *Journal of Materials Science & Technology*, vol. 75, pp. 14–20, Jun. 2021.

[113] A. A. Talin, F. Léonard, B. Swartzentruber, X. Wang, and S. D. Hersee, "Unusually strong space-charge-limited current in thin wires," *Physical Review Letters*, vol. 101, no. 7, p. 076802, Aug. 2008.

[114] S. K. Kajli, D. Ray, and S. C. Roy, "Anomalous diameter dependent electrical transport in individual CuO nanowire," *Journal of Physics D: Applied Physics*, vol. 54, no. 25, p. 255104, Apr. 2021.

[115] Z. Lin, R. Zhan, L. Li, H. Liu, S. Jia, H. Chen, S. Tang, J. She, S. Deng, N. Xu *et al.*, "Defect-concentration dependence of electrical transport mechanisms in CuO nanowires," *RSC advances*, vol. 8, no. 4, pp. 2188–2195, Dec. 2018.

[116] B. J. Hansen, N. Kouklin, G. Lu, I.-K. Lin, J. Chen, and X. Zhang, "Transport, analyte detection, and opto-electronic response of p-type CuO nanowires," *The Journal of Physical Chemistry C*, vol. 114, no. 6, pp. 2440–2447, Jan. 2010.

[117] C.-H. Huang, Y. Tang, K. Matsuzaki, and K. Nomura, "Resistive switching memory effects in p-type hydrogen-treated CuO nanowire," *Applied Physics Letters*, vol. 117, no. 4, p. 043502, Jul. 2020.

[118] L. Liao, Z. Zhang, B. Yan, Z. Zheng, Q. Bao, T. Wu, C. M. Li, Z. Shen, J. Zhang, H. Gong *et al.*, "Multifunctional CuO nanowire devices: p-type field effect transistors and CO gas sensors," *Nanotechnology*, vol. 20, no. 8, p. 085203, Feb. 2009.

[119] A. Gonçalves, L. Campos, A. Ferlauto, and R. Lacerda, "On the growth and electrical characterization of cuo nanowires by thermal oxidation," *Journal of Applied Physics*, vol. 106, no. 3, p. 034303, Aug. 2009.

[120] S. Singh and A. Raman, "Gate-all-around charge plasma-based dual material gate-stack nanowire FET for enhanced analog performance," *IEEE Transactions on Electron Devices*, vol. 65, no. 7, pp. 3026–3032, Apr. 2018.

[121] *Force Nanosciences*, Accessed: April 15, 2020. [Online]. Available: www.bioforcenano.com

[122] J. Xu, M. Lynch, J. L. Huff, C. Mosher, S. Vengasandra, G. Ding, and E. Henderson, "Microfabricated quill-type surface patterning tools for the creation of biological micronano arrays," *Biomedical Microdevices*, vol. 6, p. 117–123, June 2004.

[123] V. K. S. Yadav, G. Natu, and R. P. Paily, "Fabrication and electrical characterization of printed microresistors of silver nanoparticles using microcantilever-based printing technology," *IEEE Transactions on Components, Packaging and Manufacturing Technology*, vol. 10, no. 1, pp. 57–64, Jan 2020.

TH-2675_186102019

[124] A. D. Fortes, "Crystal structures of spinel-type Na_2MoO_4 and Na_2WO_4 revisited using neutron powder diffraction," *Acta Crystallographica Section E: Crystallographic Communications*, vol. 71, no. 6, pp. 592–596, Jun. 2015.

[125] J. H. Park, Y. B. Yoo, K. H. Lee, W. S. Jang, J. Y. Oh, S. S. Chae, H. W. Lee, S. W. Han, and H. K. Baik, "Boron-doped peroxo-zirconium oxide dielectric for high-performance, low-temperature, solution-processed indium oxide thin-film transistor," *ACS applied materials & interfaces*, vol. 5, no. 16, pp. 8067–8075, Aug. 2013.

[126] B. S. Kim, Y. Taek Jeong, D. Lee, T. Choi, S.-H. Jung, J. Whan Choi, C. Yang, K. Jo, B.-j. Lee, E. Park *et al.*, "Solution-processed zinc-indium-tin oxide thin-film transistors for flat-panel displays," *Applied Physics Letters*, vol. 103, no. 7, p. 072110, Aug. 2013.

[127] P. N. Plassmeyer, K. Archila, J. F. Wager, and C. J. Page, "Lanthanum aluminum oxide thin-film dielectrics from aqueous solution," *ACS Applied Materials & Interfaces*, vol. 7, no. 3, pp. 1678–1684, 2015.

[128] A. J. Chiquito, C. A. Amorim, O. M. Berengue, L. S. Araujo, E. P. Bernardo, and E. R. Leite, "Back-to-back Schottky diodes: the generalization of the diode theory in analysis and extraction of electrical parameters of nanodevices," *Journal of Physics: Condensed Matter*, vol. 24, no. 22, p. 225303, Jun. 2012.

[129] H. Kim, H. Kim, and D.-W. Kim, "Silver Schottky contacts to α-plane bulk ZnO," *Journal of Applied Physics*, vol. 108, no. 7, p. 074514, Oct 2010.

[130] S. K. Cheung and N. W. Cheung, "Extraction of Schottky diode parameters from forward current-voltage characteristics," *Applied Physics Letters*, vol. 49, no. 2, pp. 85–87, May 1986.

[131] X. Zhang, J. Zhai, X. Yu, L. Ding, and W. Zhang, "Fabrication and characterization of flexible Ag/ZnO Schottky diodes on polyimide substrates," *Thin Solid Films*, vol. 548, pp. 623 – 626, Dec 2013.

[132] T. B. Daunis, J. M. Tran, and J. W. Hsu, "Effects of environmental water absorption by solution-deposited Al_2O_3 gate dielectrics on thin film transistor performance and mobility," *ACS applied materials & interfaces*, vol. 10, no. 46, pp. 39 435–39 440, Nov. 2018.

[133] A. Ghosh, A. Maity, R. Banerjee, and S. Majumder, "Volatile organic compound sensing using copper oxide thin films: Addressing the cross sensitivity issue," *Journal of Alloys and Compounds*, vol. 692, pp. 108–118, Jan. 2017.

[134] S. Kulkarni and R. Ghosh, "A simple approach for sensing and accurate prediction of multiple organic vapors by sensors based on CuO nanowires," *Sensors and Actuators B: Chemical*, vol. 335, p. 129701, May 2021.

TH-2675_186102019

List of Publications

Thesis work

1. **S. Raveesh**, V. K. S. Yadav and R. Paily, "CuO Single-Nanowire-Based White-Light Photodetector," IEEE Electron Device Letters, vol. 42, no. 7, pp. 1021-1024, July 2021, doi: 10.1109/LED.2021.3081627.

2. **Siddaramaiah R**, Yadav VK, Pal A, Palathinkal RP. "High-performance CuO nanowire printed devices for visible light sensing and switching characteristics," Materials Letters, vol. 320, p. 132300, Aug 2022, doi: 10.1016/j.matlet.2022.132300.

3. **S. Raveesh**, V. K. S. Yadav, T. T. Daniel, and R. Paily, "CuO Single-Nanowire Printed Devices for Volatile Organic Compounds (VOCs) Detection" in IEEE Transactions on Nanotechnology, (Revision submitted).

4. **S. Raveesh**, V. K. S. Yadav, and R. Paily, "Microcantilever Printed CuO Single Nanowire Field-Effect Transistors" in IEEE Transactions on Nanotechnology, (under review).

5. **S. Raveesh**, V. K. S. Yadav, and R. Paily "Solution-processed planar printed capacitor and field effect transistor," in IEEE Transactions on Components, Packaging and Manufacturing Technology (manuscript under preparation).

Collaboration work

1. V. K. S. Yadav, T. T. Daniel, **S. Raveesh** and R. Paily, "Room Temperature Air Pollutants Sensors Using Printed ZnO Single-Nanowire Schottky Diodes," IEEE Transactions on Nanotechnology, vol. 20, pp. 338-345, 2021.

2. T. T. Daniel, **S. Raveesh**, K. Saikia and R. P. Paily, "Magneto-Semiconductor Resistor for Hydrogen Detection," IEEE Sensors Journal, vol. 21, no. 7, pp. 9038-9045, April, 2021.

3. V. K. S. Yadav, **S. Raveesh**, T. T. Daniel and R. Paily, "Microcantilever Printed Back-to-Back ZnO Single-Nanowire Schottky Diodes," IEEE Transactions on Electron Devices, vol. 67, no. 8, pp. 3309-3314, Aug. 2020.

TH-2675_186102019

4. T. T. Daniel, K. Saikia, **S. Raveesh**, and R. P. Paily, " Hydrogen Sensing of Heterostructured Magnetic Nanospheres with Different Fe to Zn Molar Ratio," in IEEE Transactions on Nanotechnology, vol. 20, pp. 669-677, 2021.

TH-2675_186102019

TH-2675_186102019